MODELING OF MOFs BASED CO_2 ADSORPTION SYSTEMS

BY

YASIR JAMIL

A Thesis Presented to the
DEANSHIP OF GRADUATE STUDIES

KING FAHD UNIVERSITY OF PETROLEUM & MINERALS

DHAHRAN, SAUDI ARABIA

In Partial Fulfillment of the
Requirements for the Degree of

MASTER OF SCIENCE

In

MECHANICAL ENGINEERING

DECEMBER, 2014

KING FAHD UNIVERSITY OF PETROLEUM & MINERALS

DHAHRAN- 31261, SAUDI ARABIA

DEANSHIP OF GRADUATE STUDIES

This thesis, written by **Yasir Jamil** under the direction of his thesis advisor and approved by his thesis committee, has been presented and accepted by the Dean of Graduate Studies, in partial fulfillment of the requirements for the degree of **MASTER OF SCIENCE IN MECHANICAL ENGINEERING.**

Med Habib

Dr. Mohamed A. Habib
(Advisor)

Dr. Zuhair Gasem
Department Chairman

Said

Dr. Syed A. M. Said
(Member)

Dr. Salam A. Zummo
Dean of Graduate Studies

Dr. Abdul Khaliq
(Member)

15/1/15

Date

To my Father and Mother, without their prayers and support I may not be able to come this far

To my wife for her continuous encouragement

To my Teachers for their guidance and tutelage

To my beloved country ‘Pakistan’

ACKNOWLEDGEMENTS

"In the name of Allah, The Most Gracious and The Most Merciful"

All praise belongs to Almighty Allah (s.w.t.) for bestowing me with courage and perseverance to carry out this work sincerely. I thank Almighty Allah for giving me chance to do my M.S. successfully at King Fahd University of Petroleum and Minerals, Dhahran.

My great thanks to King Fahd University of Petroleum and Minerals for providing me good academic platform and financial support during my M.S., thanks is also due to the KACST TIC-CCS at KFUPM.

My deep gratitude and appreciation goes to my thesis advisor and mentor Dr. M.A. Habib for his constant guidance, motivation and support during the course of my studies. His valuable suggestions broadened my horizon in the field of CCS, made this work interesting and challenging for me. I also wish to express my deep appreciation to Dr. Syed A. M. Said and Dr. Abdul Khaliq for their help, guidance, and constant encouragement during my M.S.

Many thanks to Dr. Medhat A. Nemitallah for his support and technical assistance during simulation work. I would also like to thank Dr. Haider Ali and Mr. Pervez Ahmed for their encouragement and guidance.

I am very grateful to Furqan Tahir, Binash Imtiyaz, Ahmer Ali and Maimoon Atif for their help and encouragement during my Masters. Also special thanks to Danish Sattar, Haider Ali and Waqas Ahmed for their support. I would also like to acknowledge all the Mechanical Engineering faculty members with whom I took courses during my M.S., who helped me a lot during my coursework. I also owe thanks to all the students and faculty with whom I interacted during my Master's program.

TABLE OF CONTENTS

LIST OF TABLES

LIST OF FIGURES

LIST OF ABBREVIATIONS

CCS	:	Carbon Capture and Sequestration
CFD	:	Computational Fluid Dynamics
COF	:	Covalent Organic Frameworks
DFT	:	Density Functional Theory
GCMC	:	Grand Canonical Monte Carlo
IGCC	:	Integrated Gasification Combined Cycle
IPCC	:	Inter-governmental Panel on Climate Change
ITM	:	Ion Transport Membranes
LDF	:	Linear Driving Force
MOFs	:	Metal Organic Frameworks
PSA	:	Pressure Swing Adsorption
TSA	:	Temperature Swing Adsorption
UDF	:	User Defined Function

ABSTRACT

FULL NAME : YASIR JAMIL

THESIS TITLE : MODELING OF MOFs BASED CO_2 ADSORPTION SYSTEM

MAJOR FIELD : MECHANICAL ENGINEERING

DATE OF DEGREE : NOVEMBER, 2014

The anthropogenic CO_2 emission resulting from the burning of fossil fuels, to meet the growing global energy demand, poses a serious threat on environment as global warming. Reducing CO_2 and other greenhouse gases concentration in the environment has quickly become the most important environmental issue of our age. Extensive research has been carried out in the area of Carbon Capture and Sequestration (CCS). Post-combustion carbon capture technology provides a novel mean to address this environmental issue because this can be retrofitted to existing units that produce two-thirds of the CO_2 in power sector. In Post-combustion carbon capture technology, flue gases produced by combustion are being treated to remove CO_2. Metal Organic Frameworks (MOFs) represent a new class of porous materials available for CO_2 capture. MOFs are cage like structure composed of metallic nodes connected by a network of organic linkers. The present study focuses on modelling of adsorption system for CO_2 having different adsorbents like activated carbon, zeolite and Metal Organic Frameworks (MOFs). The adsorption model is based on modified Dubinin-Astakov (D-A) adsorption equation. Simulations are performed using finite volume method with CFD commercial software FLUENT. To set the boundary conditions, User Defined Functions (UDF) is hooked in FLUENT. Effect of storage pressure and bed porosity on heat and mass transfer processes for adsorption is studied while taking into account the influence of viscous and inertial resistances of porous media. Heat and mass transfer features of the numerical model are validated by the experimental data of hydrogen adsorption on activated carbon. Dubinin-Astakov (D-A) adsorption equation parameters like enthalpic factor, entropic factor, limiting pressure, limiting adsorption are found by regression analysis using CO_2 adsorption isotherm for different adsorbents. At tank entrance, mass flux profile of CO_2 is established using user defined function (UDF). Results show that highest amount of absolute adsorption is found at the entrance and near wall regions. Whereas lowest amount of the absolute adsorption is found to be in the central region of the storage tank. Maximum temperature is found in the central region of the tank and is lower at entrance and in areas adjacent to walls. After main charging phase, temperature distribution tends to become uniform. Comparisons between CO_2 adsorption in activated carbon, zeolite and Mg-MOF-74 have been presented while considering the effect of storage pressure for a range of pressure from 20 kPa to 100 kPa. The amount of absolute adsorption has been increased while increasing storage pressure. Mg-MOF-74 adsorbent material showed high adsorption capacity as compared to zeolite and activate carbon. Bed porosity of the adsorption bed has been varied and is found that, with increase in bed porosity, peak value of temperature at different locations within adsorption bed increases and also delay in peaks of temperature is observed.

ملخص الرسالة

الاسم الكامل: ياسر جميل

عنوان الرسالة: نمذجة نظام الامتصاص المبنى على ال"موف" لثاني اكسيد الكربون

التخصص: هندسة ميكانيكية

تاريخ الدرجة العلمية: نوفمبر 2014

تشكل إنبعاثات ثانى أكسيد الكربون الناتجة عن حرق الوقود الأحفوري، لتلبية الطلب العالمي على الطاقة المتنامية، تهديدا خطيرا على البيئة متمثلا فى ظاهرة الاحتباس الحراري. أصبح الحد من تركيز إنبعاثات ثانى أكسيد الكربون وغيرها من غازات الاحتباس الحراري في البيئة قضية البيئة الأولى فى العصر الحالى. وقد أجريت بحوث واسعة النطاق في مجال التقاط الكربون وتخزينه. تقدم تكنولوجيا التقاط الكربون في مرحلة ما بعد الاحتراق وسيلة مبتكرة لمعالجة هذه القضية البيئية لأن هذه التكنولوجيا يمكن تطبيقها فى وحدات إنتاج الطاقة القائمة والتي تنتج حوالى ثلثي الإنبعاثات الكلية لثانى أكسيد الكربون. في تكنولوجيا التقاط الكربون في مرحلة ما بعد الاحتراق يتم معالجة غازات العادم الناتجة من عملية الإحتراق من أجل فصل الكربون. تمثل أطر المعادن العضوية فئة جديدة من المواد المسامية والمتاحة لإلتقاط ثانى أكسيد الكربون. تتشكل أطر المواد العضوية من هيكل قفصى يتألف من عقد معدنية متصلة بواسطة شبكة من الوصلات العضوية. تركز الدراسة الحالية على نمذجة نظام إمتزاز ثانى أكسيد الكربون بإستخدام ممتزات مختلفة مثل الكربون المنشط، الزيوليت وأطر المعادن العضوية. تم عمل نموذج للإمتزاز بناء على تعديل معادلة دوبينين-أستاكوف. تم تنفيذ عمليات المحاكاة عن طريق عمل كود مبنى على أساس ديناميكا الموائع الحسابية وتم عمل الحسابات بإستخدام البرنامج التجاري فلوينت. تم عمل كود بإستخدام لغة البرمجة C++ لضبط ظروف السريان عند الدخول وتم دمجها مع برنامج فلوينت. تم دراسة تأثير ضغط التخزين والمسامية على عمليات إنتقال الكتلة والحرارة خلال عملية الإمتزاز مع الأخذ في الاعتبار تأثير مقاومتا اللزوجة والقصور الذاتي داخل مادة التخزين. تم التحقق من صحة حسابات إنتقال الحرارة والكتلة عن طريق مقارنة نتائج البرنامج المستخدم مع البيانات

التجريبية لإمتصاص الهيدروجين فى الكربون المنشط. تم العثور على قيم المعاملات فى معادلة دوبينين-أستاكوف للإمتزاز مثل معامل الإنثالبى ومعامل الإنتروبى وأقصى ضغط وأقصى إمتزاز عن طريق تحليل الانحدار لبيانات إمتزاز ثانى أكسيد الكربون فى ممتزات مختلفة وتحت درجة حرارة ثابتة. تم إستخدام دالة معرفة للبرنامج مكتوبة بلغة ++C لتحديد كمية سريان ثانى أكسيد الكربون كدالة فى الزمن عند مدخل الخزان. تشير النتائج إلى أن أعلى كمية للإمتزاز المطلق وجدت في المناطق عند مدخل الخزان وبالقرب من الجداران. في حين أن أقل كمية للإمتزاز المطلق وجدت في المنطقة الوسطى من خزان التخزين .تم العثور على درجة الحرارة القصوى في منطقة وسط الخزان ودرجة الحرارة الصغرى عند المدخل وفي المناطق المتاخمة للجدران. يميل توزيع درجات الحرارة إلى أن يصبح موحد بعد مرحلة الشحن الرئيسية. تم عرض مقارنات بين إمتزاز ثانى أكسيد الكربون في الكربون المنشط والزيوليت وأطر المعدن العضوى (Mg-MOF-74) مع مراعاة تأثير ضغط التخزين في المدى من 20 كيلو باسكال إلى 100 كيلو باسكال. أظهرت النتائج زيادة كمية الامتزاز المطلق مع زيادة ضغط التخزين .وأظهرت مادة أطر المعدن العضوى (Mg-MOF-74) قدرة عالية على إمتصاص ثانى أكسيد الكربون بالمقارنة مع الزيوليت والكربون النشط. تم دراسة تأثير مسامية الممتزات وقد وجد أنه مع زيادة المسامية تزيد قيمة درجة الحرارة في مناطق مختلفة داخل الخزان ويحدث أيضا تأخير فى الوصول إلى أعلى قيمة لدرجات الجرارة داخل الخزان.

CHAPTER 1

INTRODUCTION

1.1 Climate Challenge and CO_2 Emissions

Climate change is the biggest environmental and humanitarian crisis of our time. This climate challenge is aggravated to such a scale that it has become undeniable as of today. One of the major environmental issue is melting of ice caps of polar region which results not only rise in sea level but it also throws the global ecosystem out of balance because these ice caps are source of fresh water and desalinates oceans when melts. Similarly we are facing more frequent and intense floods in recent years. As the climate changes, rise in sea water temperature creates thermal expansion. This thermal expansion has already raised the oceans height by 4 to 8 inches. Likewise we are facing problems of destructive storms, death of ocean life, increased intensity of droughts and heat waves.

To meet growing population energy requirement, global energy demand is increasing exponentially. Around 80% of current energy requirement is met by fossil fuels. Among fossils fuels 40% is coal and rest includes furnace oil, natural gas, diesel etc [1]. Burning of fossil fuels generates CO_2 which is a greenhouse gas. Greenhouse gases primarily water vapors, CO_2, CH_4, N_2O act as thermal blanket for the Earth, warming surface temperature up to life supporting level by absorbing heat. Since beginning of 19th century significant increase in CO_2 concentration has been observed subsequently increasing global surface temperature. Figure 1 shows the evolution of CO_2 concentration and temperature since year 1000.

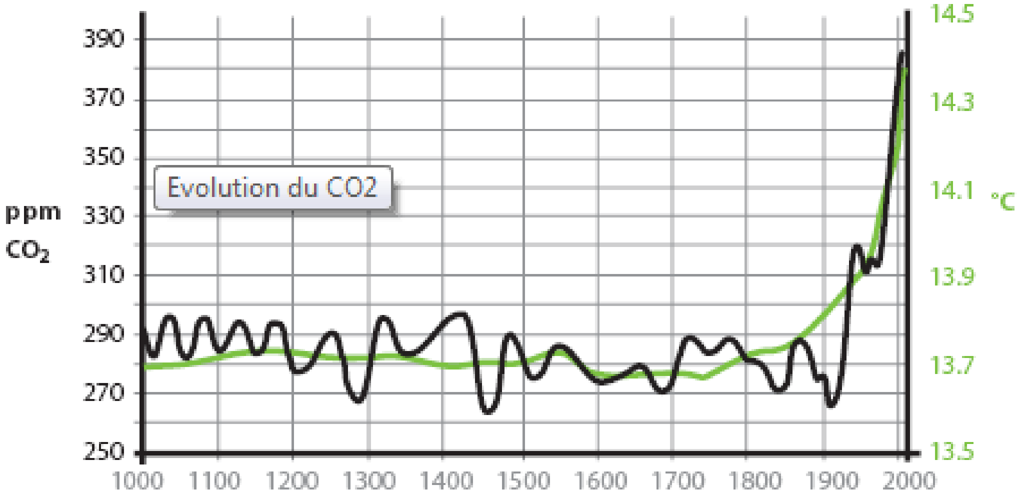

Figure 1: The Evolution of Temperature and CO_2 concentration since year 1000 (Source: GIEC)

The fossil fuel power plants are producing tons of CO_2 every second and making the earth warmer by global warming. Global warming is detrimental for our atmosphere affecting present and next generations by changing climate conditions, water scarcity, ice caps depletion, air pollution etc. The maximum temperature rise of the world in 2090 would be 8 ^{0}C starting from 1990 [2] as shown in Figure 2.

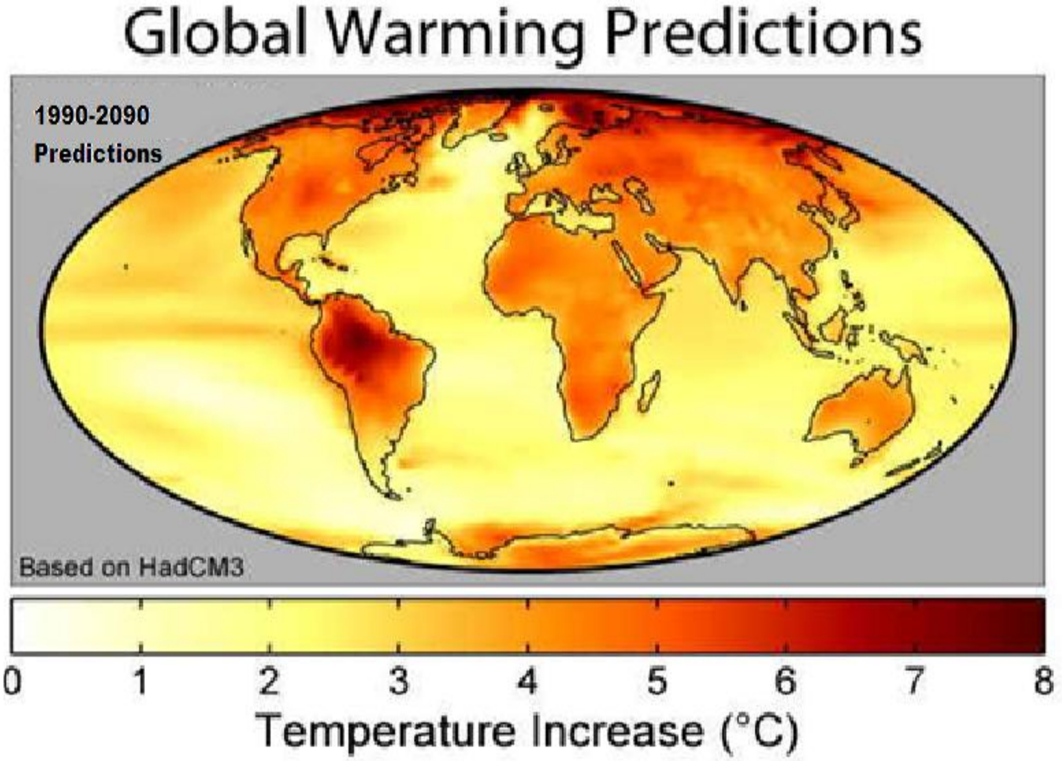

Figure 2: Predictions of temperature rise from 1990-2090 around the globe [2]

Inter-governmental Panel on Climate Change (IPCC) reported some important observations in an assessment report published in 2007 [3]. It is being reported the rise in average temperature of the Earth's surface is +1 ^{0}C since 1910, the average sea level rise for past 100 years is 16 cm and the snow cover depletion in the Northern hemisphere is 9 % within past 50 years. These phenomena are speeding up and the predicted temperature rise till 2030 is 0.2 ^{o}C and if the fossils fuels are being used continuously then the sea level rise would be 59 cm from 18 cm by 2099. To prevent catastrophic penalties of global warming, the carbon dioxide concentration should not cross 450 ppm by 2050. Therefore CO_2 concentrations must be lowered and controlled by developing and adopting alternate energy sources.

1.2 Carbon Capture Technologies

In principle, greenhouse gas emissions from energy production can be reduced by the use of alternative energy sources such as nuclear power and renewable energy. Recently, renewable energy sources are increasingly used, however the immediate energy demand is likely to be met by conventional fossil fuel combustion. To reduce greenhouse gas emissions from fossil fuel-fired power generation plants, carbon capture and sequestration technologies are being developed for CO_2 capture in combustion processes. The development of CO_2 capture technologies (CCS) for hydrocarbon fired power and steam plants can be divided into three broad categories as reported by Jordal et al [4] as shown in Figure 3.

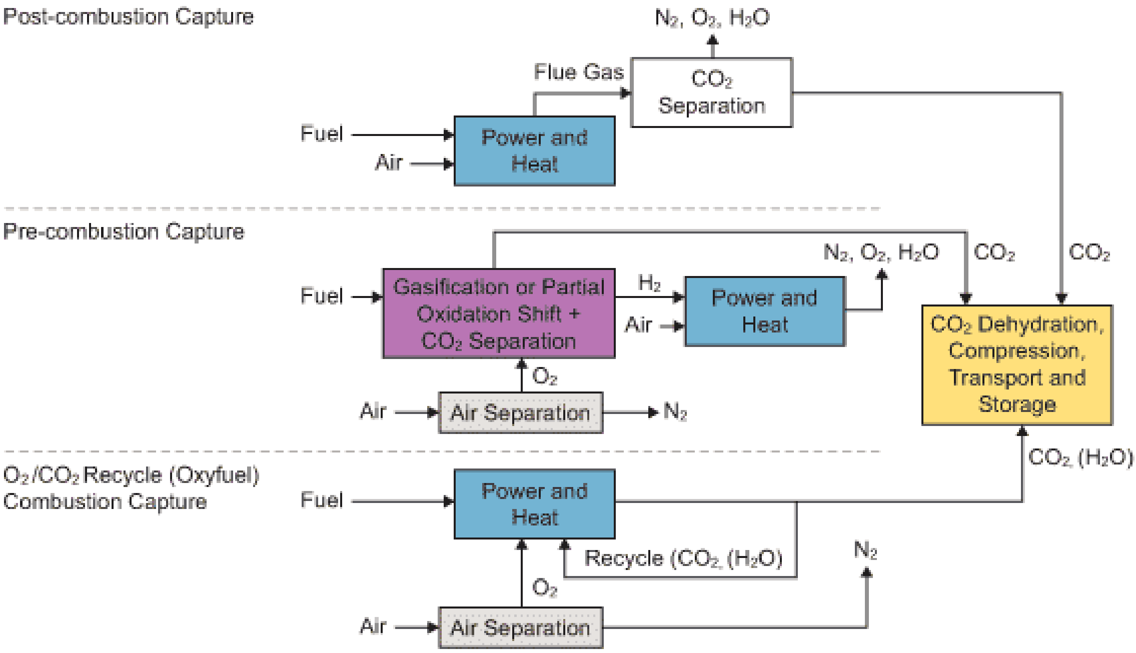

Figure 3: Carbon capture and sequestration technologies [4]

1.2.1 Post combustion capture

The first is separation of CO_2 from waste gas (post-combustion carbon capture). The term post-combustion capture refers to separation of CO_2 from flue gas at the exit of the combustion chamber. Some separation techniques currently used for CO_2 capture from flue gasses are as follows:

- **Absorption in solvents**

This process involves dissolving a solute contained in gas mixture, using a liquid solvent in which this solute is soluble. The most widely used solvents are aqueous solvents containing alkanolamine, commonly called *amine*. The reaction with the amine is reversible and solvent can be regenerated by heating.

- **Adsorption on solids**

This process involves retention of gas or liquid molecules on a solid surface. CO_2 separation processes implement regeneratable adsorbents with high affinity for CO_2, such as zeolites, activated carbon etc. These adsorbents are characterized by a uniform well defined pore size and are capable of separating molecular species by size effect. Since CO_2 is adsorbed on solid surface, the quantity captured is proportional to the developed surface. In adsorption process lowering the temperature and increasing the partial pressure of CO_2 in exhaust gas can increase the capturing of CO_2 by adsorbent. Adsorbent regeneration, i.e. release of the adsorbed gas is carried out by increasing the temperature (TSA), reducing the pressure (PSA) or displacement of adsorbed species by another adosrbable compound.

- **Membrane separation**

This process uses the fact that under the effect of a driving force, various compounds present in a gas do not diffuse at the same rate across the membrane. The driving force might be the partial pressure difference of the compounds in gas each side of membrane.

- **Cryogenics**

CO_2 can be separated from a gas mixture by lowering the temperature and changing the state i.e. transition into liquid or solid phase.

1.2.2 Oxyfuel combustion capture

The second is combustion of fuel in presence of O_2 only instead of air (oxy-fuel combustion carbon capture). In oxy-fuel combustion, the combustion air is replaced by oxygen. Thus, the concentration of CO_2 in flue gas is increased by using pure or enriched oxygen (O_2) instead of air for combustion, either in a boiler or in a gas turbine.

1.2.3 Pre combustion capture

Third technology is production of a carbon free fuel (pre-combustion carbon capture). Pre-combustion capture refers to the removal of carbon from fuel before the combustion process. In this approach, fuel reacts partially at high pressure with oxygen or air and, in some cases, steam, to produce carbon monoxide (CO) and hydrogen (H_2). The CO then reacts with steam in a catalytic shift reactor to produce CO_2 and additional H_2. The hydrogen is used as fuel in a combined cycle plant for electricity generation and the CO_2 is then separated for sequestration.

1.3 Sequestration and Storage

After separating CO_2 contents from flue gases of power plants, the next task is to ensure proper storage of CO_2 to prevent it becoming part of environment. It has been reported in IPCC [3] that the CO_2 can be stored in the deep aquifers, coal mines, depleted oil and gas fields, limestone, sandstones as shown in Figure 4. The CO_2 can also be used for enhanced oil recovery. The carbon dioxide must be stored at the depths of more than 800 m to obtain temperature and pressure at which the volume is minimum (super critical state i.e. 74 bar and 31 ^{0}C) [2]. Three types of geological formation are suitable for CO_2 trapping.

They are:

- Deep aquifers
- Depleted Oil and Gas fields
- Storage in unmined coal seams.

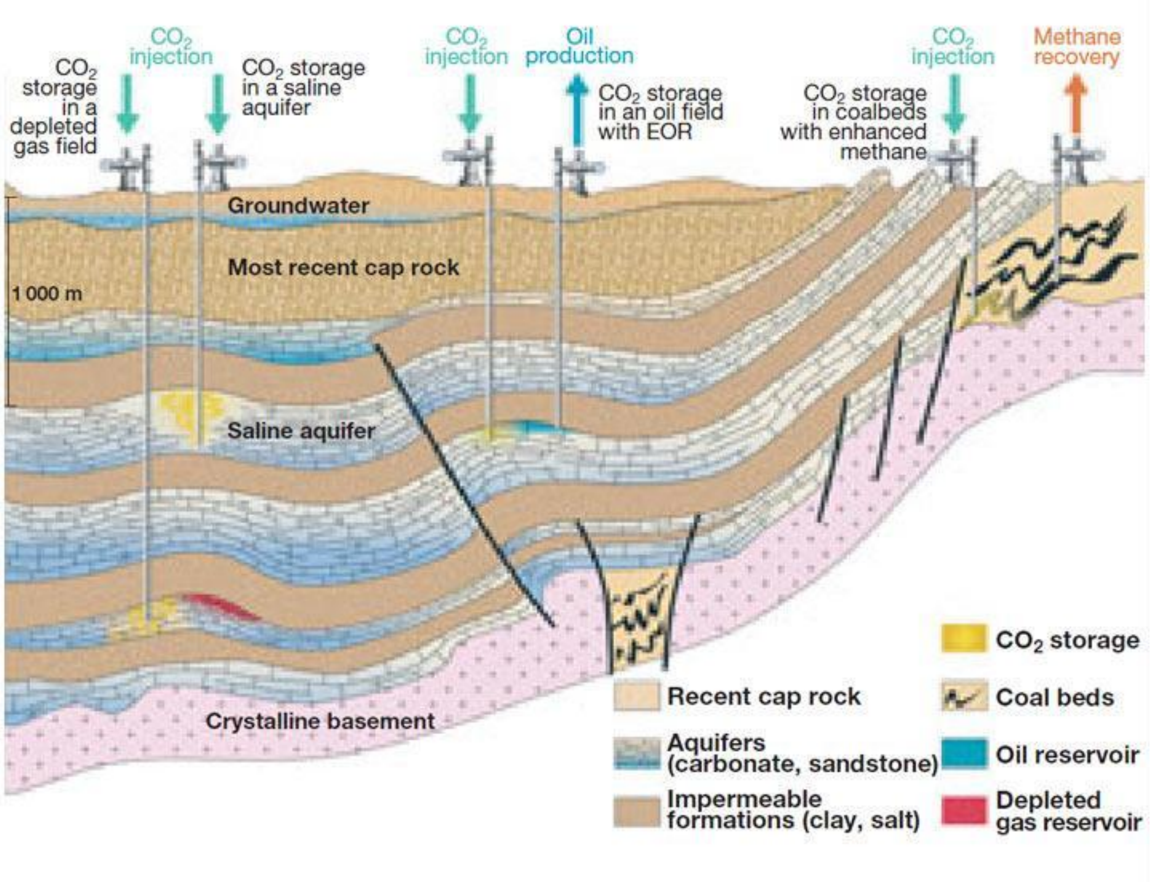

Figure 4: Various possibilities for the geological storage of CO_2 (Source: IFP-BRGM-ADEME-©BLCom)

Amongst different geological storage options, storage in deep aquifers is a favorite option as it offers largest storage capacity about ten times larger than oil and gas reservoirs. Figure 5 shows summary of potential reservoirs for geologically storing CO_2 in billion tons (Bt).

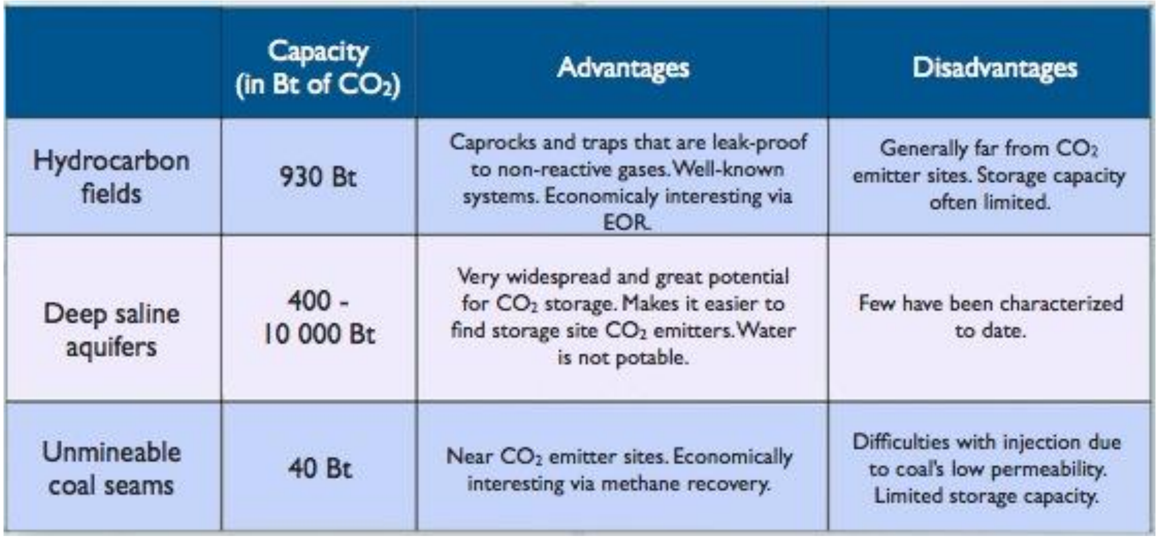

	Capacity (in Bt of CO_2)	Advantages	Disadvantages
Hydrocarbon fields	930 Bt	Caprocks and traps that are leak-proof to non-reactive gases. Well-known systems. Economicaly interesting via EOR.	Generally far from CO_2 emitter sites. Storage capacity often limited.
Deep saline aquifers	400 - 10 000 Bt	Very widespread and great potential for CO_2 storage. Makes it easier to find storage site CO_2 emitters. Water is not potable.	Few have been characterized to date.
Unmineable coal seams	40 Bt	Near CO_2 emitter sites. Economically interesting via methane recovery.	Difficulties with injection due to coal's low permeability. Limited storage capacity.

Figure 5: Potential reservoirs for geologically storing CO_2 [2]

1.4 Problem Statement

This study is focused on the storage of CO_2 in a tank, made of steel, filled with adsorbent. Charging process of CO_2 in steel tank at room temperature (T=295 K) is modeled using finite volume method with CFD commercial software ANSYS FLUENT. The storage tank dimensions are; length 'L' = 255mm, height 'H' = 48mm. CO_2 is fed to the tank at temperature T=295 K. Tank walls are kept at constant temperature. The adsorption model is based on modified Dubinin-Astakov (D-A) adsorption equation. Heat and mass transfer features of the numerical model are validated by the experiments of hydrogen adsorption on activated carbon performed by Hermosillalara et al. [5]. Axisymmetric geometric model of the storage system is shown below.

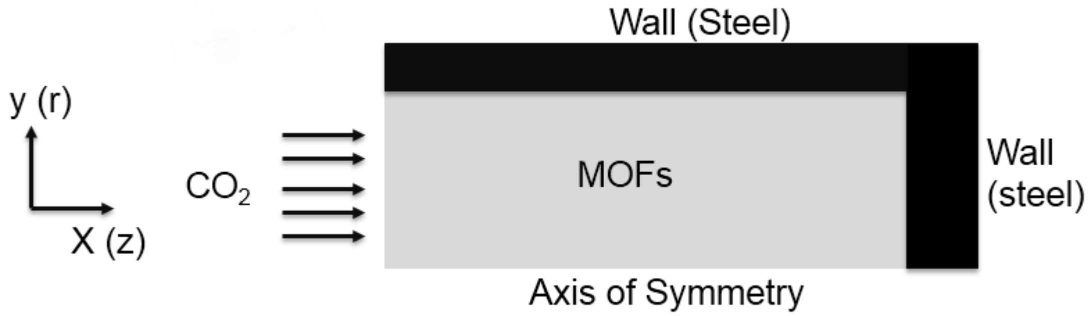

Figure 6: Axisymmetric geometric model of CO_2 storage system

Dubinin-Astakov (D-A) adsorption equation parameters like enthalpic factor, entropic factor, limiting pressure, limiting adsorption are found by regression analysis using CO_2 adsorption isotherm for different adsorbents. At tank entrance mass flux profile of CO_2 is established using user defined function (UDF). The Dubinin-Astakhov (D-A) adsorption model requires inclusion of source terms to the transport equations as well as solving additional equations. These tasks are performed using UDF in FLUENT.

1.5 Research Objectives

The research objectives of this study are as follow:

- To validate numerical results with experimental data.
- To study, numerically, the effect of storage pressure and temperature on heat and mass transfer processes during adsorption.
- To study, numerically, the influence of viscous resistance and inertial resistance of porous media on heat and mass transfer during adsorption.
- To compare, numerically, uptake capacity of different MOFs and other CO_2 adsorbents under same charging conditions.

1.6 Thesis Outline

The thesis is comprised of five chapters.

Chapter 1 introduces the climate challenges and CO_2 emissions resulting global warming issues; need and availability of carbon capture technologies, problem statement of thesis and the research objectives set to accomplish in this work.

Chapter 2 focuses on literature review mainly related to carbon capture technologies, MOFs suitable for CO_2 capture, numerical modeling of gas adsorption process in different adsorbents.

Chapter 3 describes the methodologies related to numerical work, CFD model used to discretized and solve the domain of the problem, governing equations and laws that are required to solve for numerical modeling.

Chapter 4 focuses on numerical study and presents the validation of numerical model by means of experimental results of Hermosillalara et al. [5] in order to ensure reliability of numerical results. Numerical results of CO_2 adsorption for different adsorbents under different charging conditions, varying bed porosity and viscous and inertial resistances are presented. Comparison of different adsorbents under similar charging conditions is presented.

In chapter 5, the conclusion of this study is presented and the possible future recommendations are proposed for continuation of this study in order to further improve the performance of the CO_2 storage process via adsorption.

CHAPTER 2

LITERATURE REVIEW

2.1 Carbon Capture Technologies

Around 40% of energy demands are met by burning of coal subsequently making it the largest contributor in CO_2 emissions followed by liquid fuels (furnace oil and diesel) and then natural gas as shown in Figure 7.

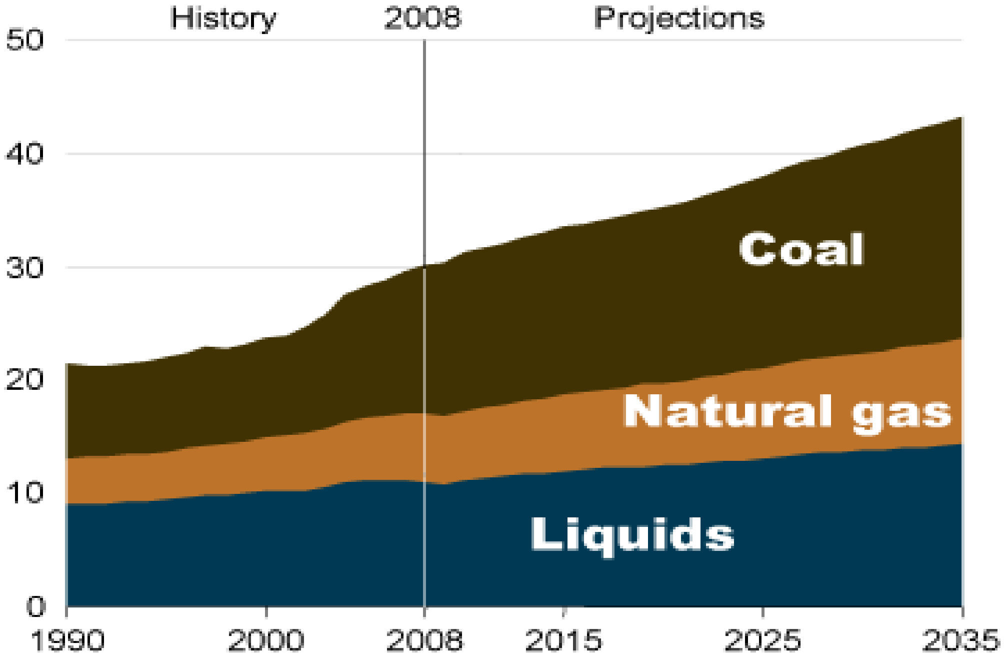

Figure 7: History and predictions of CO_2 emissions in Giga tons per annum by the usage of different fuels[6]

Up to 2008 the actual usage of each type of fuel is presented along with projections till 2035. Projections shows a considerable increase of coal utilization in energy sector. The CO_2 emissions may possibly rise up to 42 Giga tons per annum by 2035 [7]. Carbon Capture and Sequestration (CCS) is a promising technology to reduce CO_2 emissions. The development of CO_2 capture technologies (CCS) for hydrocarbon fired power and steam plants can be divided into three broad categories namely pre combustion, post combustion and oxy-fuel combustion. After separation of CO_2 from the flue gases, it is compressed and transported for sequestration.

Kunze and Spliethoff [8] evaluated all three CCS technologies for Integrated Gasification Combined Cycle (IGCC) Plants. In their work, IGCC concept based on oxy-fuel combustion exhibited a substantial improvement in efficiency reaching 45.74%. However implementation of this technique requires certain modifications and new equipment. The oxy-fuel combustion is one of the promising carbon capture technologies that can be used in the new plants and existing plants with some modifications [9]. The combustion of fuel in the presence of pure oxygen results very high temperatures however we have material constraints in directly implementing this technique. So CO_2 is re-circulated to reduce the overall temperature. The use of CO_2 as a carrier gas in the oxy-fuel combustion process reduces the flame speed compared to the nitrogen as reported by Law et al [10]. This results in the poor performance and temperature and species were different for nitrogen and for carbon dioxide cases. Andersson and Johnsson [11] performed experiments on combustion in O_2/CO_2 environment. Their results showed reduction in flame temperature when the burning fuel with the ratio of O_2/CO_2=21/79 as compared to the burning of fuel in air. They found that the combustion is delayed for ratio of oxygen to carbon dioxide on volumetric basis $O_2/CO_2=21/79$, the results for ratio $O_2/CO_2=27/73$ were better than the previous case.

Both pre-combustion and oxy-fuel combustion techniques require a dedicated air separation unit for Oxygen supply. Oxygen can be separated from air at very low temperatures (cryogenics), but it requires a lot of power for compression of air [12]. The available cryogenics plants have low second law efficiency normally in the range of 15-24% [13]. When implemented these plants can significantly reduce the overall efficiency of the power plants [14]. Extensive research has been going on for developing ion transport membranes (ITMs). Different membranes have been developed which are semi permeable for oxygen and provides high oxygen flux at high temperature when exposed to air and hydrocarbon. These membranes are efficient as compared to the cryogenics process.

In pre-combustion approach, the fuel is decarbonized removing all carbon contents prior combustion. For more than half a century this process is used for producing hydrogen in refineries, fertilizer and petrochemical plants, [15]. In this approach, fuel reacts partially at high pressure with oxygen or air and, in some cases, steam, to produce carbon monoxide (CO) and hydrogen (H_2). The CO then reacts with steam in a catalytic shift reactor to produce CO_2 and additional H_2. The hydrogen is used as fuel in a combined cycle plant for electricity generation and the CO_2 is then separated for sequestration.

The post-combustion technique can be easily retrofitted in the existing plants as compared to other techniques. In this approach, flue gases are passed through solvents or adsorbent beds where the CO_2 is separated by absorption or adsorption. Liquid solvents are usually amine based solvents such as MEA: Mono Ethanol Amine are used, MEA is used in different industries in CO_2 separation processes [16]. Recently a new class of porous materials, Metal Organic Frameworks (MOFs) are developed having high surface area. MOFs are better compared to liquid solvents in terms of energy consumption and ease of regeneration [17].

In oxy-fuel combustion, fuel is burnt in pure oxygen environment instead of air which eliminates the possibility of NO_x formation. However burning of fuel in pure oxygen gas results very high temperatures which most of the materials cannot withstand, so CO_2 has to be recycled as a carrier gas to reduce overall temperatures. The high concentration of CO_2 in the exhaust makes it more economical for downstream process as compared to other approaches. Removal of up to 98% of CO_2 is possible by oxy-fuel combustion [18].

The three approaches are summarized based on their merits and demerits in Table 1.

Table 1: Comparison between CCS approaches [2], [3], [6], [19]

S.No.	Technique	Advantages	Disadvantages
1.	Post combustion	➢ Can be retrofitted to existing plants ➢ Immediate solution	➢ Due to low conc. in exhaust, the separation is very costly. ➢ Net power decreases by 30%
2.	Pre combustion	➢ Carbon contents are removed before combustion ➢ Water gas shift reaction commercially practiced	➢ Hydrogen fired gas turbine are not commercially available. ➢ Net power decreases by 20% ➢ Dilution of H_2 is needed.
3.	Oxy-fuel combustion	➢ Removal of CO_2 up to 98% ➢ Combustion can be controlled by varying O_2/CO_2 ➢ No emissions at all.	➢ Modification and replacement of some equipment is needed ➢ Air separation is needed ➢ Net power decreases by 25%. (cryogenic separation)

2.2 Metal Organic Frameworks (MOFs) for CO_2 Capture

Any efficient adsorption medium must exhibit following two features to have long-term sustainability in CO_2 removal.

I. A periodic structure with fully reversible CO_2 adsorption and desorption capabilities.
II. A flexibility of the adsorbent structure to achieve optimized storage capacity by chemical functionalization and molecular level fine-tuning.

Fortunately Metal Organic Frameworks commonly known as MOFs represent a class of porous materials which shows aforementioned characteristics for CO_2 capture. MOFs are cage like structures composed of metallic nodes connected by a network of organic linkers.

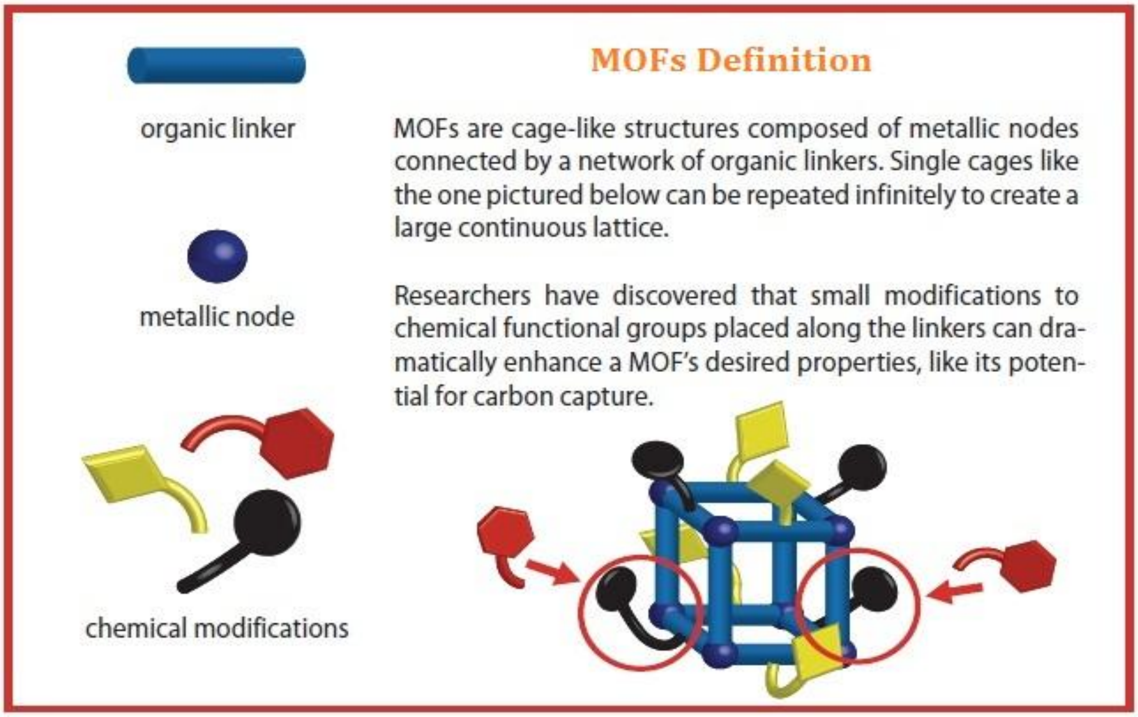

MOFs Definition

MOFs are cage-like structures composed of metallic nodes connected by a network of organic linkers. Single cages like the one pictured below can be repeated infinitely to create a large continuous lattice.

Researchers have discovered that small modifications to chemical functional groups placed along the linkers can dramatically enhance a MOF's desired properties, like its potential for carbon capture.

Figure 8: Chemistry of MOFs [20]

These single cages can be repeated infinitely to create a large continuous lattice. Researchers have discovered that small modifications to chemical functional groups placed along the linkers can dramatically enhance MOF's desired properties like its potential for carbon capture.

Extensive research is going on to develop MOFs having good selectivity and storage capacities for CO_2. Some of the MOFs identified for CO_2 capture include;

- Mg-MOF-74 (1,4-dioxido-2,5-benzenedicarboxylate)
- MOF-5 (Zn4O(BDC)3)
- COF-103 (C24H24B4O8Si)
- MIL-101 (Cr3OF(BDC)3)
- MOF-177 (1,3,5-benzenetribenzoate)

The desirable characteristics of MOFs for their potential use in carbon capture and sequestration technology are;

- High adsorption capacity for CO_2
- Low CO_2 desorption energy
- Good thermal stability
- Tolerance to contaminants
- Attrition resistance
- Resistance to moisture
- Adsorption selectivity that can be adjusted to suit the kinetic diameter of the molecules to be separated by varying organic binders used in synthesis.

In industries CO_2 is normally captured by chilling and compressing exhaust gases. Fluidized bed with aqueous amine solutions are also used through which exhaust gases or fumes are passed. However both aforesaid techniques are costly and relatively inefficient. Other methods include adsorption of CO_2 on oxide surfaces or within porous silicates, activated carbons etc. Millward and Yaghi [21] compared volumetric capacity of MOF-177 with zeolite 13X and Maxsorb. They found that MOF-177 filled container can capture two times the amount of CO_2 compared to zeolite 13X and Maxsorb filled container. Moreover MOF-177 filled container can store nine times the amount of CO_2 compared to the container without adsorbent.

Walton et al. [22] performed experiment for the adsorption of CO_2 on MOF-5 for a large temperature range and presented adsorption isotherms for CO_2. They found steps in isotherms while decreasing temperature. They presented a molecular model that predicts the inflections and steps which are in good agreement with the experimental data. This helps in explaining the adsorption mechanism. They performed Grand Canonical Monte Carlo (GCMC) simulation to get modeling results and compared these results with the experiment. Their model explains that the steps in adsorption isotherm is due to the attractive electrostatic interactions between CO_2 molecules. Hence with this model isotherm shapes can be predicted by using rigid crystal structure.

In equilibrium with pure CO_2, MOFs generally show remarkably high CO_2 storage. Pressure range used for CO_2 capture from stream of flue gases is 0.1 – 0.2 bar. Within this pressure range most MOFs exhibit low uptake capacity. Under dynamic conditions their uptake capacity reduces significantly when exposed to mixture of gases as in case of flue gases from power plants. To overcome these difficulties and to enhance their CO_2 capture selectivity extensive research work has been done. To obtain the desirable characteristics structural modifications are usually conducted in three ways: (i) metal ions; (ii) organic linkers; or (iii) combination of both metal ions and organic linkers. Britt et al. [23] reported that Mg-MOF-74, replete with open magnesium sites, exhibit excellent selectivity for CO_2 and facile regeneration. They performed breakthrough separation experiments for Mg-MOF-74 and reported that Mg-MOF-74 undergoes CO_2 release at considerably lower temperature i.e. 80 ^{0}C. Mg-MOF-74 challenges competitive materials for CO_2 capture with 8.9 wt. % dynamic capacity hence shows excellent balance between regeneration and dynamic capacity. In particular, when Mg-MOF-74 was subjected to a gas stream containing 20% CO_2 in CH_4, a percentage in the range of industrial separation conditions, it captured only CO_2 and not CH_4. Bae et al. [24] studied experimentally behavior of MOFs that are carborane-based or coordinated with a mixture of ligands and achieved higher selectivity for CO_2 compared to CH_4. Coal fired power plants typically produce 33% of the CO_2 which is released to the atmosphere, making them the primary target for CO_2 capture. At ambient conditions flue gases from the fossil-fuel fired power plants contain 3 to 16% of CO_2 by volume. The higher flow rates and low partial pressure makes it a challenging separation process. 14 different MOFs have been analyzed for their potential capabilities to capture CO_2 from flue gases for low pressure CO_2 uptake using experiment and with molecular modeling approach. It has been found that MOFs with high density of open metal sites are promising. Molecular modeling can be helpful in selection of adsorbents suitable for capturing CO_2 from flue gas [25].

Various adsorption techniques have been used for the separation of CO_2. Using temperature swing adsorption (TSA) technique, Mason et al. [26] evaluated MOF-177 and Mg-MOF-74 for their use in post-combustion CO_2 capture. They showed that the quantity adsorbed decreases with temperature for both gases as a result of the greater thermal energy of the molecules at higher temperatures. Additionally for both compounds, due to the greater quadrupole moment and polarizability of CO_2 compared to N_2, the quantity of CO_2 adsorbed is higher than that for N_2 at all temperatures.

Presence of water molecules in flue gas can degrade the molecular structure of MOFs. To study the effects of water on post-combustion CO_2 capture in Mg-MOF-74, Yu and Balbuena [27] performed Grand Canonical Monte Carlo (GCMC) and Density Functional Theory (DFT) simulations and found that presence of water molecules which are linked to coordinatively unsaturated metal sites (CUMs) decreases the CO_2 adsorption capacity of MOF. This is due to reduction of binding energy between CO_2 and water coordinated Mg-MOF-74. CUMs in MOFs play vital role in their potential use for CO_2 capture from a gaseous mixture containing moisture.

Based on the sorption / desorption temperatures, Wang et al. [28] classified the solid adsorbents into three types: (i) low temperature adsorbents (below 200 ^{0}C), (ii) intermediate temperature adsorbents (between 200 – 400 ^{0}C), and (iii) high temperature adsorbents (above 400 ^{0}C). MOFs, ZIFs, carbons, zeolites and amine based materials are low temperature CO_2 adsorbents.

MOFs are 1D, 2D and 3D crystalline compounds having metallic ions as nodes and organic linkers as binders. MOFs shape of assembly can be controlled by the types and connectivity of ions and linkers [29]. MOFs have high micropore porosity. Increasing micropore porosity increases surface area thus providing more sites for gas adsorption. This objective can be achieved by expanding the structure of MOFs by using longer linker lengths. However by using longer linkers often leads to a fragile framework. In addition due to strong binding energy between the frameworks, highly porous lattice structures often start to interpenetrate each other. This self-interpenetration prohibits high porosity and not desirable in MOFs for their potential use as gas adsorbents.

Zhao et al. [30] experimentally studied the adsorption equilibrium and diffusion phenomena of CO_2 on MOF-5 by the gravimetric method within pressure range up to 1atm. MOF-5 sample used for the analysis is of cubic crystals of 40 – 60 µm in sizes with specific surface area of 2517 m^2/g. MOF-5 has CO_2 adsorption capacity of 2.1 mmol/g (or 9.24%) at 295.7 K and 1 atm. For MOF-5, CO_2 adsorption isotherms can be well described by Freundlich adsorption isotherm equation. CO_2 diffusion in MOF-5 crystals is an activated process with diffusivity in the range of $8.1\text{-}11.5 \times 10^{-9}$ cm^2/s in 295-331 K and activation energy for diffusion of 7.6 kJ/ mol. The CO_2 pressure (or loading) has negligible effect on the rate of CO_2 diffusion in MOF-5 crystals.

2.3 Numerical Modeling of Gas Adsorption

In addition to enormous experimental work, computational efforts have also been made to investigate and predict the characteristics and applications of adsorption process of gas on solid surfaces.

Hermosillalara et al. [5] studied thermal effects during charging process of hydrogen storage tank packed with activated carbon. They performed experimental tests and compared simulation results with the experimental data to validate their numerical model. Their storage tank was a cylindrical stainless steel column, six thermocouples were attached along the column to get axial and radial temperature profiles. Digital pressure transducer was also attached at the bottom of column. The experiments were carried out at 10 MPa. Throughout the charging process the temperature and pressure variation along the axial and radial direction were recorded with the help of data accusation system. The numerical model used was based on mass, momentum and energy conservation equations for flow through porous media and Dubinin-Astakov model.

Adsorption isotherms for hydrogen, nitrogen and methane over activated carbon at higher pressure and superficial temperatures have been studied by Richard et al. [31]. The model was developed with the objective to fit the experimental data accurately over the whole temperature and pressure ranges. Dubinin-Astakov (D-A) model was adapted by using fitting parameters for the saturation pressure and limiting adsorption. It has been found that addition of entropic factor produces good results. Moreover D-A model best fits the experimental data.

Heat and mass transfer phenomena during charging of hydrogen in a stainless steel storage tank packed with activated carbon have been studied by Xiao et al. [32]. Charging process was simulated at room temperature (295K) and medium storage pressure (10 MPa) using finite volume commercially available software FLUENT. They found that temperature near the bottom of the tank is higher compared to entrance. Also temperature in the center of the tank is higher than that near the wall and rise in temperature along the axial direction is higher compared to radial direction because axial velocity is higher than the radial component. At the entrance of the tank, absolute adsorption of hydrogen is maximum. Moreover they compared simulation results with the experimental data available and found good agreement between the two. In addition to adsorption, desorption cycle was also simulated by Ye et al. [33] for hydrogen over activated carbon at room temperature (302K) and medium storage pressure (10 MPa). Simulation results showed that temperature in central region of the tank is higher than that near the walls during charging process. While temperature in central region is lower than that near the walls during discharging process. The amount of adsorbed hydrogen was greater than that of compressed gaseous hydrogen which tells that hydrogen storage by adsorption on high surface area activated carbon is better.

Charge-discharge cycles of the two MOF-5 samples (powder and compacted tablet) were simulated by means of finite element analysis software Comsol Multiphysics^{TM}, and compared with activated carbon [34]. The adsorption process was modelled using modified Dubinin-Astakhov (D-A) adsorption isotherm. Maximum pressure in powder MOF-5 tank is much higher than that in the activated carbon tank due to lower adsorbent density of MOF-5 consequently resulting lower adsorption of hydrogen. Maximum pressure in compacted MOF-5 is a little bit lower than that in the activated carbon due to higher adsorbent density resulting higher adsorption of hydrogen. The temperate swings during charge-discharge cycle in MOF-5 tanks are higher than that of activated carbon.

Xiao et al. [35] performed finite element simulation of charging and discharging processes of cryo-adsorptive hydrogen storage in a steel tank filled with activated carbon using Comsol Multiphysics^{TM}. A modified Dubinin-Astakhov (D-A) model was adapted to express the relationship between hydrogen adsorption density, pressure and temperature in the tank. The pressure rises sharply from initial value to 9 MPa during the charging. During the discharge process, the pressure drops quickly as hydrogen flows out of the tank. Due to small pressure gradient the pressure distribution in the tank is uniform.

Absolute adsorption density at different locations remains uniform during charging and discharging. Absolute adsorption depends on local temperature and pressure. As the pressure distribution is uniform throughout the tank, the absolute adsorption amount is maximum where the temperature is minimum and the absolute adsorption is minimum where the temperature is maximum [36].

Bai [37] and Bai et al. [38] performed two dimensional, time accurate simulations of adsorption / desorption of n-butane in a carbon canister having activated carbon BAX950 as adsorbent. They implemented Dubinin-Polnayi adsorption potential model for the adsorption phenomena of n-butane at ambient pressure by writing user defined functions (UDF) incorporated in CFD package FLUENT. Nitrogen gas was used as carrier gas. They studied effect of varying concentrations of n-butane on adsorption phenomena and initial carbon bed equilibrium adsorption states on desorption phenomena. Linear Driving Force (LDF) model which adequately describes the mass transfer phenomena in adsorption process was used for the calculation of heat and mass transfer by several researchers [39]–[41] in their work on adsorption beds and columns.

Lavoie et al. [42] used one dimensional adsorption model to predict the performance of fixed bed canisters in vehicle evaporative emissions control system. The model describes the mass transfer and transient thermal phenomena in carbon canisters and accurately predicts the hydrocarbon removal rates, mass of hydrocarbon adsorbed by the canister and breakthrough times. However model poorly predicts the local bed temperatures at maximum purge and loading rates. Experiments were performed by Liu and his research group [43]–[45] for separation and recovery of butane vapor from nitrogen gas using BAX activated carbon. Cooney [46] numerically studied adiabatic fixed bed adsorption phenomena. Langmuir equilibrium distribution relation and linear driving force model were used for heat and mass transfer in adiabatic adsorption beds. The effects of heat and mass transfer coefficients, inlet feed concentration and heat of adsorption were investigated. They found that maximum temperature rises which occur can actually be larger for solutes having smaller heats of adsorption, under certain conditions.

CHAPTER 3

METHODOLOGY

3.1 Numerical Modeling

3.1.1 Governing equations

The governing equations to describe the adsorption of gas flowing through porous media include conservation of mass, momentum, energy equations and adsorption amount. During adsorption process gas is being adsorbed by the adsorbent and also being an exothermic process heat is released during adsorption phenomena. This results in the fluid mass and momentum loss and a rise of temperature of the adsorbate/adsorbent system. Theses phenomena are taken into account by adding source or sink term to the corresponding governing equations.

3.1.1.1 Mass conservation equation

The mass conservation equation in porous media can be expresses as [32];

$$\frac{\partial\left(\varepsilon_b \rho_g\right)}{\partial t} + \nabla.\left(\rho_g \vec{v}\right) = S_m \tag{1}$$

Where

ε_b = Bed porosity

ρ_g = Gas density

$\vec{v}$ = Superficial velocity vector

S_m = Mass source term

Mass source term corresponds to the mass added to the adsorbed phase from the gaseous phase in unit volume per second. Mass source term can be described as [47];

$$S_m = -\left(1-\varepsilon_b\right)\rho_p M_g \frac{\partial n_a}{\partial t} \tag{2}$$

Where

ρ_p = Particle density of the adsorbent

M_g = Molecular mass of the gas

n_a = Absolute adsorbed amount of the gas per unit mass of the adsorbent

3.1.1.2 Momentum conservation equation

The momentum conservation equation for porous media can be expressed as [32];

$$\frac{\partial}{\partial t}\left(\rho_g \vec{v}\right) + \nabla.\left(\rho_g \vec{v}\vec{v}\right) = -\nabla p + \nabla.\left(\overline{\overline{\tau}}\right) + \rho_g \vec{g} + \vec{S} \tag{3}$$

Where

$\overline{\overline{\tau}}$ = Stress tensor

$\vec{S}$ = Momentum source term

Momentum source term represents the additional friction due to porous media and describes the viscous and inertial losses. For simple homogeneous porous media, its component in *i-direction* can be expressed as [32];

$$S_i = -\left(\frac{\mu}{C_1} v_i + C_2 \frac{1}{2} \rho_g \left| \vec{v} \right| v_i \right) \tag{4}$$

The negative source term contributes to the pressure gradient in porous cell creating pressure drop.

Where

μ = Dynamic viscosity of the gas

C_1 = Permeability

$\frac{1}{C_1}$ = Viscous resistance coefficient

C_2 = Inertial resistance coefficient

Viscous resistance and Inertial resistance co-efficient can be identified as [32];

$$C_1 = \frac{D_p^2}{150} \frac{\varepsilon_b^3}{\left(1-\varepsilon_b\right)^2} \tag{5}$$

$$C_2 = \frac{3.5}{D_p} \frac{\left(1-\varepsilon_b\right)}{\varepsilon_b^3} \tag{6}$$

3.1.1.3 Energy conservation equation

ANSYS FLUENT solves the standard energy transport equation for porous medium with modifications in conduction flux and transient terms only. For simulations where thermal equilibrium is assumed between porous medium and fluid flow, conduction flux in porous media uses an effective conductivity and transient term includes the thermal inertia of the solid region on the medium [32].

$$\frac{\partial}{\partial t}\left[\varepsilon_b \rho_g E_g + \left(1-\varepsilon_b\right)\rho_p E_s\right] + \nabla.\left[\vec{v}\left(\rho_g E_g + p\right)\right] = \nabla.\left(k_{eff}\nabla T - \sum_i h_i \overrightarrow{J_i} + \overline{\overline{\tau}}.\vec{v}\right) + S_h \quad (7)$$

Where

E_g = Total gas energy

E_s = Energy of solid phase

k_{eff} = Effective thermal conductivity of the medium

S_h = Energy source term

h_i = Species enthalpy along *i* direction

$\overrightarrow{J_i}$ = Diffusion flux of species along *i* direction

The energy source tern can be expressed as [32];

$$S_h = -\frac{\Delta H . S_m}{M_g} \quad (8)$$

Where

ΔH = Isosteric heat of adsorption

The effective thermal conductivity in the porous media is computed as the volume average of the gas conductivity and the solid phase conductivity and is expressed as [32];

$$k_{eff} = \varepsilon_b k_g + \left(1 - \varepsilon_b\right) k_s \tag{9}$$

Where

k_g = Thermal conductivity of the gas

k_s = Thermal conductivity of the solid phase

3.1.2 Modified Dubinin-Astakhov (D-A) adsorption model

A modified Dubinin-Astakhov (D-A) micropore volume filling adsorption model is used to describe the adsorption isotherm. The absolute adsorption can be expressed as [31];

$$\theta = \frac{n_a}{n_{\max}} = \exp\left[-\left(\frac{A}{E}\right)^m\right] \tag{10}$$

Where

θ = Degree of filling of volume of micropores

$n_{\max}$ = Limiting adsorption

A = Differential molar work of adsorption or adsorption potential

E = Characteristic free energy of adsorption

Differential molar work of adsorption can be expressed as [31];

$$A = RT \ln\left(\frac{P_o}{P}\right) \tag{11}$$

Where

P_o = Limiting pressure

R = Universal gas constant

Characteristic free energy of adsorption can be expressed be the following equation [31];

$$E = \alpha + \beta T \tag{12}$$

Where

α = Enthalpic factor

β = Entropic factor

Substituting Equations (11) and (12) in equation (10), the equation for absolute adsorption can be expressed as;

$$n_a = n_{\max} \exp\left[-\left(\frac{RT}{\alpha + \beta T} \ln \frac{P_o}{P}\right)^m\right] \tag{13}$$

3.1.3 CFD approach

In this work, the adsorption model is based on modified Dubinin-Astakov (D-A) adsorption equation. Simulations are performed using finite volume method using CFD commercially available software ANSYS FLUENT 14.5. The finite volume is a conservative method, for discretization of the governing equations. The domain is divided into rectangular elements; each element represents a finite volume, and the discretized equations are solved for each finite volume element. Solving momentum equation along with the other equations is difficult because of the presence of pressure gradient term. Therefore, a staggered grid is used for the simulations as recommended by Versteeg and Malalasekera [48]. All the scalars are calculated at the grid point, whereas, velocities are computed at the center of the cell. Gambit 2.4 software is used to generate the geometry for meshing purpose. After the generation of the grid, it is imported to the FLUENT software and all remaining operations for setting up the case are performed within the solver. Simulations are performed using double precision solver. Gradients are calculated using Least Squares cell-based method. For pressure-velocity coupling, the SIMPLE algorithm (semi-implicit method for pressure-linked equations) is used. The second order upwind scheme is sued for the discretization of momentum, energy and other scalar equations. First order implicit transient formulation is used. Solution is assumed to be converged when residuals drops below 10^{-6} for all equations.

The Dubinin-Astakhov (D-A) adsorption model requires inclusion of source terms to the transport equations, as well as, solving additional equations. These tasks are performed through the incorporation of user defined functions (UDFs) into the FLUENT CFD solver. The UDFs are subroutines written in C++, and they can be accessed by the CFD solver during the calculations. DEFINE_ADJUST function is a general purpose macro which is used to adjust or modify the FLUENT variables that are not passed as arguments. Absolute adsorption as given in equation (14) is defined as a scalar quantity and it is called by the CFD solver during the calculations through the execution of the UDF by the DEFINE_ADJUST macro. During adsorption, gas is adsorbed by the adsorbent hence mass conservation equation must add mass source term. Adsorption is an exothermic process and heat is liberated during adsorption. The mass source term and energy term are incorporated using DEFINE_SOURCE macro.

3.1.4 Material and flow properties

The adsorption system under study comprises of CO_2 gas as adsorbate and a steel tank as storage container filled with different adsorbents like BPL 4X10 activated carbon, 13X zeolite and Mg-MOF-74. Material properties of the adsorbents are shown in Table 2. Material properties of CO_2 gas and steel walls of the storage tank are shown in Table 3.

Table 2: Material properties of adsorbents

	Activated carbon	**Zeolite**	**Mg-MOF-74**
Particle density (kgm^{-3})	916	1357	1510
Average particle diameter (mm)	1.3	1.5	0.02
Specific heat capacity (JKg^{-1}K^{-1})	825	780	836
Thermal conductivity (Wm^{-1}K^{-1})	0.764	0.32	0.2
Viscous resistance coefficient (m^{-2})	35.689e6	26.806e6	1.5078e11
Inertial resistance coefficient (m^{-1})	3184	2759.5	206959.4
Isosteric adsorption heat (Jmol^{-1})	20900	31600	22000

Table 3: Material properties of CO_2 and Steel

CO_2 Gas	Density (kgm^{-3})	Ideal gas
	Specific heat capacity (JKg^{-1}K^{-1})	Piecewise-Polynomial
	Thermal conductivity (Wm^{-1}K^{-1})	Kinetic Theory
	Viscosity (Pa.s)	Kinetic Theory
Steel wall	Density (kgm^{-3})	7830
	Specific heat capacity (JKg^{-1}K^{-1})	468
	Thermal conductivity (Wm^{-1}K^{-1})	13

In an adsorption system there are three porosities; micropore porosity “ε_{mi}” which contributes to the adsorption process, macropore porosity “ε_{ma}” same as bed porosity ε_b and “ε_t” total porosity. These porosities are related with each other though following expression [32]:

$$\varepsilon_t = \varepsilon_{mi} + \varepsilon_{ma} \tag{14}$$

We assume that the macropore porosity provides flow path to the gas flowing though the adsorption bed [31]. In this study, bed porosity is varied from 0.66 to 0.78 to study its effect on heat and mass transfer processes of the adsorption system.

3.1.5 User defined function (UDF)

The Dubinin-Astakhov (D-A) adsorption model requires inclusion of source terms to the transport equations as well as solving additional equations. These tasks are performed using UDF in FLUENT. User Defined Functions (UDF) are subroutines written in C-language, accessed by FLUENT during solution subsequently increasing the solution capability of FLUENT.

DEFINE_ADJUST a general purpose macro is used to adjust or modify the FLUENT variables that are not passed as arguments. Absolute adsorption as given in equation (13) is defined as scalar quantity and is called by the FLUENT by executing UDF using DEFINE_ADJUST macro.

The function C_T (c , t) is used to obtain cell temperature. C_P (c , t) is is used to obtain pressure of cell. RP_Get_Real is used to obtain operating pressure of the cell. The function C_UDSI is used to store absolute adsorption of a cell at every iteration.

During adsorption, gas is adsorbed by the adsorbent hence mass conservation equation must add mass source term. Adsorption is an exothermic process and heat is liberated during adsorption. The mass source term and energy term are incorporated using DEFINE_SOURCE macro.

3.1.6 Boundary conditions

DEFINE_PROFILE is a general purpose macro and is used to define custom boundary profile that varies as function of spatial coordinates or time. F_PROFILE is used in DEFINE_PROFILE UDF to set the mass flux boundary condition at the inlet. A mass flux profile corresponding to mass flow rate 1e-3 kgs^{-1} is applied as inlet boundary condition using UDF.

In this work gas entrance temperature is set as 295K. The storage tank walls are kept at a constant temperate i.e. 295K. In order to investigate the effect of storage pressure, operating pressure is varied from 20 kPa to 100 kPa.

3.2 Regression Analysis

Regression analysis is used for modeling the relation between response variables and predictors [49]. These response variables are also known as dependent variables, predicted variables, or regressands. The predictors are commonly known as independent variables, explanatory variables, or regressors. The approach is mainly used to identify the mathematical dependency of one random variable to another random variable. This mathematical model can be used to estimate the dependent variable for any given instance of the independent random variable. In my work, the mathematical dependence of absolute adsorption is analyzed using regression analysis. The regression model helps estimating the unknown parameters of Dubinin-Astakhov (D-A) model parameters.

3.2.1 Types of regression models

Regression models and its application depend upon the type of problem [49]. There are various regression models developed for particular use and the most familiar types are mentioned below.

1. Linear Regression
2. Non Linear Regression
3. Multiple regression
4. Logistic regression

5. Stepwise regression

6. GLM: generalized linear models

7. GLMM: generalized linear mixed models

The most elementary type of regression model is the simple linear regression model in which there is only one independent variable and the relationship is linear between response variable and predictor [50]. The model for simple linear regression is expressed by the following equation:

$$Y_i = \beta_0 + \beta_1 X_i + \varepsilon_i \tag{15}$$

Where,

Y_i = Dependent Variable

β_0 = Population Y intercept

β_1 = Population Slope Coefficient

X_i = Independent Variable

ε_i = Random Error term

Multiple Regression model is employed where there are a number of independent parameters. The following equation shows Multiple Regression Model with k Independent Variables.

$$\mathrm{Y_i = \beta_0 + \beta_1 X_{1i} + \beta_2 X_{2i} + \cdots + \beta_k X_{ki} + \varepsilon_i} \tag{16}$$

Where,

β_0 = Y intercept

β_1 = Population Slopes

The accuracy of linear regression is measured by the coefficient of determination. It is the part of the whole difference in the dependent parameter that is explained by change in the independent parameter. [51]

The coefficient of determination is also called r-squared and is denoted as r^2.

$$r^2 = \frac{SSR}{SST} = \frac{\text{regression } \textit{sum} \text{ of squares}}{\textit{total} \text{ sum of squares}}$$

The value of r^2 is from 0 to 1.

Another technique for regression analysis is called non-linear regression. In non linear regression, the relationship between the dependent parameter and an independent parameter is defined using quadratic model.

The general non-linear regression model is expressed as:

$$Y_i = \beta_0 + \beta_1 X_{1i} + \beta_2 X_{1i}^2 + \varepsilon_i \tag{17}$$

Where,

β_0 = Y intercept

β_1 = regression coefficient for linear effect of X on Y

β_2 = regression coefficient for quadratic effect on Y

ε_i = random error in Y for observation i

The testing of significance for quadratic model is carried out by comparing the value of r^2 and r^2_{adj}. If adj. r^2 resulting from the quadratic model is bigger than the r^2 from the linear model, then the quadratic model will perform better. [49] - [50]

After the development of regression model, goodness of fit test is performed along with statistical importance of the predictable parameters [52]. Generally used goodness of fit test includes the R-squared, residuals pattern and hypothesis testing. Statistical importance is verified using t-tests and f test for individual and complete fit respectively.

The parameters of modified D-A adsorption model are obtained, using regression analysis, from a curve fitting to experimental adsorption isotherm of CO_2 for BPL 4X10 activated carbon [53], 13X zeolite [53] and Mg-MOF-74 [54]. The parameters are given in Table 4. Distribution parameter “m” in D-A model is taken 1.38 for activated carbon and 1.60 for zeolite and Mg-MOF-74.

Table 4: Modified D-A model Parameters of adsorbents

Adsorbents	α	β	$n_{\max}$	P_o
Activated Carbon (BPL)	608.3	25.83	60.65	430
Zeolite 13X	893.5	68.7	10.98	800
Mg-MOF-74	134.1	69.13	25.15	600

3.3 Solution Procedure

In FLUENT, when UDFs are included in the solution procedure, the solution process starts with the default initialization function. Then the iteration loop begins with executing user defined adjust function. After that, conservation equations are solved, progressing from momentum conservation equations and subsequent pressure correction equation to the additional relevant scalar equations. After conservation equations, the properties are updated including user defined properties. A check for either convergence or further iterations is done and the loop either continues or stops. Detailed explanations of the steps within the iterations are as follows;

1. Based on current solution, fluid properties are updated. If the calculation has just begin, fluid properties are updated based on initialized solution.
2. The u, v and w momentum equations are solved sequentially using current values of pressure and face mass fluxes, in order to update the velocity field.
3. Since the velocities obtained in above step may not satisfy the continuity equation locally, a pressure correction equation is derived from the continuity equation and linearized momentum equations. This pressure correction equation is then solved to obtain corrected pressure and velocity fields and face mass fluxes such that continuity equation is satisfied.
4. Where appropriate, equations for energy and other scalars are solved using previously updated values of other variables.
5. A check for convergence of equations set is made.
6. These steps are repeated until convergence criteria is fulfilled.

Figure 9 gives the illustration of this process.

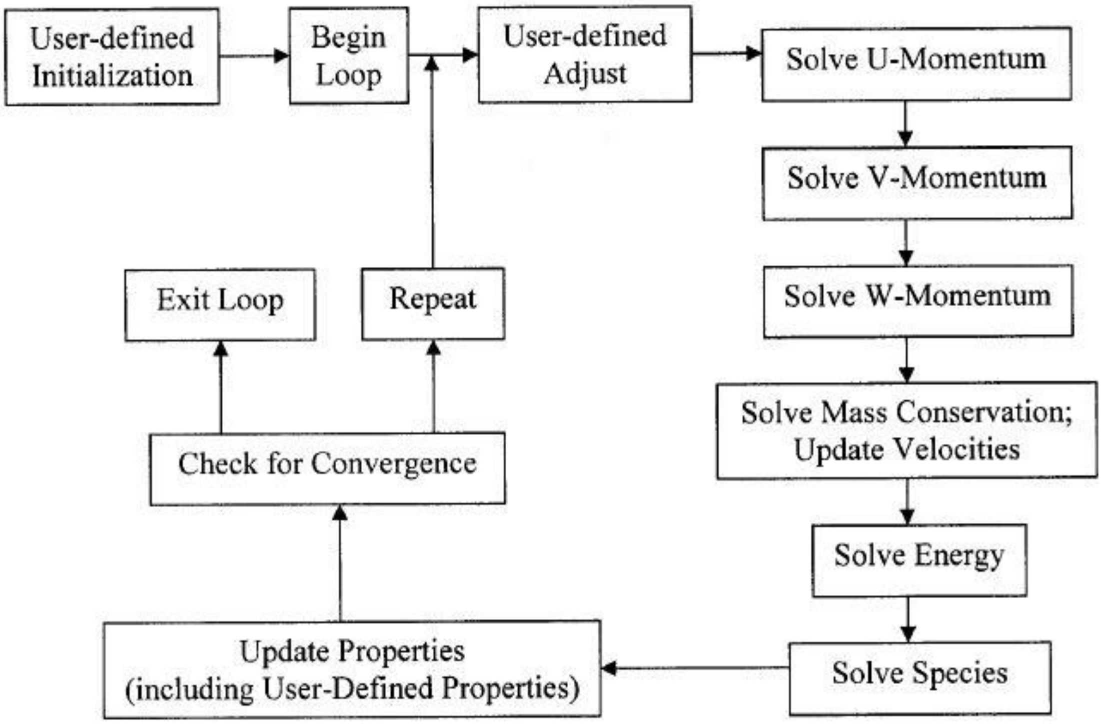

Figure 9: Solution procedure of FLUENT solver with UDF [37]

CHAPTER 4

RESULTS AND DISCUSSION

This chapter focuses on the numerical study that includes validation of the numerical model with the experimental work of Hermosillalara et al. [5] to ensure reliability of the numerical results for adsorption of CO_2 in different adsorbents. Moreover this chapter also presents the detailed results with critical analysis to better understand the phenomena of adsorption in different adsorbents namely activated carbon, zeolite 13X and Mg-MOF-74. A comparison of adsorbents for uptake capacity of CO_2 under similar charging conditions is also presented.

4.1 Validation of Numerical Model

4.1.1 Geometry model for hydrogen adsorption in activated carbon

A 2D axisymmetric geometric model used for the adsorption of Hydrogen in a steel tank filled with activated carbon is shown in Figure 10 using commercially available software GAMBIT 2.4 which is widely used for geometry and mesh generation. The x direction is along the length of the adsorption bed and y direction is along the height of the adsorption bed. The domain of the reactor is meshed into 12,240 rectangular elements or quadrilateral cells. The grid is made uniform throughout the domain. Since the heat transfer phenomena within the steel tank walls is not much significant, as there is not much rise in temperature within the bed during adsorption and also temperature of walls is kept constant at 295K during charging phase, walls thickness is neglected to make computation easier. The storage tank dimensions are; length ‘L’ = 255mm, height ‘H’ = 48mm. Variation of temperature, pressure and adsorption is recorded at six different points as shown in Figure 10. Experimental temperature results for these six points are available to compare the numerical results with the experimental data [5].

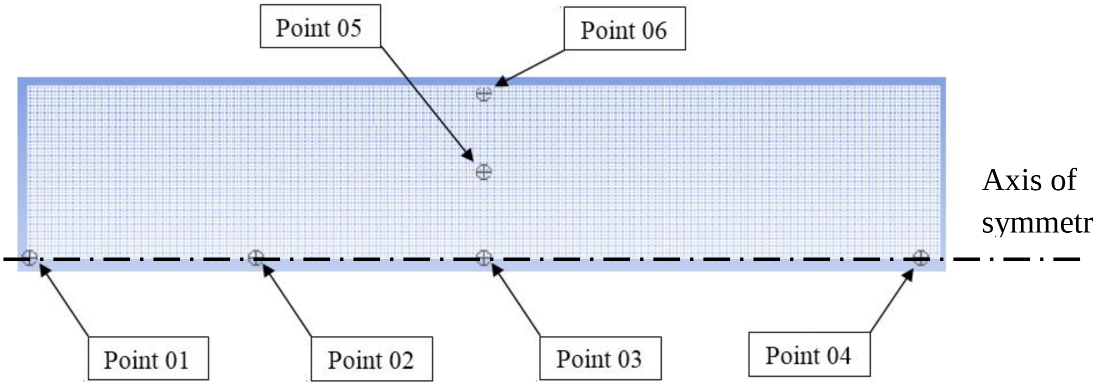

Figure 10: Geometric model of adsorption bed

The six monitoring points and there locations are shown in the Table 5 below. Monitoring temperature at these points enables us to investigate the temperature variation both axially and radially and to compare them with the experimental data [5].

Table 5: Coordinates of monitoring points

Sr. No.	**Axial Distance**	**Radial Distance**
Point 01	0	0
Point 02	L/4	0
Point 03	L/2	0
Point 04	L-5mm	0
Point 05	L/2	H/2
Point 06	L/2	H-2mm

4.1.2 Material and flow properties for validation case

The adsorption system under study comprises of hydrogen gas as adsorbate, activated carbon as adsorbent and steel tank as storage container. Material properties of the adsorption system are shown in Table 6 below.

Table 6: Material properties of adsorption system

Activated Carbon	Particle density (kgm^{-3})	702.4
	Average particle diameter (mm)	2
	Specific heat capacity (JKg^{-1}K^{-1})	825
	Thermal conductivity (Wm^{-1}K^{-1})	0.764
	Bed porosity	0.66
Hydrogen Gas	Density (kgm^{-3})	Ideal gas
	Specific heat capacity (JKg^{-1}K^{-1})	14700
	Thermal conductivity (Wm^{-1}K^{-1})	0.206
	Viscosity (Pa.s)	8.411e-6
Steel wall	Density (kgm^{-3})	7830
	Specific heat capacity (JKg^{-1}K^{-1})	468
	Thermal conductivity (Wm^{-1}K^{-1})	13

Viscous resistance and inertial resistance coefficient can be calculated using equations 5 and 6 respectively.

$$C_1 = \frac{D_p^2}{150} \frac{\varepsilon_b^3}{\left(1-\varepsilon_b\right)^2}$$

$$C_2 = \frac{3.5}{D_p} \frac{\left(1-\varepsilon_b\right)}{\varepsilon_b^3}$$

Using above two equations viscous and inertial resistances are calculated as;

$\frac{1}{C_1}$ = Viscous resistance coefficient = 1.50786 e+7 (m^{-2})

C_2 = Inertial resistance coefficient = 2070 (m^{-1})

Isosteric heat of adsorption is assumed to be constant and is equal to;

ΔH = Isosteric heat of adsorption = 3185 (J mol^{-1})

4.1.3 Dubinin-Astakhov (D-A) model parameters

The parameters of D-A adsorption model are obtained, using regression analysis, from a curve fitting to experimental adsorption isotherm of hydrogen on activated carbon AX-21 at 77K with R-square = 0.99, Adjusted R-square = 0.99 and RMSE = 0.0001991, and is compared with the parameters presented by Richard et al. [31] as shown in Table 7 below.

Table 7: Modified D-A model parameters for validation case

Parameter	**Present study**	**Richard et al. [31]**
n_{max} (mol kg^{-1})	71.59	71.6
P_0 (MPa)	1469	1470
α	3092	3080
β	19.2	18.9

4.1.4 Boundary conditions

In reality, hydrogen gas is fed to the storage tank through a small pipe of 2mm diameter, including this inlet pipe is not necessary and will make the computation complex [5]. So, the whole inner radius of the storage tank is considered as the inlet for hydrogen gas. During charging phase the walls of the storage tank are kept at constant temperature at 295K. A mass flux profile corresponding to mass flow rate 1e-4 kgs^{-1} is applied as inlet boundary condition using UDF based on multiple fitted expression [32] and is shown in Table 8 below.

Table 8: UDF for mass flux

```
if(flow_time<=119)
      F_PROFILE(f,t,i)=1.3815533E-02-flow_time*1.09986554E-06;
else if(flow_time<=224)
      F_PROFILE(f,t,i)=0.02773874-flow_time*1.181003E-04;
else if(flow_time<=248)
      F_PROFILE(f,t,i)=-3.05396E-05*flow_time+8.124988E-03;
else if(flow_time<=510)
      F_PROFILE(f,t,i)=-2.1036911E-06*flow_time+1.0728825E-03;
else if(flow_time<=600)
      F_PROFILE(f,t,i)=0;
```

4.1.5 Validation results

Comparison of numerical and experimental temperature profiles at different locations within the adsorption bed are shown in Figures 11 – 15. The inlet temperature is almost constant during all the charging phase, while the hottest region is found to be at the same location as determined experimentally, i.e. at the center of the tank. The maximum value of the temperature in the center of the tank is around 347 K as found experimentally. Whereas numerical model predicts the maximum temperature value at the center of the tank to be around 345 K. The highest temperature at the tank center is due to bad heat transfer from the central region to the walls of the container as thermal conductivity of the activated carbon bed is low. Moreover, convective effect of fresh hydrogen gas is weaken at the center.

Similarly the amplitude of temperature increase predicted by the numerical model at points 02, 03, 05 and 06 is similar to the experimentally obtained temperature profiles. The time instants where temperature peaks appear are almost identical for different locations. However small deviation between temperature profiles predicted by present numerical model and the experimental results have been observed such as at points 02 and 04. This might be due to the reasons that bed porosity is assumed to be isotropic and isosteric heat of adsorption is taken constant however it is generally a function of the adsorbed gas. Moreover FLUENT uses a superficial velocity inside the porous medium, based on the volumetric flow rate, to ensure continuity of the velocity vectors across the porous medium interface. This superficial velocity formulation does not take porosity into account when calculating the convection and diffusion terms of the transport equations.

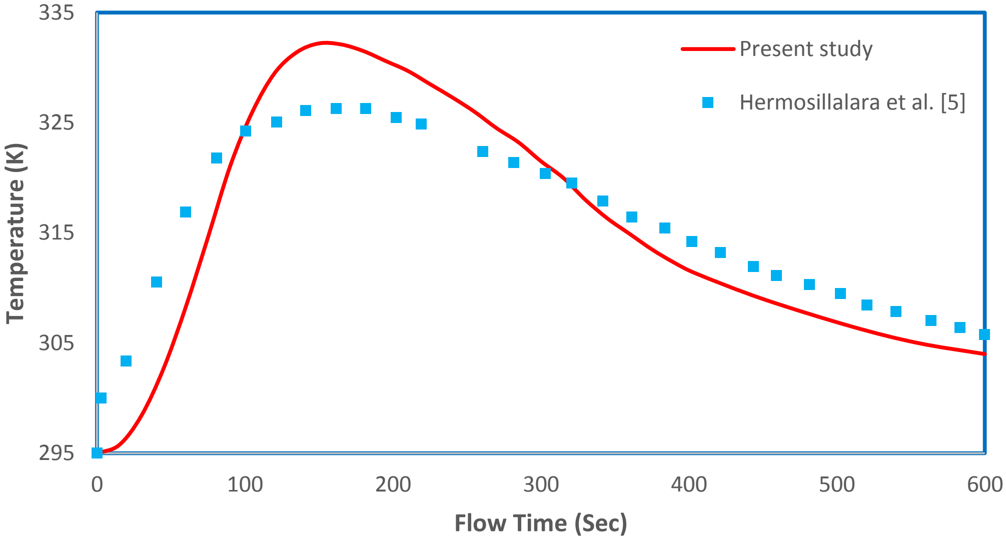

Figure 11: Temperature profile during charging phase at point 02

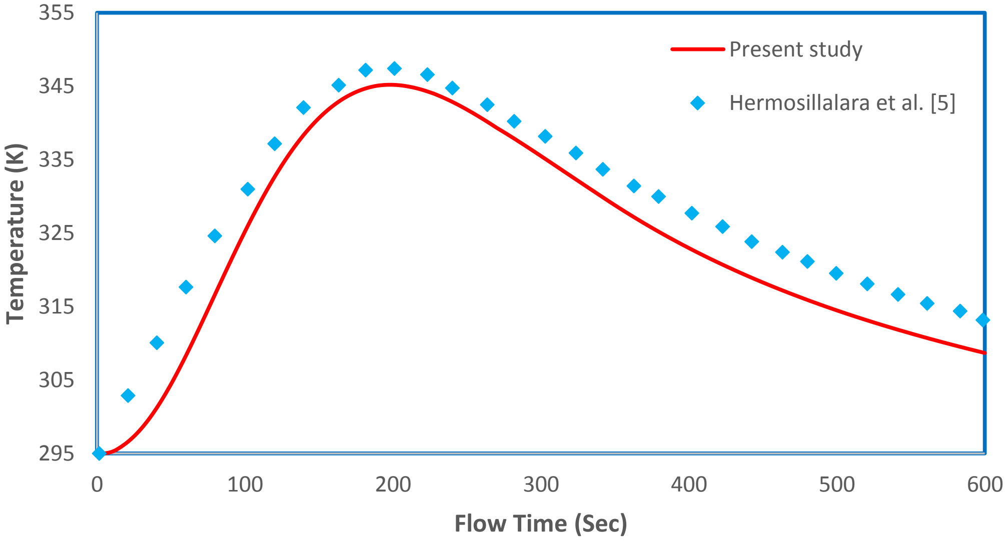

Figure 12: Temperature profile during charging phase at point 03

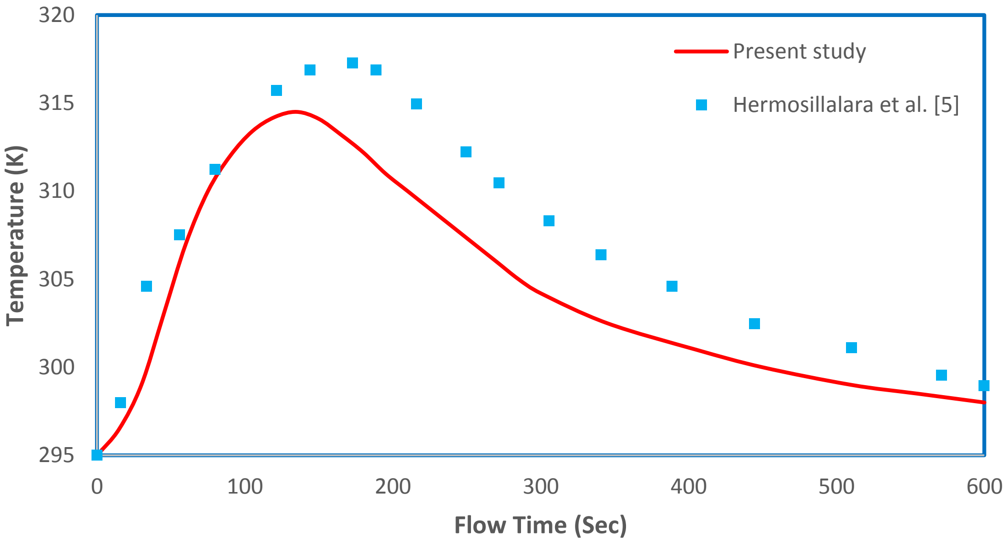

Figure 13: Temperature profile during charging phase at point 04

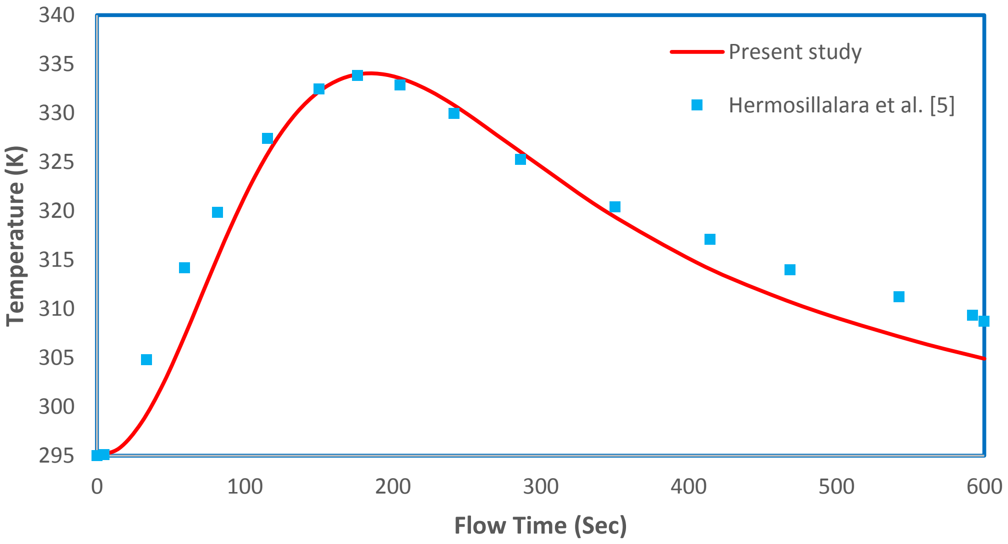

Figure 14: Temperature profile during charging phase at point 05

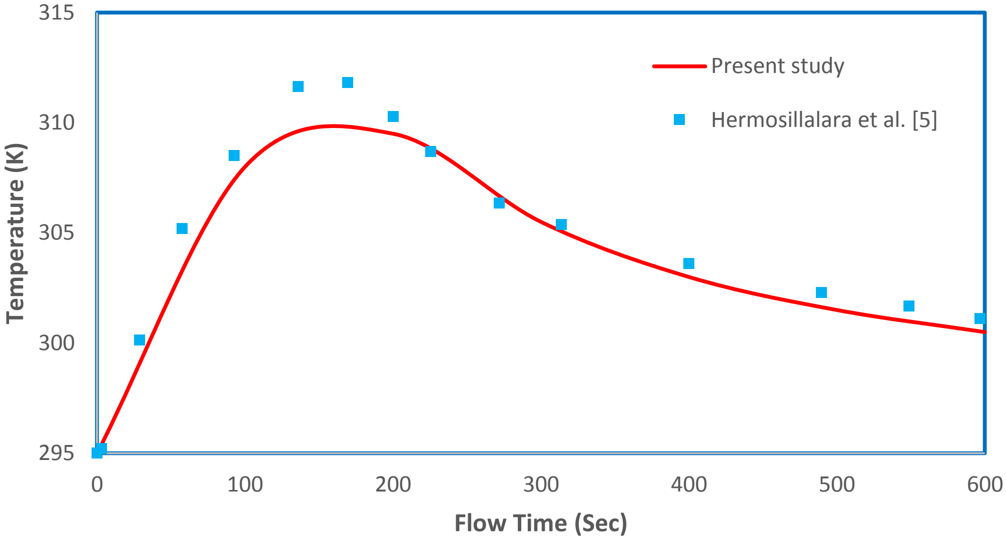

Figure 15: Temperature profile during charging phase at point 06

Xiao et al. [32] studied heat and mass transfer phenomena during charging of hydrogen in a stainless steel storage tank packed with activated carbon. Charging process was simulated at room temperature (295K) and medium storage pressure (10 MPa) using finite volume commercially available software FLUENT. A comparison of absolute adsorption at point 03 between present study and with the absolute adsorption presented by Xiao et al. [32] is shown in Figure 16. Absolute adsorption trend predicted by this study is in good agreement with that presented by Xiao et al [32].

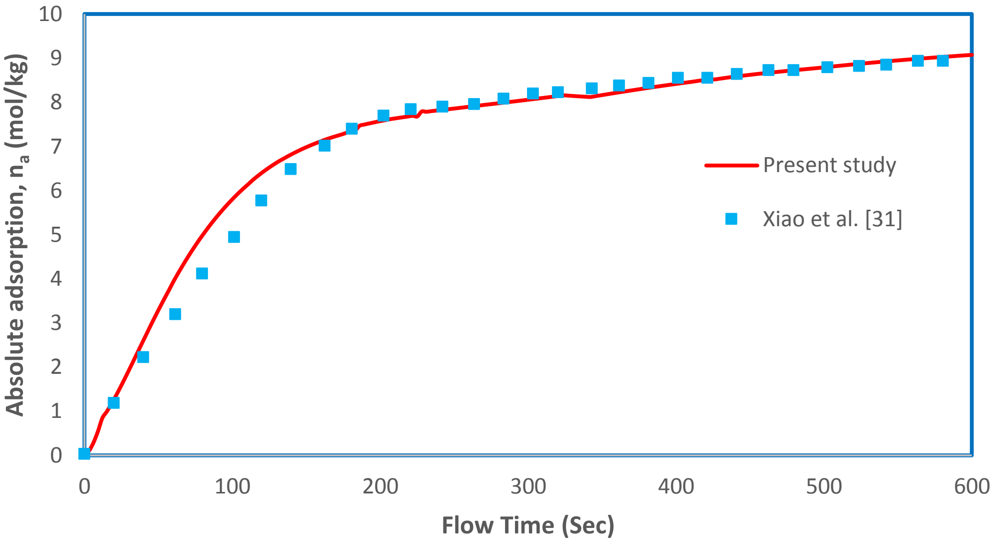

Figure 16: Comparison of absolute adsorption at point 03

4.2 Adsorption of CO_2 in Activated Carbon

To understand the adsorption phenomena, adsorption of CO_2 in a tank filled with activated carbon is studied in detail. CO_2 gas is fed to the tank at 2 bar and 295K gas temperature. Constant mass flux corresponding to 0.00l kg/s mass flow rate is applied at the inlet using UDF for the time 0 to 400sec followed by 200sec for the storage system to stablize. Few more points, Point 07 (31.875,0) and Point 08 (225,0) along axis and Point 09 (127.5,36) along radial direction, have been selected in addition to the previously selected points. These points are shown in the Figure 17.

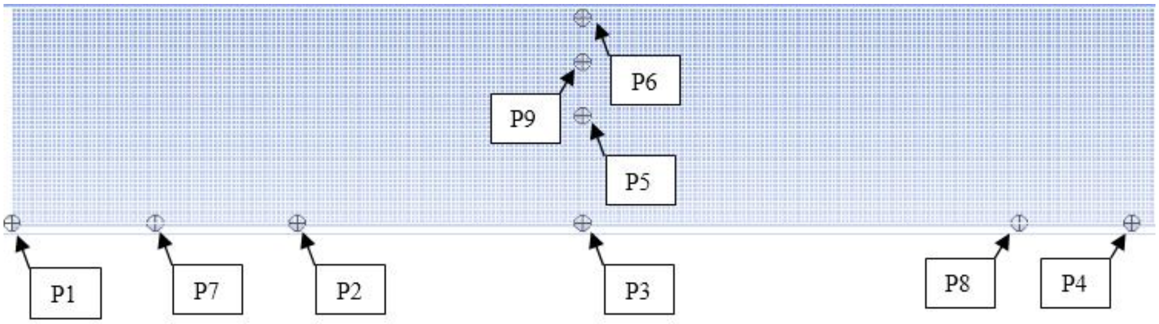

Figure 17: Geometry model of the tank for CO_2 storage

4.2.1 Adsorption analysis

Simulation results for the absolute adsorption along axial direction and along radial direction at x = 127.5 mm are shown in Figures 18 and 19. Figure 20 describes variation of volumetric average value of absolute adsorption with time. The volume-weighted average is calculated by dividing the summation of product of selected field variable and cell volume by the total volume of cell zone and is expressed by the following equation (18);

$$\frac{1}{V}\int \phi dV = \frac{1}{V}\sum_{i=1}^{n}\phi_i \left|V_i\right| \tag{18}$$

It is observed that during initial 100 sec of gas flow inside the storage tank adsorption rate is high and then it decreases gradually until the maximum adsorption is occurred under operating conditions. This is because the absolute adsorption depends upon local pressure and temperature. Since there was no gas inside storage system in the beginning, there is sharp increase in pressure within the system due to large pressure gradient during first 100 seconds as CO_2 gas was fed to the tank. As the pressure rises in the storage tank the adsorption rate starts decreasing. Beyond 400 seconds no further adsorption is observed telling us that maximum amount of the gas is adsorbed under said conditions. In Figure 18 it can be observed that absolute adsorption amount is higher at Point 01 and Point 04 compared to the points 02, 03, 07 and 08 in axial direction along axis. This can be due to the reason that as absolute adsorption is mainly controlled by the local temperature, it is highest at points where local temperature is minimum and vice versa. Since Point 01 lies at the entrance where convective effects of the fresh gas is high and also conductive heat transfer at Point 04 is better due to proximity to the wall. Temperature at points 02, 03, 07 and 08 is higher due to poor thermal conductivity of the adsorption bed so absolute adsorption is lower at these location.

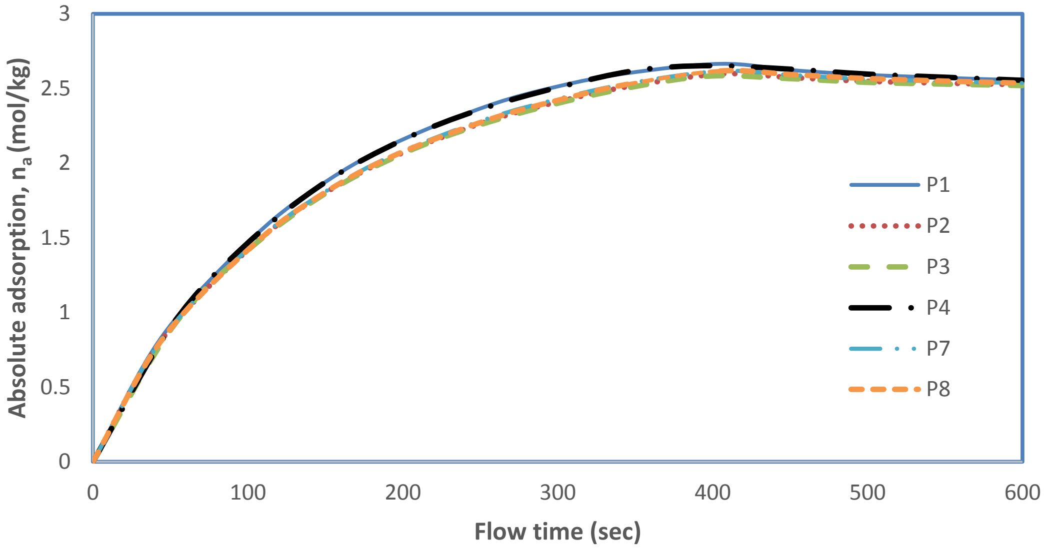

Figure 18: Time variation of absolute adsorption history of CO_2 in activated carbon along points in axial direction

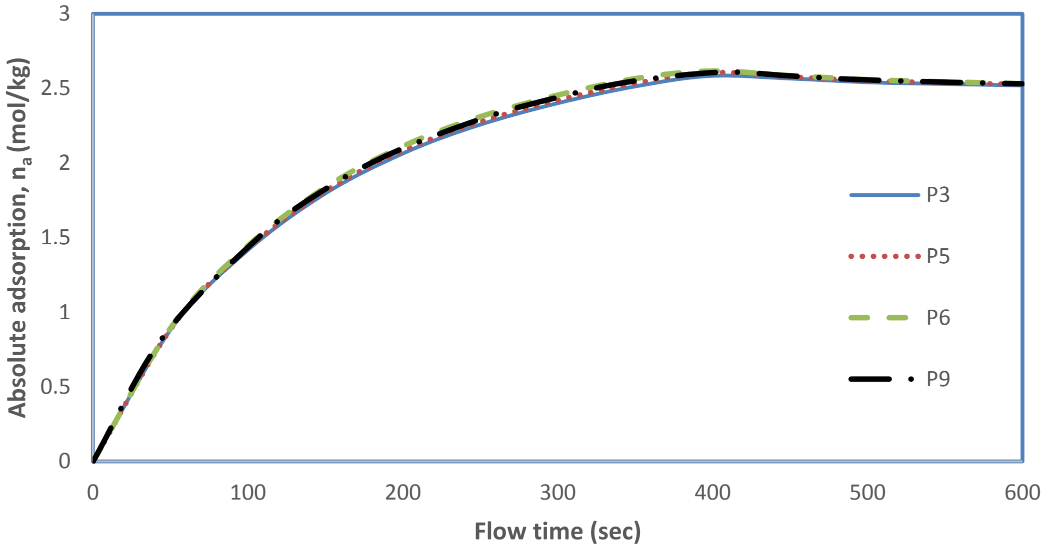

Figure 19: Time variation of absolute adsorption history of CO_2 in activated carbon along points in radial direction

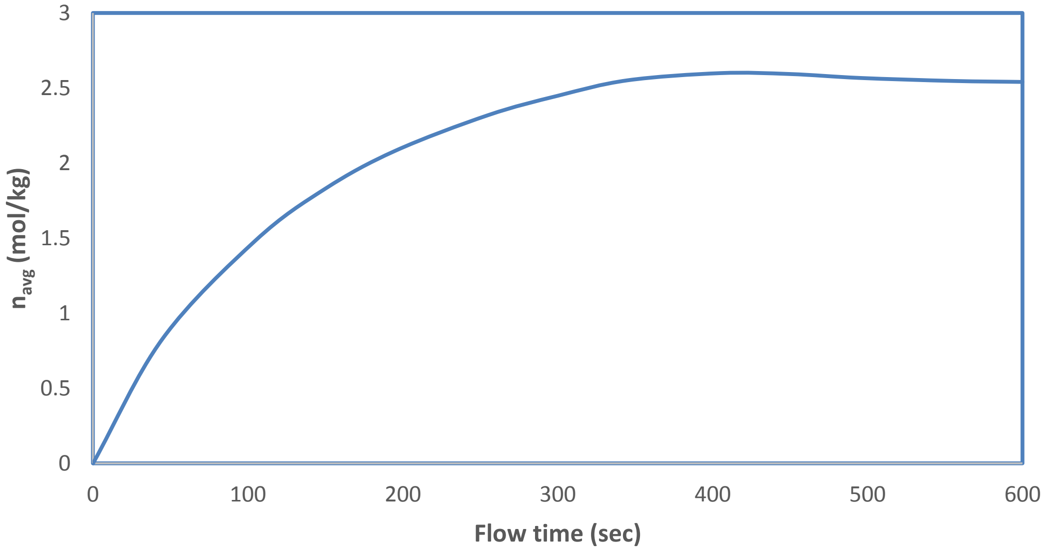

Figure 20: Time variation of volumetric average value of absolute adsorption of CO_2, n_{avg} in activated carbon

Figure 21 shows absolute adsorption distribution of CO_2 in activated carbon along axial direction at axis at different flow times. Large adsorption gradient is observed from 0 to 65 mm and from 225 to 255 mm along the axis of the storage tank. Absolute adsorption is minimum and remains almost same from 75 mm to 215 mm along the axis. This might be because of the poor convective effects of the fresh gas and bad thermal conductivity of the activated carbon bed which results in higher temperature at the central region of the tank subsequently decreasing adsorption amount in the central region compared to entrance and regions near walls. Figure 22 shows absolute adsorption distribution of CO_2 in activated carbon along radial direction at x = 127.5mm at different flow times. It can be seen that delta of absolute adsorption between positions at y = 0 to y = 48mm is 0.011 at flow time equals to 45sec which increases to 0.051 at flow time equals to 210sec and then again decreases to 0.024 at flow time equals to 390 sec. This is because temperature gradient is maximum at flow time equals to 210sec along radial direction at x = 127.5mm followed by temperature gradient at flow time equals to 390sec. Temperature gradient is minimum at flow time equals to 45 sec which results in minimum variation of absolute adsorption along radial direction. Figure 23 shows contours of absolute adsorption at different flow times. It is observed that highest amount of absolute adsorption is found at the entrance and near wall regions. Whereas lowest amount of the absolute adsorption is found to be in the central region of the storage tank. Since absolute adsorption depends upon local pressure and temperature. The pressure distribution is almost uniform throughout the tank whereas temperature distribution varies inside the tank. Absolute adsorption is mainly controlled by the local temperature, it is highest at points where local temperature is minimum and vice versa. So highest amount of absolute adsorption is observed at entrance and near wall regions because convective effects of the fresh gas is strong at the entrance and also conductive heat transfer of the points near wall region is better. However minimum amount of the absolute adsorption is observed in the central region of the tank because of the larger temperature.

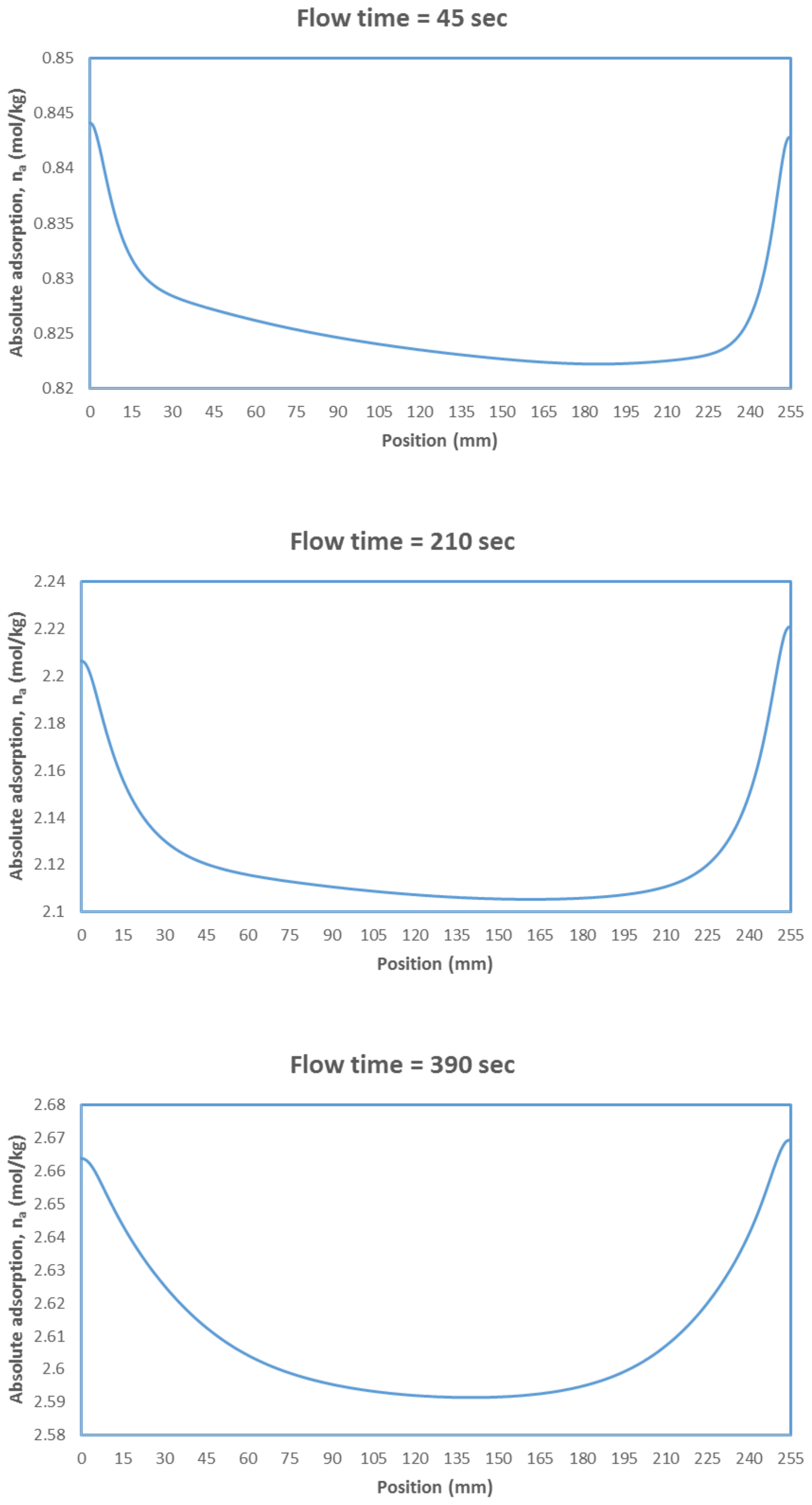

Figure 21: Axial distribution of absolute adsorption at different flow times

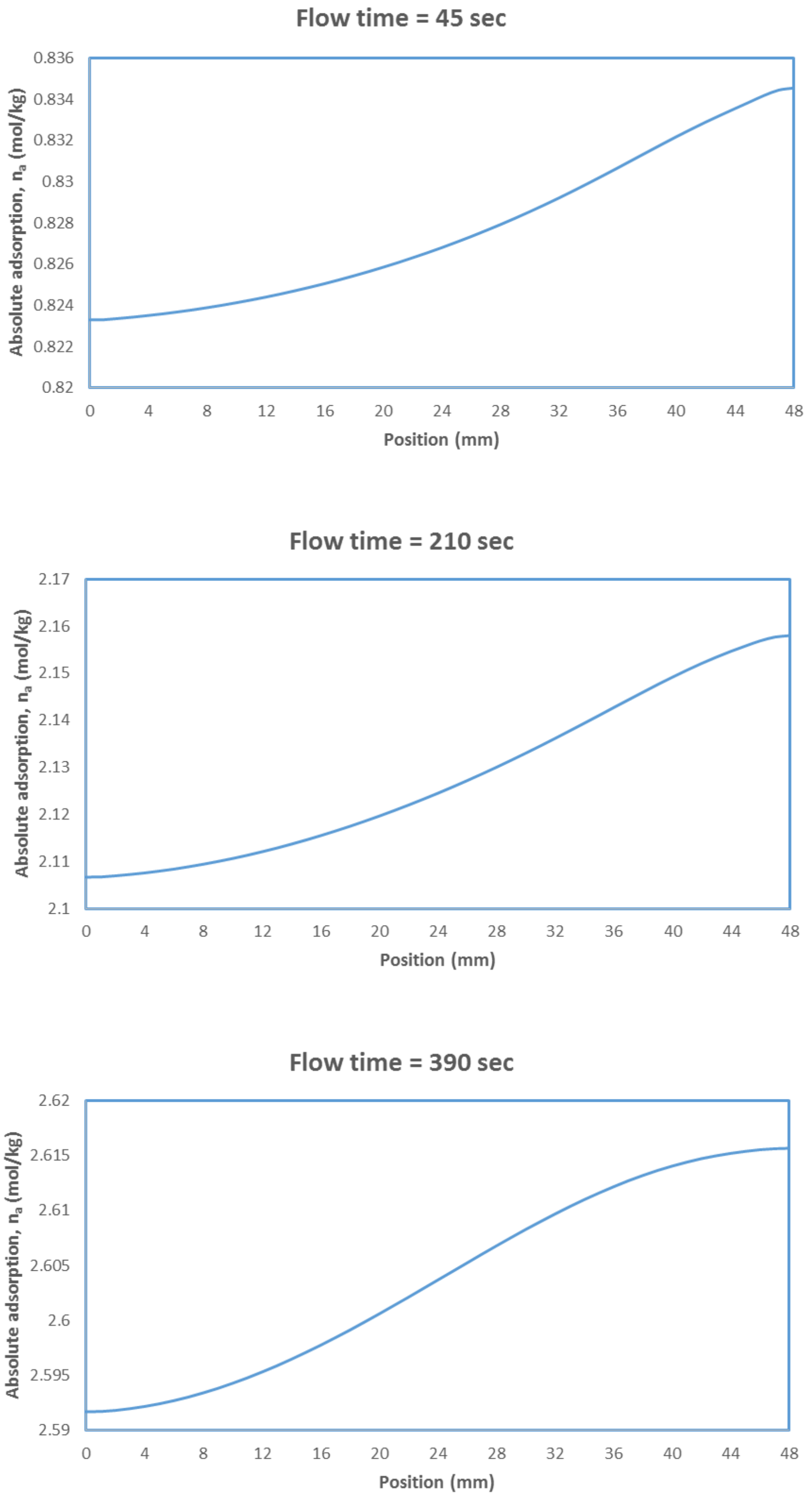

Figure 22: Radial distribution of absolute adsorption at different flow times

Flow time = 45 sec

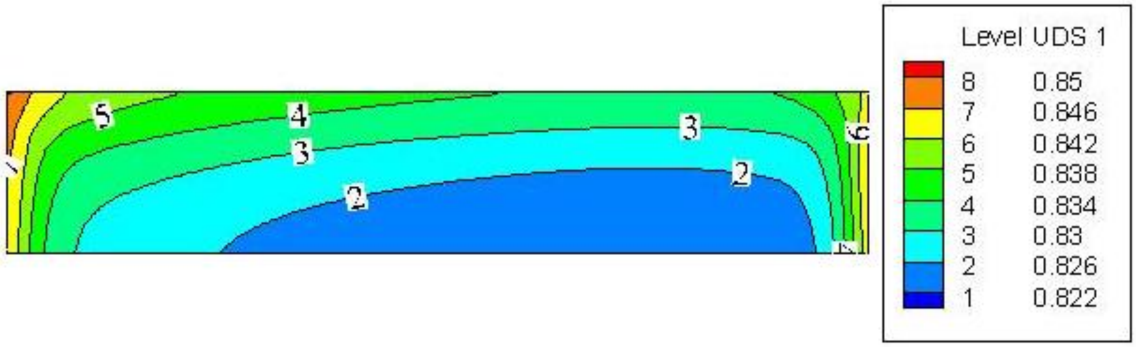

Flow time = 210 sec

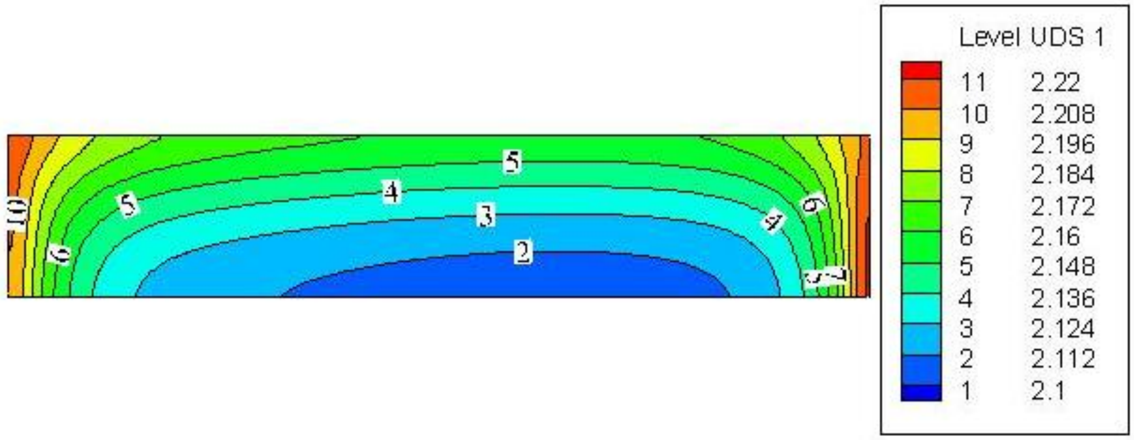

Figure 23: Contours of absolute adsorption (mol/kg) at different flow times

4.2.2 Temperature analysis

Figures 24 and 25 provide comparison of the temperature distribution of CO_2 adsorption in activated carbon along axial direction and radial direction at different locations. Temperature rises sharply during first 200 seconds because of adsorption and compression both being exothermic in nature. Temperature at point 01 remains constant (295K) due to inlet boundary condition. Temperature reaches the maximum value in central region of the tank and is lower in the region in areas closer to wall and at entrance. Maximum temperature is found to be at point 03, which is 486K. This might be due to the fact that convective effects of fresh gas entering the tank is weaken at this location. Moreover heat transfer from the central region of the tank to the walls is low due to bad heat conduction of the activated carbon bed.

Points 04 and 06 are both located near walls of the storage tank. However temperature at point 06 (near top wall) is lower compared to the temperature at point 04 (near bottom wall). Possible explanation might be the stronger convective effects along the axial direction compared to the radial direction, subsequently resulting more heat being transfer from central region, at higher temperature, to the bottom of the tank compared to the top wall. Temperature at points 05 and 09 is lower compared to the temperature at point 03 because of their proximity to the top wall. Temperature at point 07 lower than point 03 because of the cooling effect of the fresh CO_2 passing through this location.

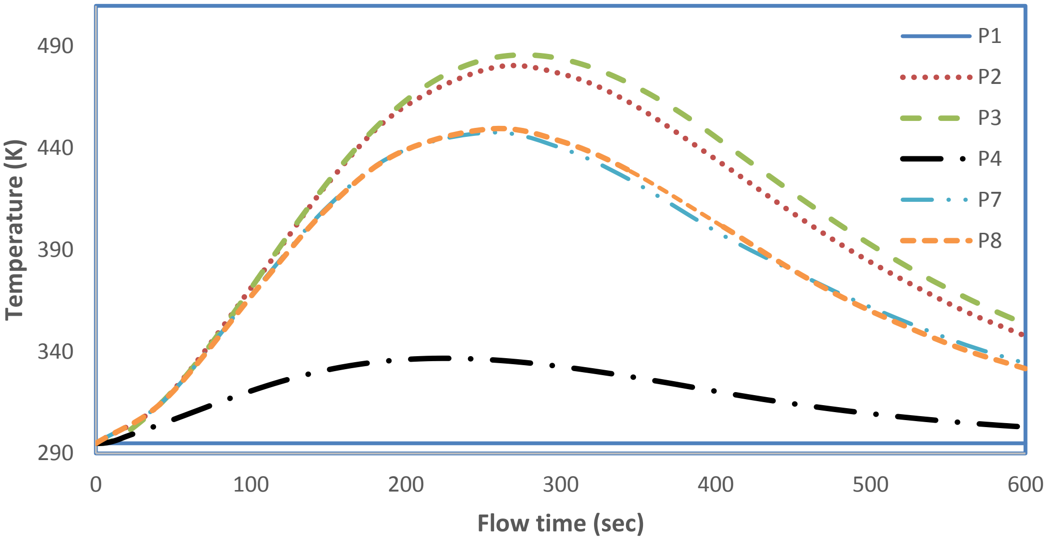

Figure 24: Temperature histories along axial direction at different points

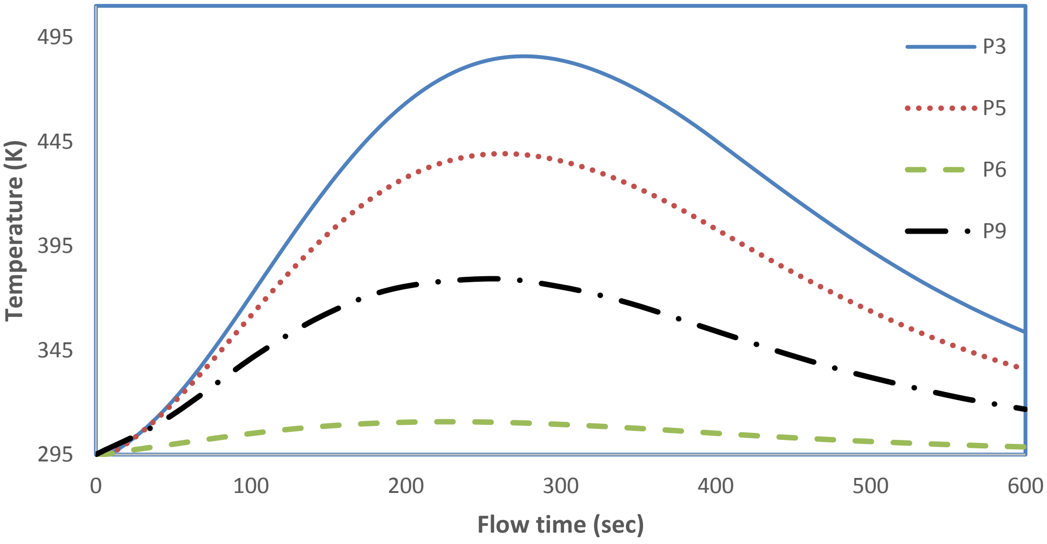

Figure 25: Temperature histories along radial direction at different points

Figure 26 shows temperature distribution along the axial direction at different flow times. Large temperature gradient is observed from 0 to 50 mm and from 215 to 255 mm along the axis of the storage tank. Temperature remains almost same from 70 mm to 195 mm along the axis. This might be because of the poor convective effects of the fresh gas and bad thermal conductivity of the activated carbon bed.

Figure 27 shows temperature distribution along the radial direction at x = 127.5 mm at different flow times. It can be observed that temperature decreases gradually, from maximum at point 03 (y = 0) in the central region to the minimum at wall (y = 48). Temperature in the central region of the tank at 600 seconds is much lower compared to 210 seconds and 390 seconds due to large amount of energy transfer from the central region to the surrounding walls.

Figure 28 shows contours of temperature distribution at different flow times. Temperature reaches maximum value in the central region of the tank and is lower at entrance and in areas close to walls. This is because convective effects of fresh gas gets weak in the central region. Moreover poor thermal conductivity of the adsorption bed also contributes in keeping higher temperature in the center of the tank. After main charging phase temperature distribution tends to become uniform.

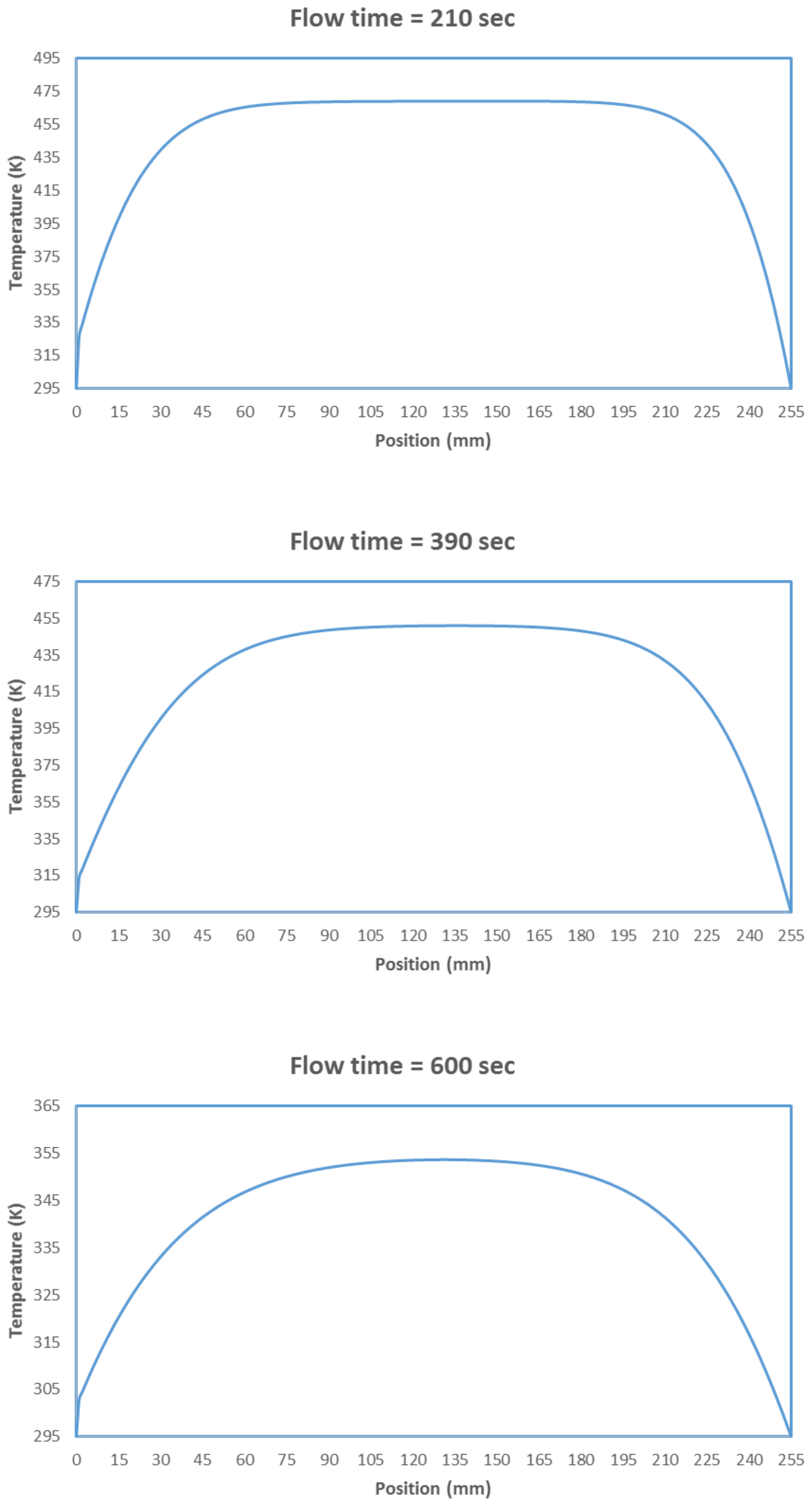

Figure 26: Temperature histories in axial direction at different flow times

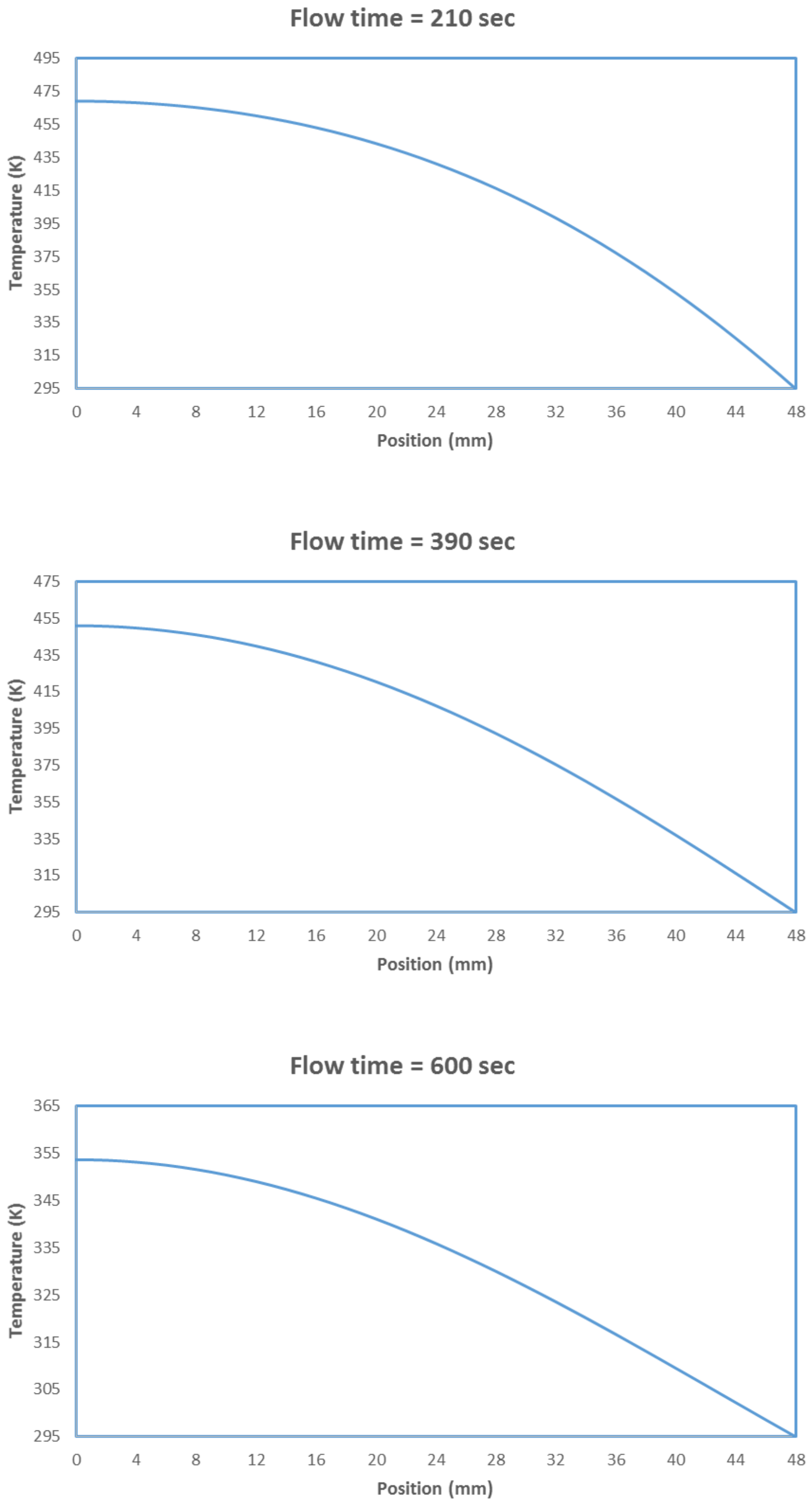

Figure 27: Temperature histories in radial direction at different flow times

Flow time = 210 sec

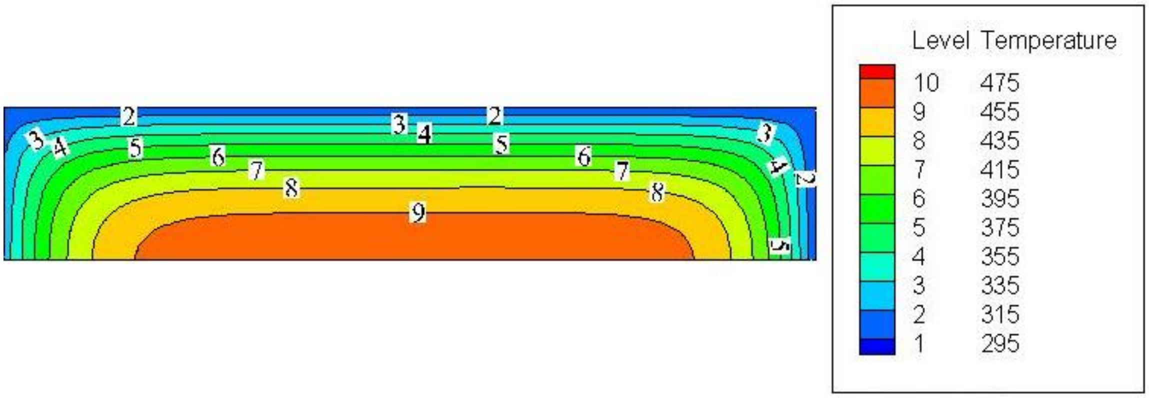

Flow time = 390 sec

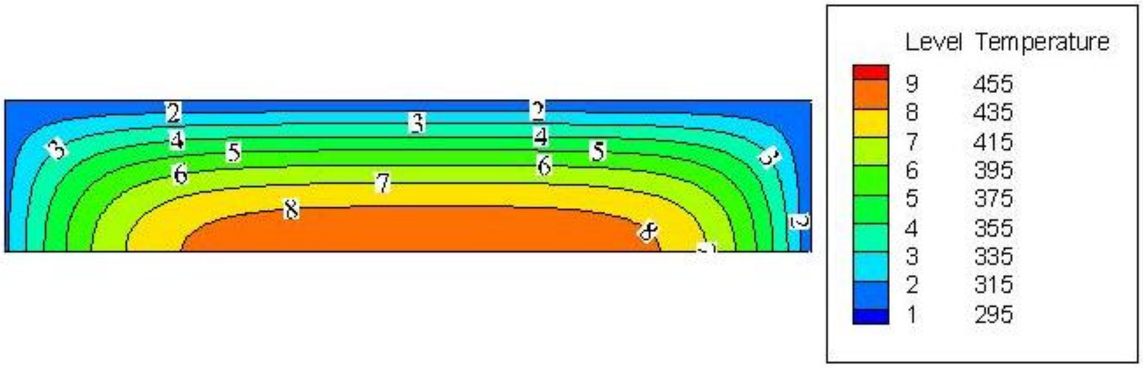

Flow time = 600 sec

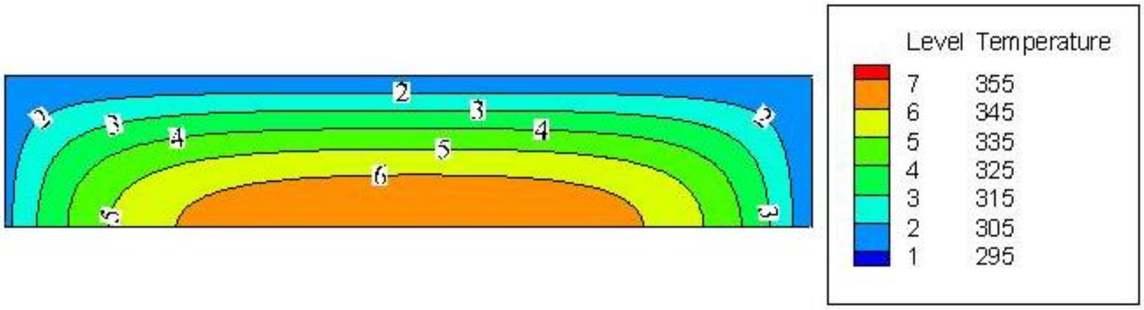

Figure 28: Temperature (K) contours at different flow times

4.2.3 Velocity distribution

Figure 29 – 31 shows contours of velocity magnitude in axial direction at different flow times. CO_2 gas enters the domain at constant mass flux of 1e-3 kg/s. As the time passes, the CO_2 continues to enter in the cylinder, the velocity at the inlet at 45 seconds is 2.44e-4 m/s i.e. maximum in the domain and it decreases as the flow moves towards the end. This is due to the fact that mass of CO_2 is adsorbed in the adsorbent which causes the mass flow rate to decrease hence decreasing the velocity. All CO_2 is adsorbed till the end which is shown by zero velocity region. Similar trend is observed in the contours at 210 seconds and 390 seconds.

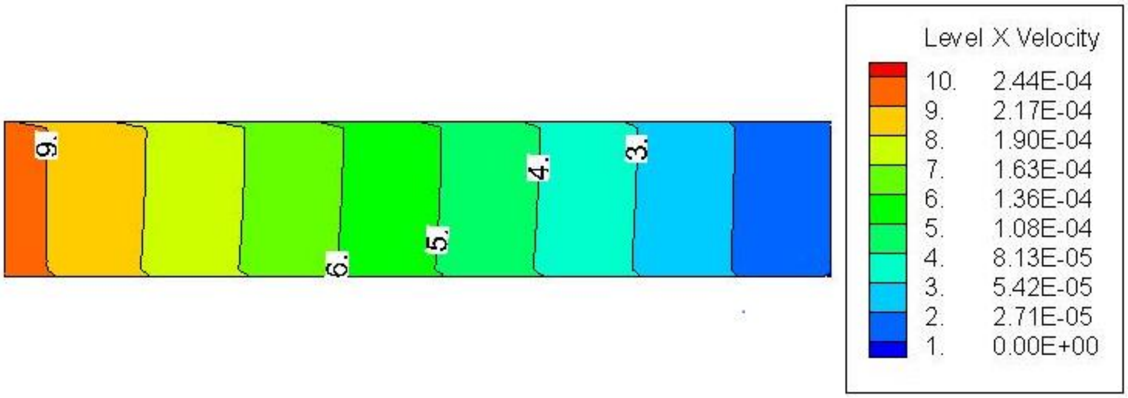

Figure 29: Contours of axial velocity (ms^{-1}) at 45 seconds

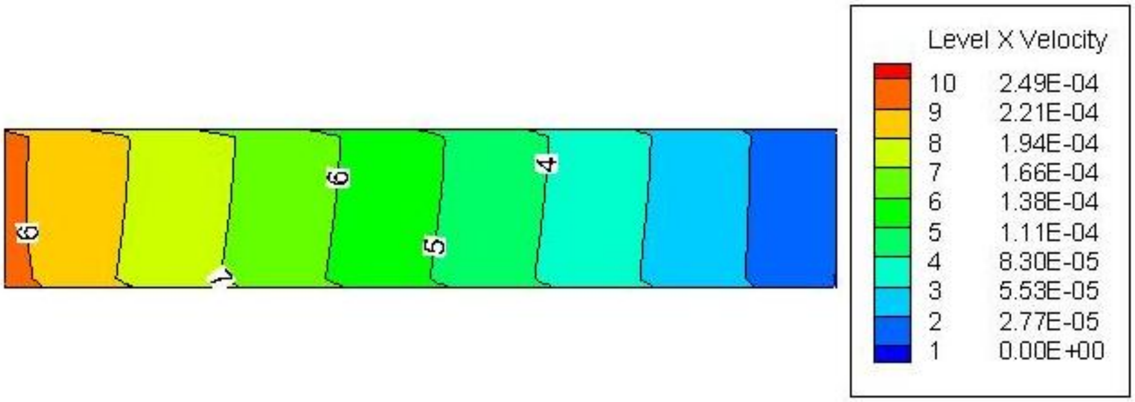

Figure 30: Contours of axial velocity (ms^{-1}) at 210 seconds

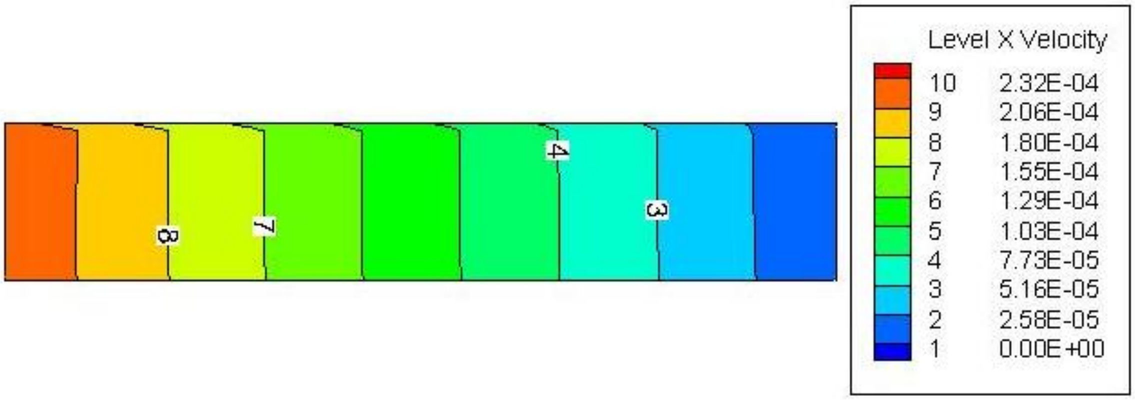

Figure 31: Contours of axial velocity (ms^{-1}) at 390 seconds

4.3 Effect of Storage Pressure on Adsorption

To investigate the effect of variation of storage pressure on adsorption of CO_2 in Mg-MOF-74, Zeolite and Activated carbon five cases have been considered in which storage pressure is increased from 20 kPa to 100 kPa with an interval 20 kPa respectively, with constant mass flux corresponding to 0.001 kg/sec mass flow rate being applied at inlet using UDF for the time 0 to 400 sec followed by 200 sec for the system to get stabilize. Temperature of storage tank walls is kept constant at 295 K and CO_2 gas is fed at 295 K.

4.3.1 Effect of storage pressure on adsorption of CO_2 in Mg-MOF-74

Effect of variation of storage pressure on the adsorption of CO_2 in Mg-MOF-74 at points 03, 04 and 05 is shown in Figures 32 – 34 respectively. It can be observed that for all the cases, during initial 100 sec adsorption rate is high and then it decreases gradually until the maximum adsorption is occurred. This is because the absolute adsorption depends upon local pressure and temperature. Since at the beginning there was no gas inside tank, as gas is fed to the tank there is sharp increase in pressure within the system due to large pressure gradient during first 100 seconds. Sharp rise in pressure within the storage system subsequently increases adsorption as shown. As the pressure is building in tank, absolute adsorption rate decreases because pressure gradient is decreasing until zero when pressure inside the tank is in equilibrium with the storage pressure.

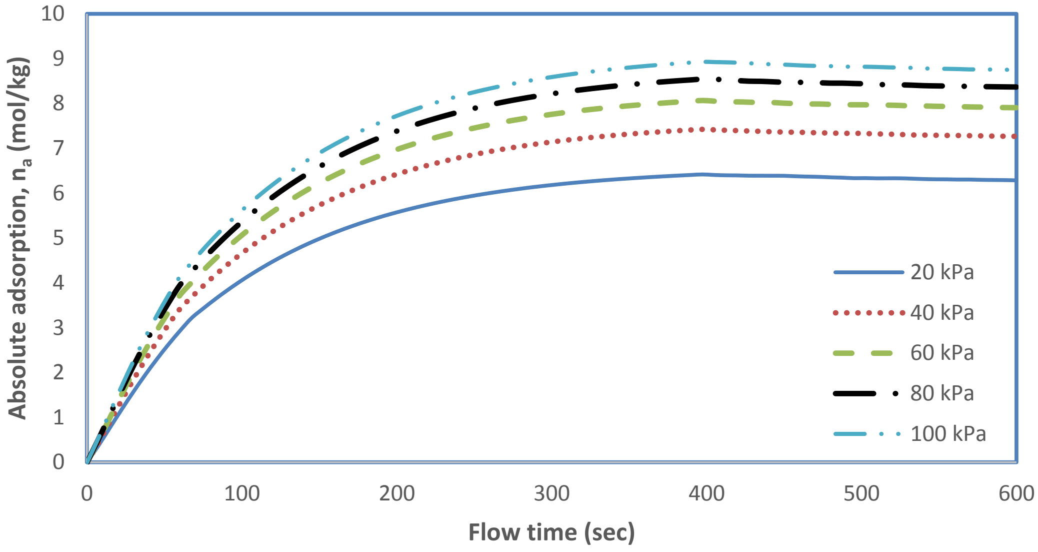

Figure 32: Time variation of absolute adsorption history of CO_2 in Mg-MOF-74 at Point 03 for varying storage pressure

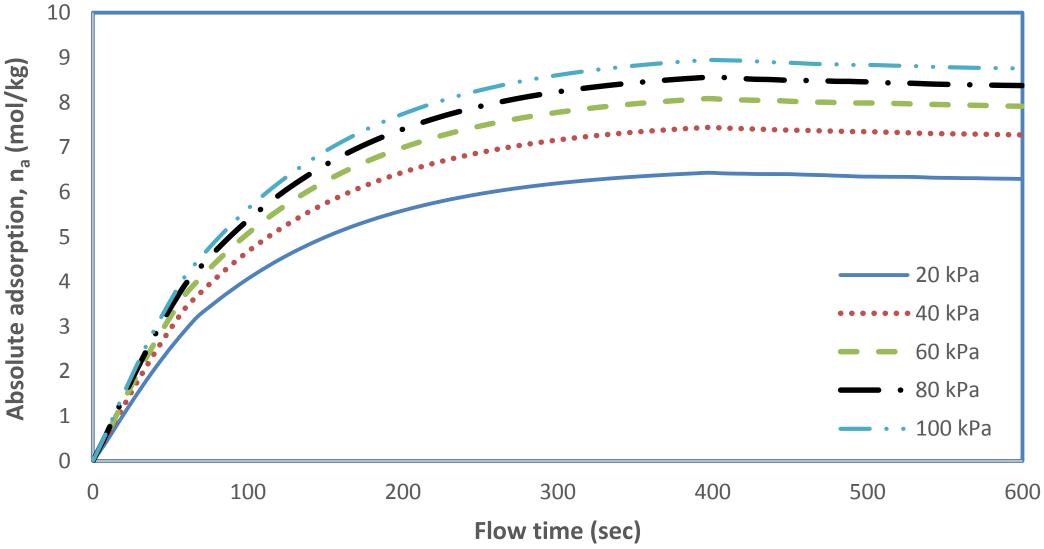

Figure 33: Time variation of absolute adsorption history of CO_2 in Mg-MOF-74 at Point 04 for varying storage pressure

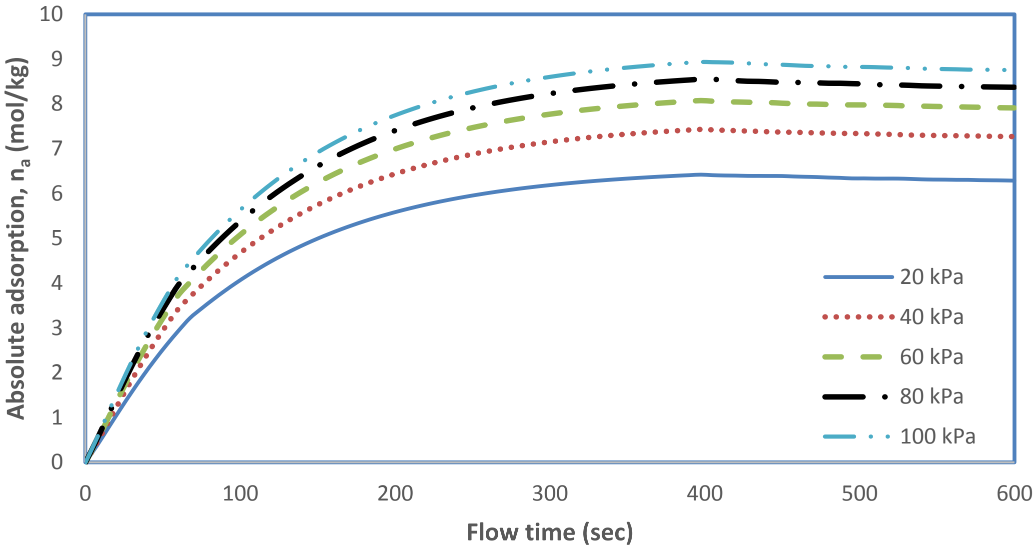

Figure 34: Time variation of absolute adsorption history of CO_2 in Mg-MOF-74 at Point 05 for varying storage pressure

Figure 35 shows the time variation of volumetric average value of absolute adsorption of CO_2 in Mg-MOF-74 for varying storage pressure cases. Volumetric average absolute adsorption is calculated as shown in Equation 19. It can be seen that adsorption of CO_2 increases with increase in storage pressure. This is due to the fact that with increase in storage pressure, differential molar work of adsorption decreases as shown in Equation 11. As differential molar work of adsorption decreases, degree of filling of micropores increases as expressed by Equation 10, subsequently increasing the absolute adsorption amount of CO_2 gas in the storage tank. In case 1 when storage pressure is set to 20 kPa, the amount of absolute adsorption is about 6.29 mol/kg. For case 2, having storage pressure equal to 40 kPa the amount of absolute adsorption is about 7.27 mol/kg. For case 3 where storage pressure is equal to 60 kPa, the amount of absolute adsorption achieved is 7.90 mol/kg. 8.37 mol/kg of absolute adsorption is achieved in case 4 when storage pressure is set to 80 kPa. Maximum amount of absolute adsorption is achieved in case 5 when storage pressure is set to 100 kPa and is equal to 8.75 mol/kg. So it can be seen that with increase in storage pressure from 20 kPa to 100 kPa, we can have extra 2.46 mol/kg absolute adsorption of CO_2 in Mg-MOF-74.

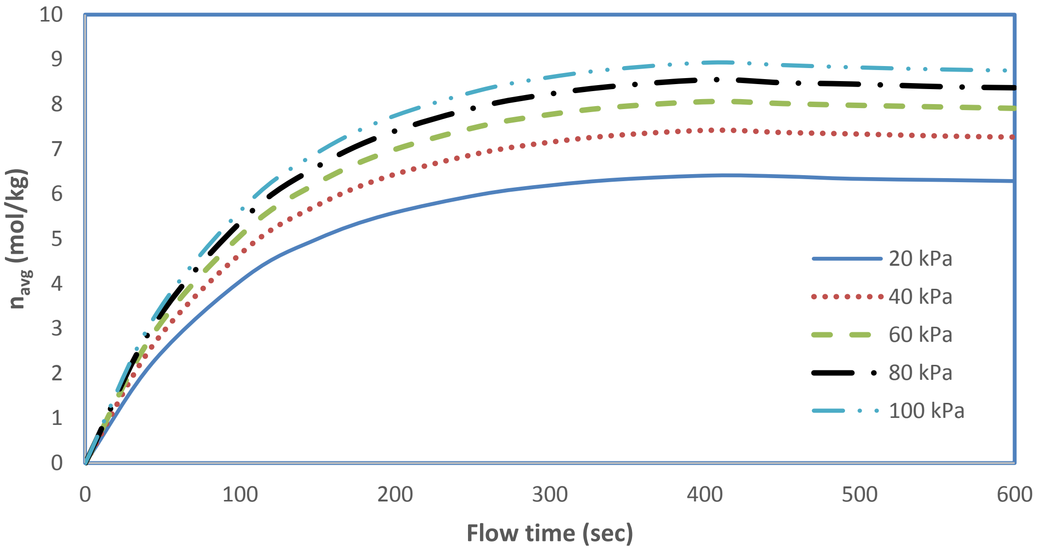

Figure 35: Time variation of volumetric average value of absolute adsorption of CO_2, n_{avg} in Mg-MOF-74 for varying storage pressure

Figures 36 – 38 provide temperature histories of adsorption of CO_2 in Mg-MOF-74 at point 03, 04 and 05 respectively with varying storage pressure. Sharp rise of temperature is observed during first 200 seconds. This is due to the reason that both adsorption and compression are exothermic in nature. Initially as pressure gradient is higher adsorption rate is high subsequently releasing more energy thus increasing temperature of adsorption bed. Temperature reaches the maximum value in central region of the tank and is lower in the region in areas closer to wall and at entrance. In all cases maximum temperature is found at point 03 in the central region of the tank. This might be due to the fact that convective effects of fresh gas entering the tank is weaken at this location. Moreover heat transfer from the central region of the tank to the walls is low due to bad heat conduction of the Mg-MOF-74. For all cases, peak value of temperature at point 04 occurs at about 200 seconds, which is earlier than the peaks of temperature at point 03 and 05. This is because of proximity of point 04 to the wall which is at 295 K. At point 04 heat dissipation due to conduction is strong which restricts the peak value. However at points 03 and 05 temperature keeps on rising till 250 seconds due to poor heat dissipation of the adsorption bed owing to is low thermal conductivity.

In Figure 36, it can be seen that temperature at point 03 increases with increase in storage pressure. This is due to the reason that absolute adsorption increases with increase in storage pressure consequently increasing the temperature at point 03 in the center of storage tank. Peak value of temperature at point 03 for case 5, when storage pressure is 100 kPa, is 704 K which is about 148 K higher compared to the peak temperature at same location for case 1 having storage pressure set to 20 kPa. Peak value of temperature at point 03 for case 1 is about 555 K.

Figure 37 shows temperature histories of adsorption of CO_2 in Mg-MOF-74 at point 04 with varying storage pressure. Peak value of temperature for case 1 is about 353 K however for case 5 the peak value is 384 K. This is because increase in pressure enhances adsorption resulting in more heat being released because of its exothermic nature. However temperature at point 04 is lower compared to temperatures at point 03 and 05 because of its proximity to the wall. Heat transfer due to conduction is much better at this point which results in lower peak temperature.

Figure 38 shows temperature histories of adsorption of CO_2 in Mg-MOF-74 at point 05 with varying storage pressure. A similar trend of increase in peak temperature values with increase in pressure is also observed at point 04. Temperature at point 05 is lower than the temperature at point 03 however it is large compared to the temperature at point 04. This is because of its proximity to the isothermal wall compared to point 03 however its distance from top wall is large compared to that of point 05.

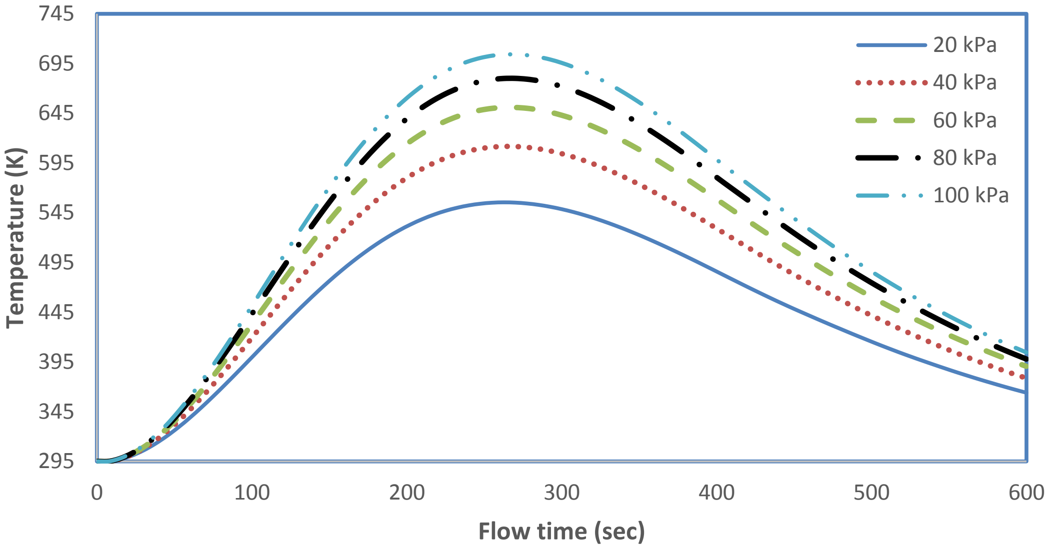

Figure 36: Temperature histories of adsorption of CO_2 in Mg-MOF-74 at point 03 for varying storage pressure

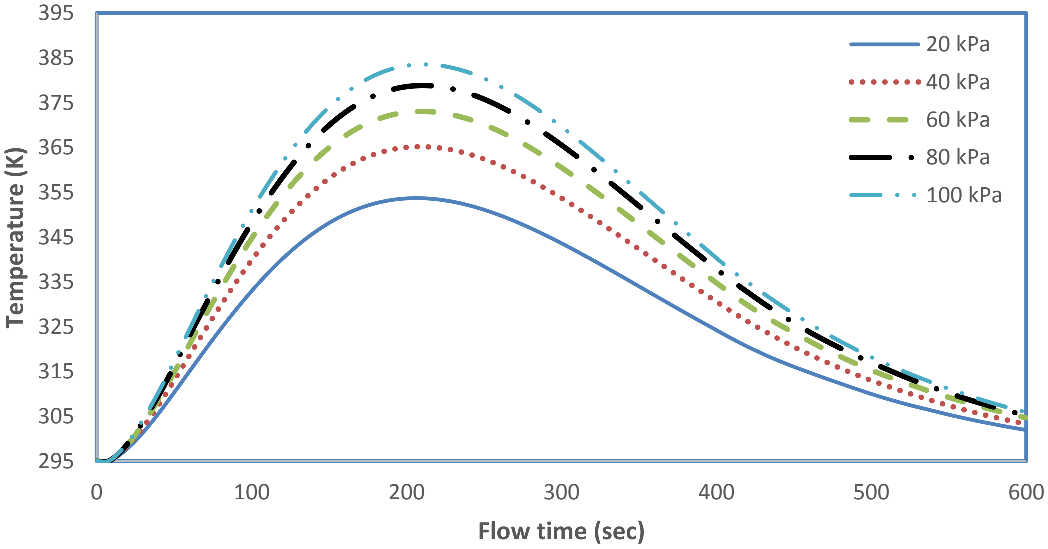

Figure 37: Temperature histories of adsorption of CO_2 in Mg-MOF-74 at point 04 for varying storage pressure

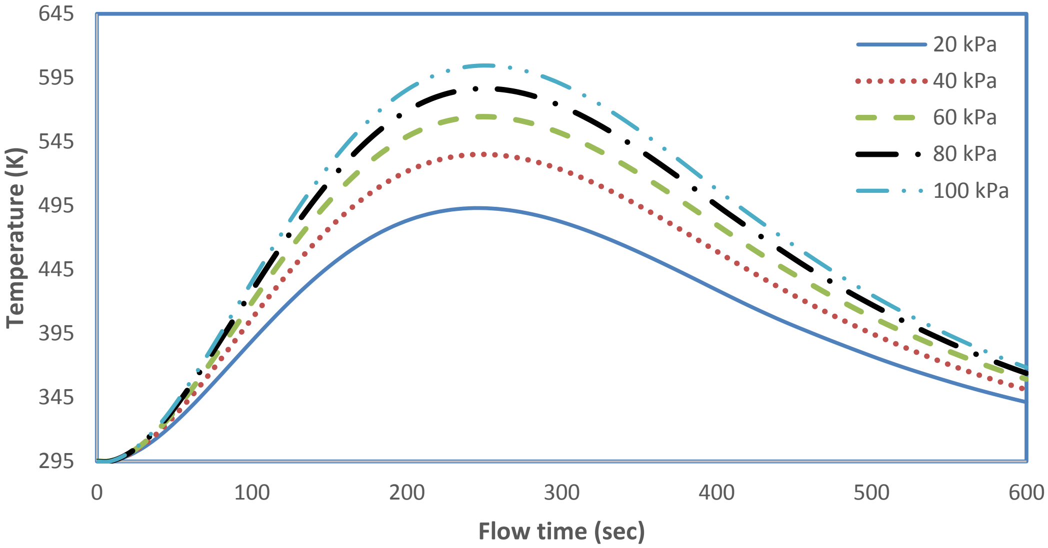

Figure 38: Temperature histories of adsorption of CO_2 in Mg-MOF-74 at point 05 for varying storage pressure

4.3.2 Effect of storage pressure on adsorption of CO_2 in Zeoltie

Effect of variation of storage pressure on the adsorption of CO_2 in Zeolite at points 03, 04 and 05 is shown in Figures 39 – 41 respectively. For each case, during initial 100 sec adsorption rate is high and then it decreases gradually until the maximum adsorption is occurred. This is because the absolute adsorption depends upon local pressure and temperature. Initially tank was empty, as gas is fed to the tank there is sharp increase in pressure within the system due to large pressure gradient during first 100 seconds results in higher adsorption rate. With the passage of time absolute adsorption rate decreases because pressure gradient is decreasing until zero when pressure inside the tank is in equilibrium with the storage pressure.

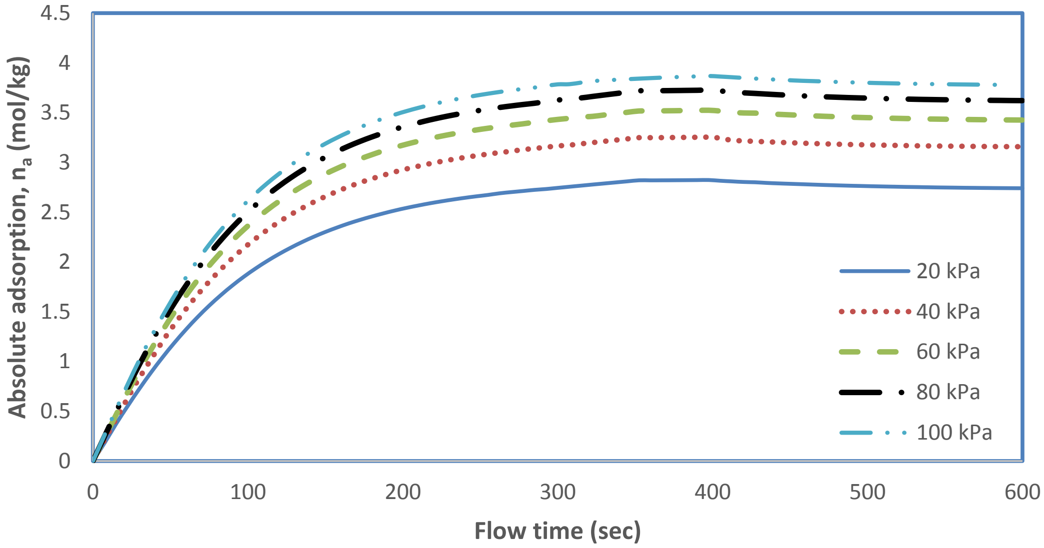

Figure 39: Time variation of absolute adsorption history of CO_2 in Zeolite at Point 03 for varying storage pressure

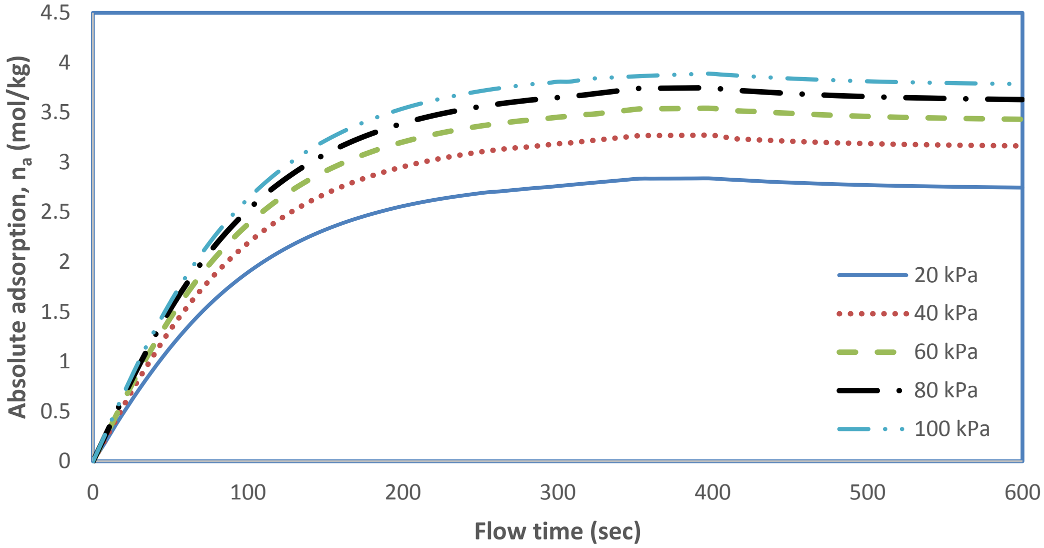

Figure 40: Time variation of absolute adsorption history of CO_2 in Zeolite at Point 04 for varying storage pressure

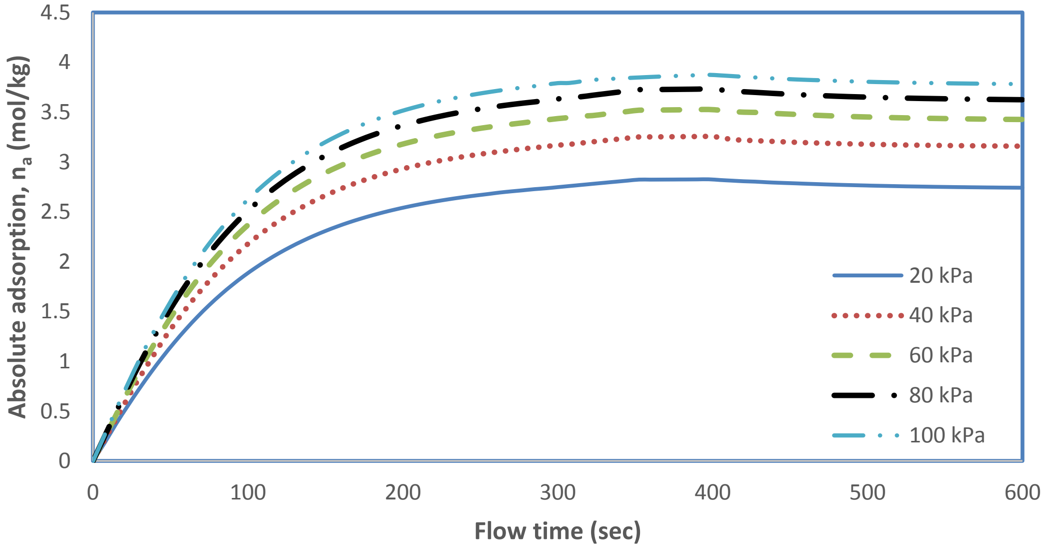

Figure 41: Time variation of absolute adsorption history of CO_2 in Zeolite at Point 05 for varying storage pressure

Figure 42 shows the time variation of volumetric average value of absolute adsorption of CO_2 in Zeolite for varying storage pressure cases. It can be seen that adsorption of CO_2 increases with increase in storage pressure. This is due to the fact that with increase in storage pressure, differential molar work of adsorption decreases which results in increase of degree of filling of micropores consequently increasing absolute adsorption amount of CO_2 gas in the storage tank. In case 1 when storage pressure is set to 20 kPa, the amount of absolute adsorption is about 2.74 mol/kg. Absolute adsorption amount at the end of charging phase is 3.16 mol/kg for case 2, 3.43 mol/kg for case 3, 3.63 mol/kg for case 4 and 3.78 mol/kg for case 5. This shows that with increase in storage pressure from 20 kPa to 100 kPa, we can have extra 1.04 mol/kg absolute adsorption of CO_2 in Zeolite.

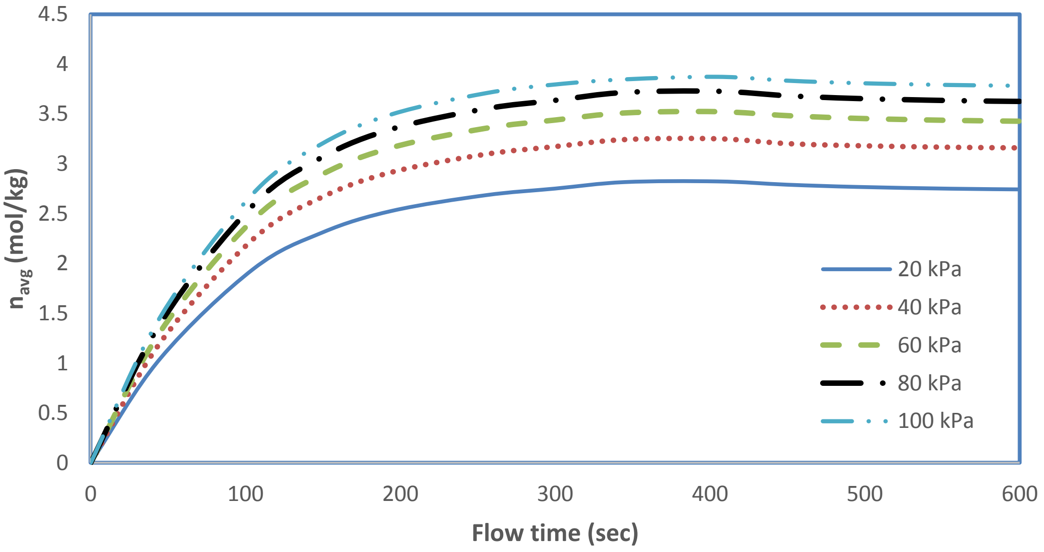

Figure 42: Time variation of volumetric average value of absolute adsorption of CO_2, n_{avg} in Zeolite for varying storage pressure

Figures 43 – 45 provide temperature histories of adsorption of CO_2 in Zeolite at point 03, 04 and 05 respectively with varying storage pressure. Sharp rise of temperature is observed during first 100 seconds because of higher adsorption rate due to large pressure gradient. Which results in releasing more energy thus increasing temperature of adsorption bed. Temperature reaches the maximum value in central region of the tank and is lower in the region in areas closer to wall and at entrance. In all cases maximum temperature is found at point 03 in the central region of the tank due to poor heat transfer of adsorption bed due to low thermal conductivity and also convective effects of fresh gas entering the tank is weaken at this location. For all cases, peak value of temperature at point 04 occurs at about 160 seconds, which is earlier than the peaks of temperature at point 03 and 05. At point 04 heat dissipation due to conduction is strong which restricts the peak value. However at points 03 and 05 temperature keeps on rising till 215 seconds due to poor heat dissipation of the adsorption bed owing to is low thermal conductivity.

In Figure 43, it can be seen that temperature at point 03 increases with increase in storage pressure. This is because absolute adsorption increases with increase in storage pressure consequently increasing the temperature at point 03 in the center of storage tank. Peak value of temperature at point 03 is 419 K for case 1, 441 K for case 2, 454 K for case 3, 465 K for case 4 and 473 K for case 5 respectively.

Figure 44 shows temperature histories of adsorption of CO_2 in Zeolite at point 04 with varying storage pressure. Peak value of temperature is 326 K for case 1, 331 K for case 2, 335 K for case 3, 337 K for case 4 and 338.7 K for case 5 respectively. This is because increase in pressure enhances adsorption resulting in more heat being released because of its exothermic nature. However temperature at point 04 is lower compared to temperatures at point 03 and 05 because of its proximity to the wall. Heat transfer due to conduction is much better at this point which results in lower peak temperature.

Figure 45 shows temperature histories of adsorption of CO_2 in Zeolite at point 05 with varying storage pressure. A similar trend of increase in peak temperature values with increase in pressure is also observed at point 05. Temperature at point 05 is lower than the temperature at point 03 however it is large compared to the temperature at point 04. This is because of its proximity to the isothermal wall compared to point 03 however its distance from top wall is large compared to that of point 05.

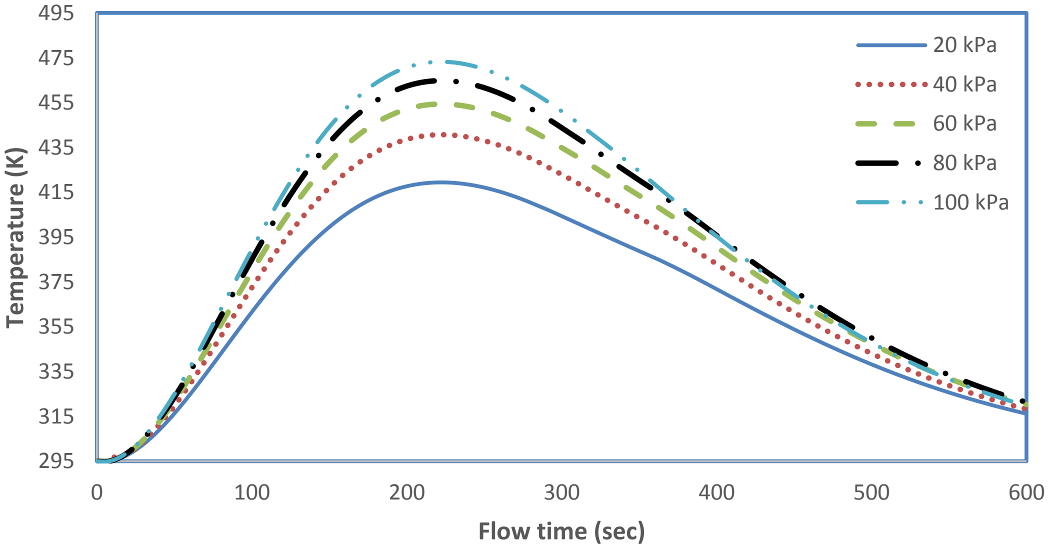

Figure 43: Temperature histories at point 03 for adsorption of CO_2 in Zeolite for varying storage pressure

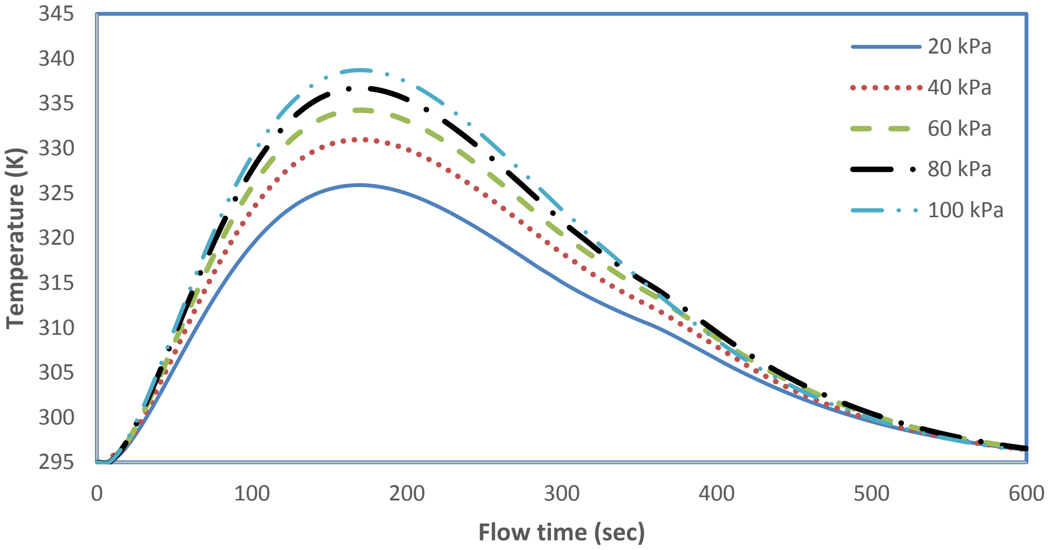

Figure 44: Temperature histories at point 04 for adsorption of CO_2 in Zeolite for varying storage pressure

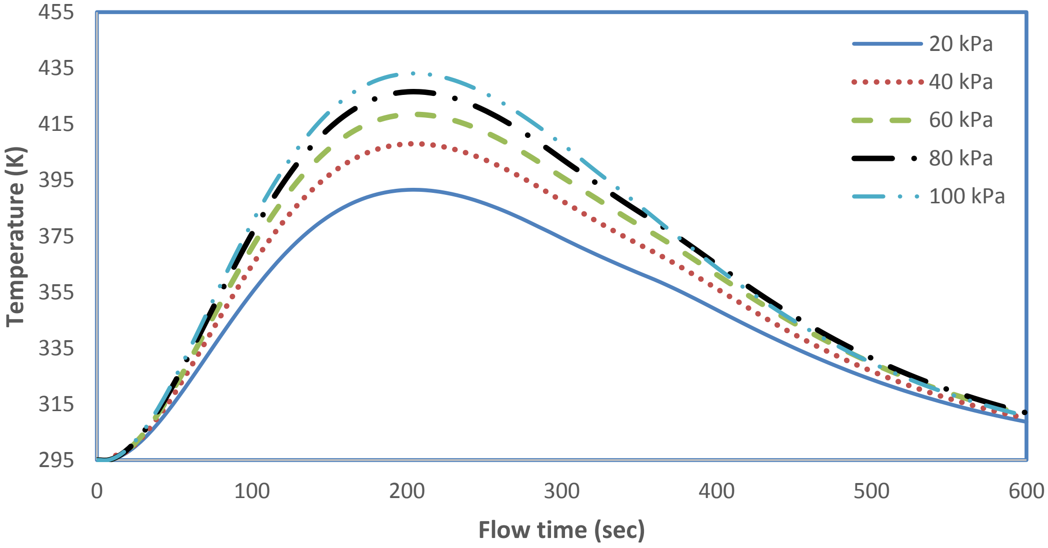

Figure 45: Temperature histories at point 05 for adsorption of CO_2 in Zeolite for varying storage pressure

4.3.3 Effect of storage pressure on adsorption of CO_2 in Activated carbon

Effect of variation of storage pressure on the adsorption of CO_2 in activated carbon at points 03, 04 and 05 is shown in Figures 46 – 48 respectively. For each case, during initial 100 sec adsorption rate is high and then it decreases gradually until the maximum adsorption is occurred. Initially there was no gas in the tank, there is sharp increase in pressure within the system, as gas is fed to the tank, due to large pressure gradient during first 100 seconds results in higher adsorption rate. With the passage of time absolute adsorption rate decreases because pressure gradient is decreasing until zero when pressure inside the tank is in equilibrium with the storage pressure.

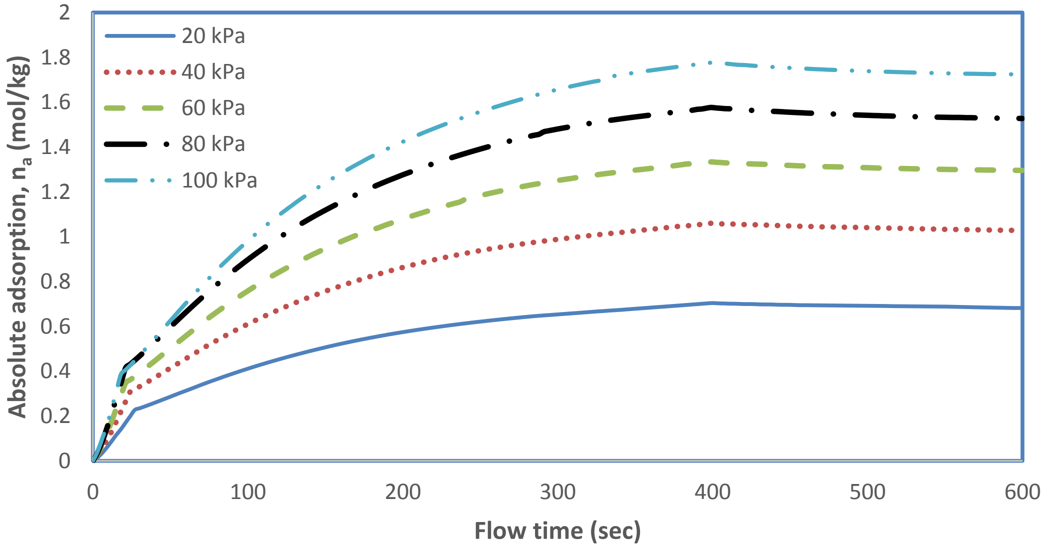

Figure 46: Time variation of absolute adsorption history of CO_2 in Activated carbon at Point 03 for varying storage pressure

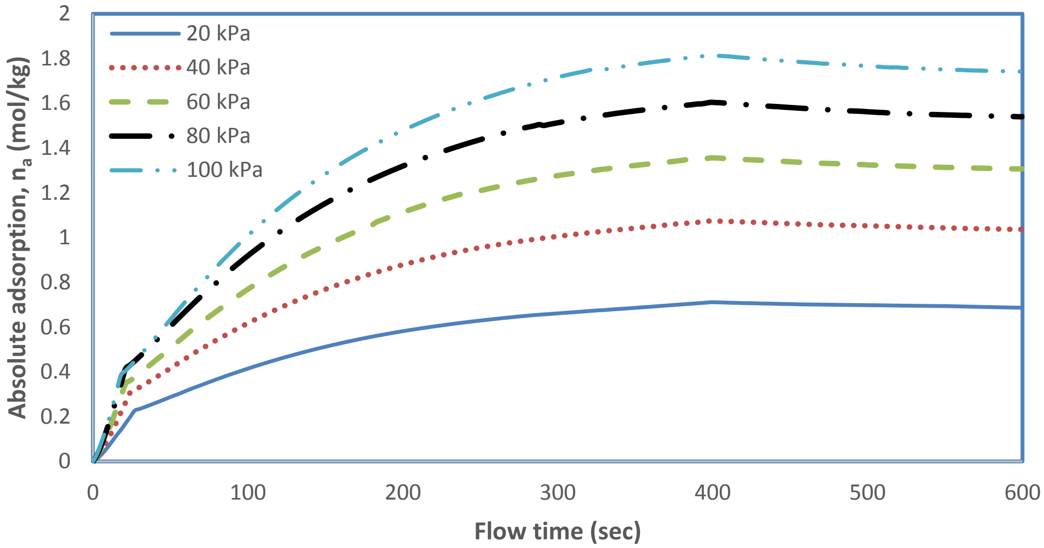

Figure 47: Time variation of absolute adsorption history of CO_2 in Activated carbon at Point 04 for varying storage pressure

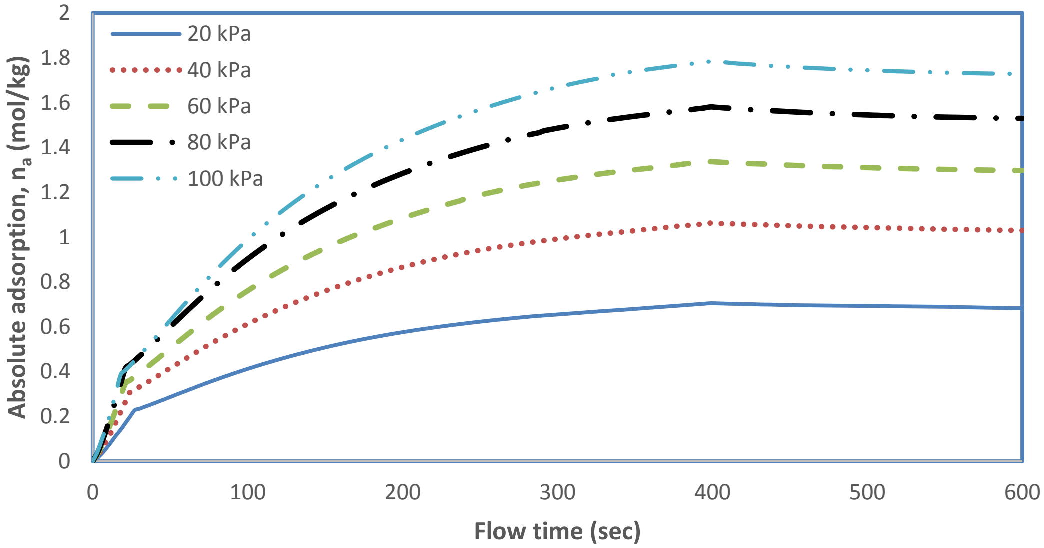

Figure 48: Time variation of absolute adsorption history of CO_2 in Activated carbon at Point 05 for varying storage pressure

Figure 49 shows the time variation of volumetric average value of absolute adsorption of CO_2 in Activated carbon for varying storage pressure cases. It can be seen that adsorption of CO_2 increases with increase in storage pressure because differential molar work of adsorption decreases with increase in pressure, which results in increase of degree of filling of micropores subsequently increasing absolute adsorption amount of CO_2 gas in the storage tank. In case 1 the amount of absolute adsorption is about 0.68 mol/kg. Absolute adsorption amount at the end of charging phase is 1.03 mol/kg for case 2, 1.30 mol/kg for case 3, 1.53 mol/kg for case 4 and 1.73 mol/kg for case 5.

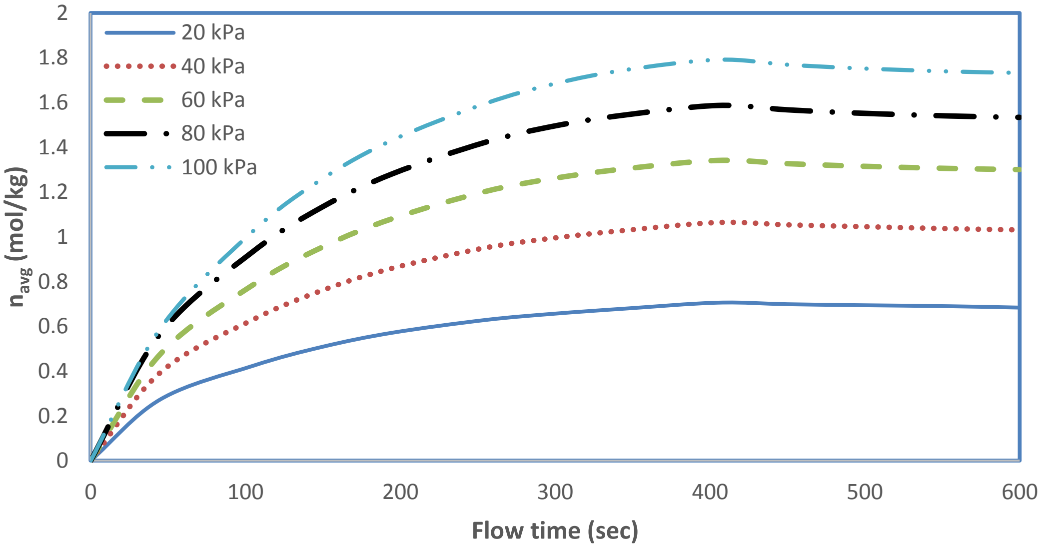

Figure 49: Time variation of volumetric average value of absolute adsorption of CO_2, n_{avg} in Activated carbon for varying storage pressure

Figures 50 – 52 provide temperature histories of adsorption of CO_2 in Activated carbon at point 03, 04 and 05 respectively with varying storage pressure. Initially sharp rise of temperature is because of higher adsorption rate due to large pressure gradient. Which results in releasing more energy thus increasing temperature of adsorption bed. Similar to the cases of adsorption on CO_2 in Mg-MOF-74 and Zeolite, maximum temperature is found at point 03. For all cases, peak value of temperature at point 04 occurs at about 210 seconds, which is earlier than the peaks of temperature at point 03 and 05. At point 04 heat dissipation due to conduction is strong which restricts the peak value. However at points 03 and 05 temperature keeps on rising till 260 seconds due to poor heat dissipation of the adsorption bed owing to is low thermal conductivity.

In Figure 50, it can be seen that temperature at point 03 increases with increase in storage pressure. Peak value of temperature at point 03 is 335 K for case 1, 359 K for case 2, 379 K for case 3, 395 K for case 4 and 416 K for case 5 respectively. This is because absolute adsorption increases with increase in storage pressure consequently increasing the temperature at point 03 in the center of storage tank.

Figure 51 shows temperature histories of adsorption of CO_2 in Zeolite at point 04 with varying storage pressure. Peak value of temperature is 304 K for case 1, 309 K for case 2, 314 K for case 3, 317.6 K for case 4 and 322 K for case 5 respectively. This is because increase in pressure enhances adsorption resulting in more heat being released because of its exothermic nature. However temperature at point 04 is lower compared to temperatures at point 03 and 05 because of its proximity to the wall. Heat transfer due to conduction is much better at this point which results in lower peak temperature.

Figure 52 shows temperature histories of adsorption of CO_2 in Activated carbon at point 05 with varying storage pressure. A similar trend of increase in peak temperature values with increase in pressure is also observed at point 05.

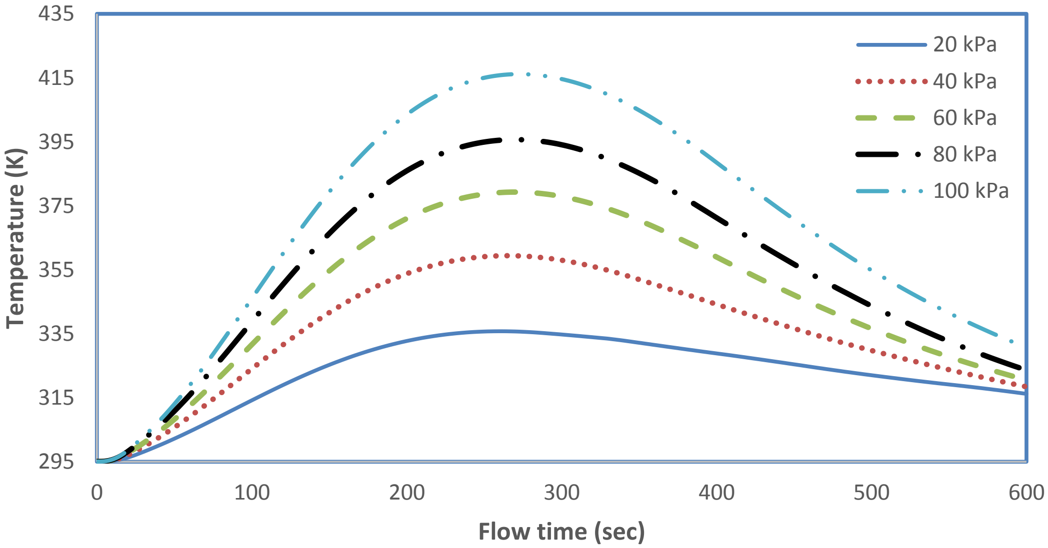

Figure 50: Temperature histories at point 03 for adsorption of CO_2 in Activated carbon for varying storage pressure

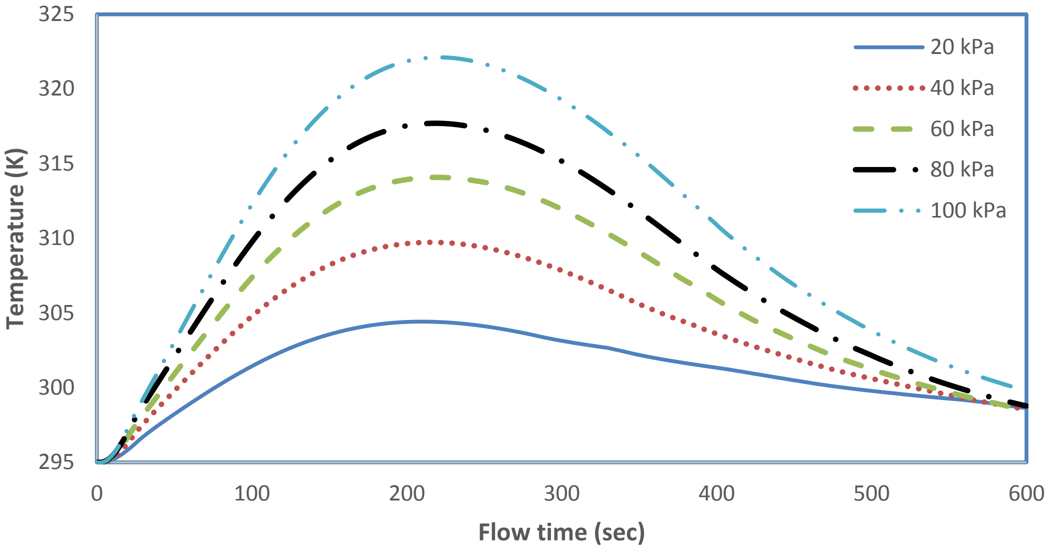

Figure 51: Temperature histories at point 04 for adsorption of CO_2 in Activated carbon for varying storage pressure

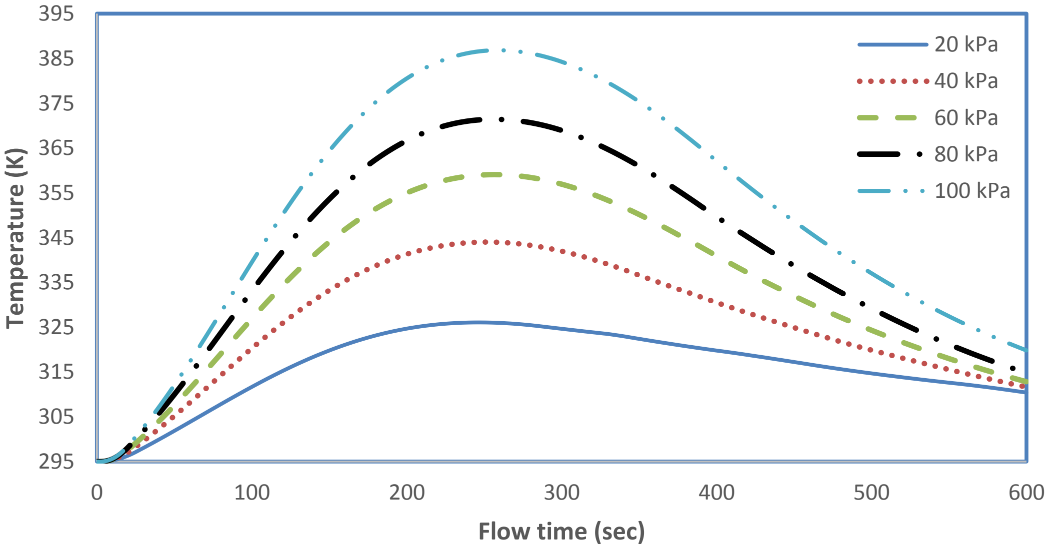

Figure 52: Temperature histories at point 05 for adsorption of CO_2 in Activated carbon for varying storage pressure

4.4 Comparison of Adsorbents for CO_2 Storage

Figures 53 – 57 show the time variation of volumetric average absolute adsorption of CO_2 for Mg-MOF-74, Zeolite and Activated carbon for pressure range from 20 kPa to 100 kPa. For each case maximum absolute adsorption is observed in Mg-MOF-74 followed by Zeolite and Activated carbon respectively. This shows that under similar charging conditions the uptake capacity of Mg-MOF-74 is higher compared to Zeolite and Activated carbon. This is due to the reason that the ratio of adsorption potential and characteristic free energy of adsorption for activated carbon is higher compared to Zeolite and Mg-MOF-74. However from equation 10 it can be seen that for higher adsorption capacity this ratio should be small. That is why the absolute adsorption of activated carbon is low compared to zeolite and Mg-MOF-74. However in case of Mg-MOF-74 and Zeolite this ratio is almost same but due to larger value of limiting adsorption of Mg-MOF-74 compared to zeolite, absolute adsorption of Mg-MOF-74 is higher compared to zeolite.

Figure 58 shows variation of volumetric average absolute adsorption of CO_2 for Mg-MOF-74, Zeolite and Activated carbon with pressure range from 20 kPa to 100 kPa. It can be observed that with increase in pressure absolute adsorption of CO_2 increases in each adsorbents. However maximum amount of CO_2 adsorbed is found in Mg-MOF-74 followed by Zeolite and Activated carbon. At 100 kPa maximum amount of absolute adsorption of CO_2 is 8.75 mol/kg in Mg-MOF-74, 3.78 mol/kg in Zeolite and 1.73 mol/kg in Activated carbon. At 100 kPa Mg-MOF-74 stores more amount of CO_2 compared to activated carbon by 7.02 moles of CO_2 per kilogram of adsorbent.

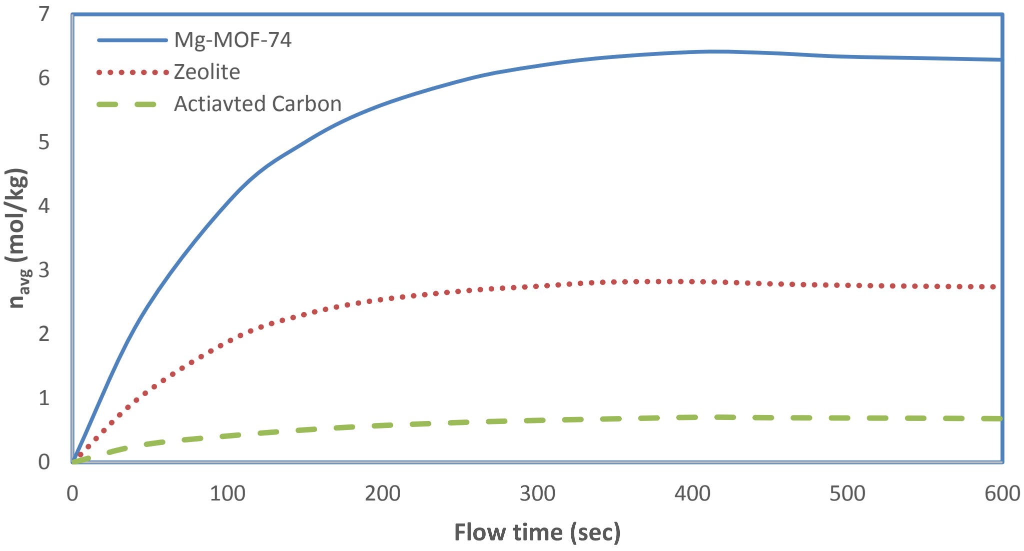

Figure 53: Time variation of volumetric average value of absolute adsorption of CO_2, n_{avg} in Mg-MOF-74, Zeolite and Activated carbon at 20 kPa

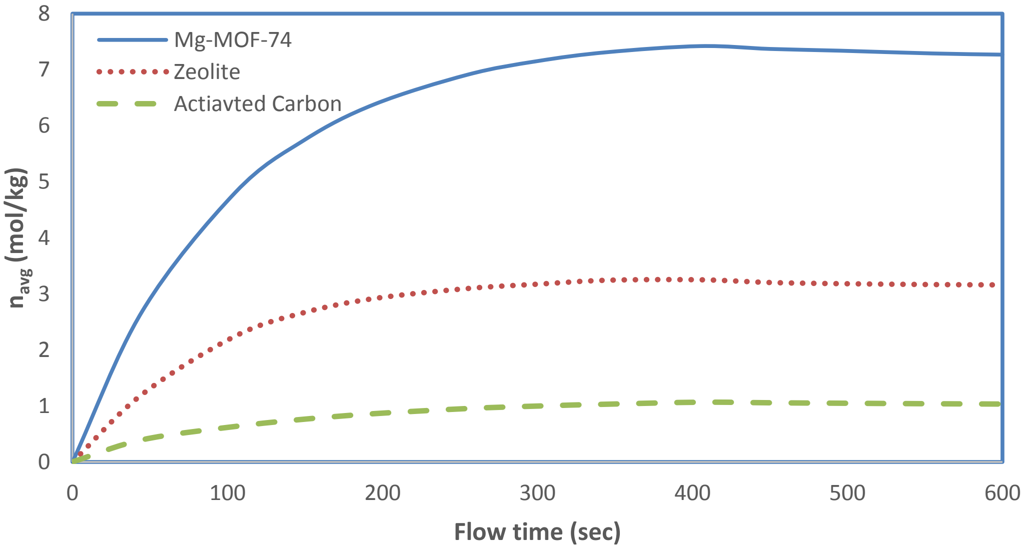

Figure 54: Time variation of volumetric average value of absolute adsorption of CO_2, n_{avg} in Mg-MOF-74, Zeolite and Activated carbon at 40 kPa

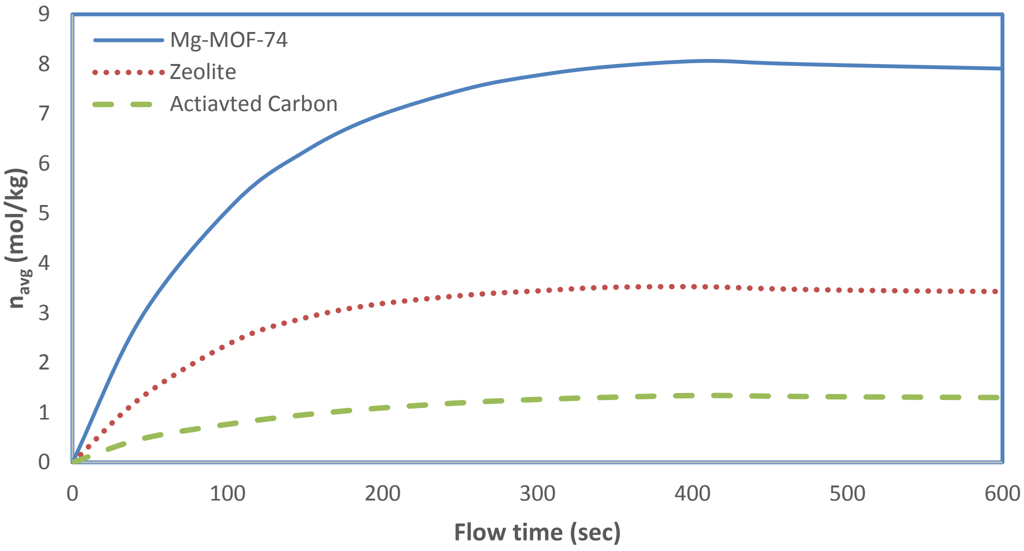

Figure 55: Time variation of volumetric average value of absolute adsorption of CO_2, n_{avg} in Mg-MOF-74, Zeolite and Activated carbon at 60 kPa

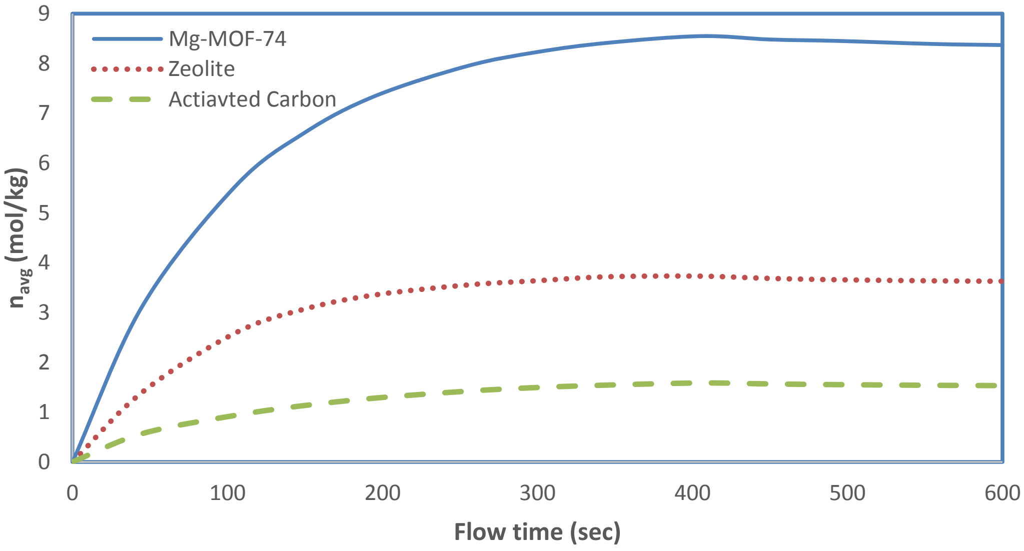

Figure 56: Time variation of volumetric average value of absolute adsorption of CO_2, n_{avg} in Mg-MOF-74, Zeolite and Activated carbon at 80 kPa

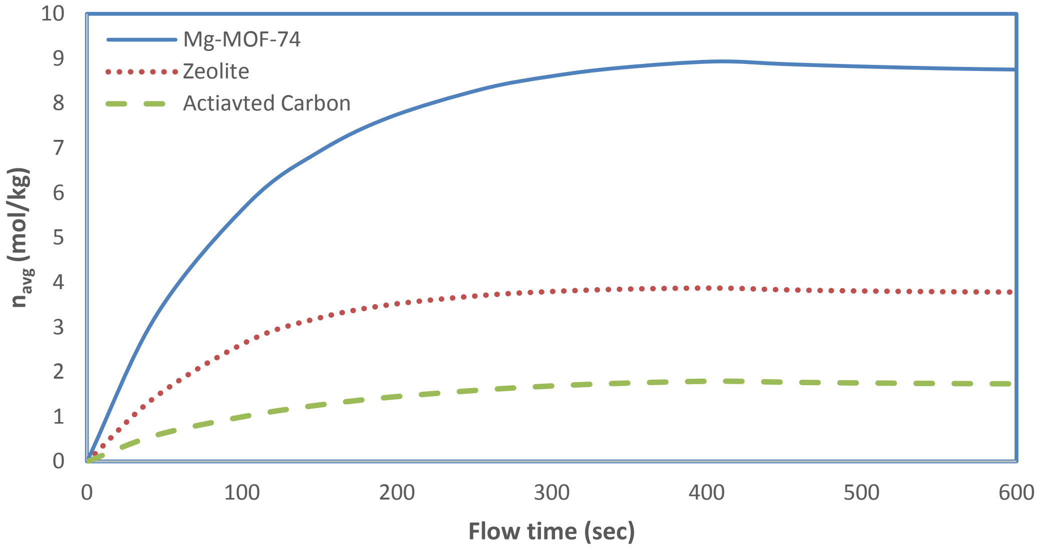

Figure 57: Time variation of volumetric average value of absolute adsorption of CO_2, n_{avg} in Mg-MOF-74, Zeolite and Activated carbon at 100 kPa

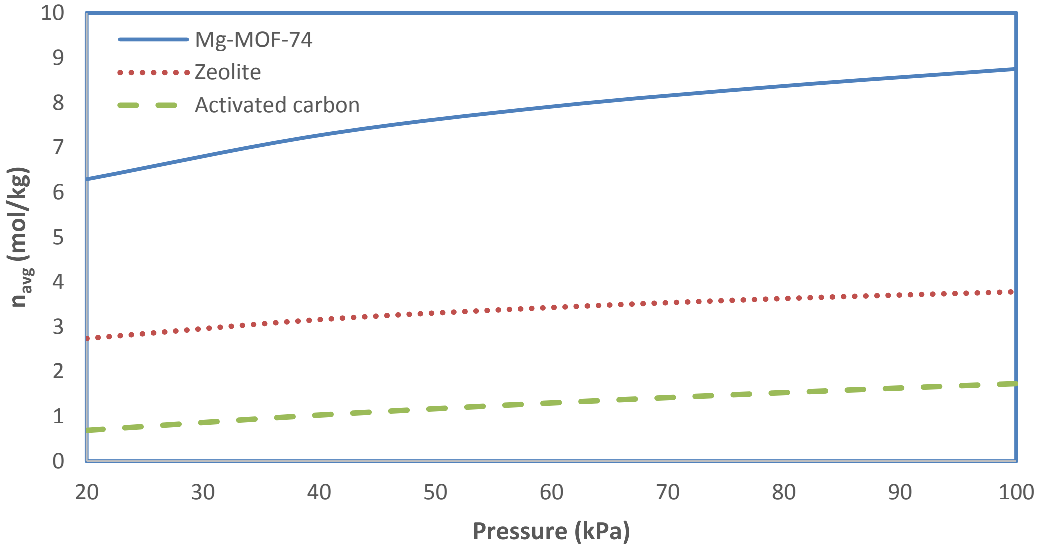

Figure 58: Pressure variation of volumetric average value of absolute adsorption of CO_2, n_{avg} in Mg-MOF-74, Zeolite and Activated carbon

4.5 Effect of Bed Porosity on Adsorption

To investigate the effect of variation of bed porosity on adsorption phenomena of CO_2 in Mg-MOF-74, Zeolite and Activated carbon three cases have been considered. For case 1 bed porosity value is set to 0.66, for case 2 bed porosity is 0.72 and 0.78 for case 3. Constant mass flux corresponding to 0.001 kg/sec mass flow rate being applied at inlet using UDF for the time 0 to 400 sec followed by 200 sec for the system to get stabilize. Operating pressure is adjusted to 100 kPa. Temperature of storage tank walls is kept constant at 295 K and CO_2 gas is fed at 295 K. Viscous and Inertial resistance coefficients have been calculated for each porosity value and applied in FLUENT while case setup for each adsorbent. Moreover UDF is also updated in accordance with the varying bed porosity for each adsorbent.

4.5.1 Effect of bed porosity on adsorption of CO_2 in Mg-MOF-74

Figures 59 – 61 provide temperature histories of adsorption of CO_2 in Mg-MOF-74 at point 03, 04 and 05 respectively with varying bed porosity. In figure 59 it can be observed that for case 1, bed porosity is adjusted to 0.66, the peak value of temperature at point 03 is 705 K and occurs at about 270 seconds. For case 2, bed porosity is equal to 0.72, peak value of temperature is 741 K and occurs at about 305 seconds. Whereas for case 3, bed porosity is equal to 0.78, the peak value of temperature reaches to 745 K and is found at 350 seconds. At the end of 600 seconds temperature at point 03 is 404 K for case 1, 499 K for case 2 and 593 K for case 3. So it can be concluded that with increase in bed porosity, peak value of temperature is increased but also a delay in the peaks of temperature at point 03 is observed with increase in bed porosity. The possible reason behind this might be the effective thermal conductivity of the adsorption bed. From Eq. 09 we can see that with increase in porosity of the adsorption bed the effective thermal conductivity of the bed gets decreased. This decrease in effective thermal conductivity impedes the effect of isothermal walls and heat transfer from central region to the walls is poor. Due to this large variation in peak value is observed.

Figure 60 shows temperature histories of adsorption of CO_2 in Mg-MOF-74 at point 04 with varying bed porosity. Peak value of temperature for case 1 is 383 K and occurs at 200 seconds, for case 2 is 390 K and occurs at 240 seconds and for case 3 is 392 K and occurs at 285 seconds. This might be due to the same reason of effective thermal conductivity of the adsorption bed as explained earlier. With increase in bed porosity the effective thermal conductivity is decreased which hinders the heat transfer to the walls.

Figure 61 shows temperature histories of adsorption of CO_2 in Mg-MOF-74 at point 05 with varying bed porosity. Peak value of temperature for case 1 is 604 K and occurs at 245 seconds, for case 2 is 631 K and occurs at 290 seconds and for case 3 is 633 K and occurs at 335 seconds. This delay of peaks of temperature at point 05 is due to effective thermal conductivity of the bed which decreases with increase in bed porosity resulting in poor heat transfer. That is why at the end of 600 seconds temperature at point 04 is 368 K for case 1, 435 K for case 2 and 505 K for case 3. So it is found that adsorption bed with large porosity will take more time to cool down compared to adsorption bed with lower porosity.

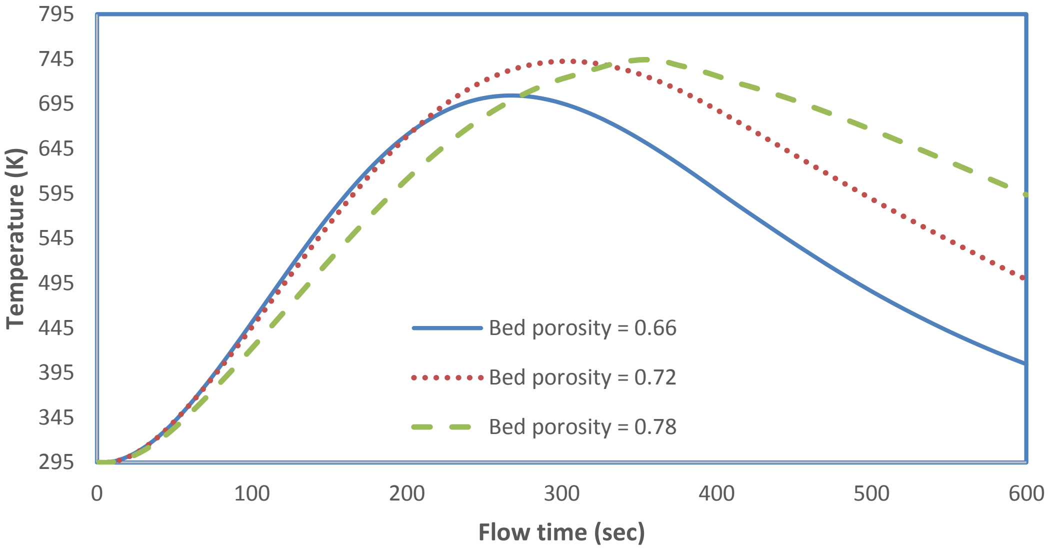

Figure 59: Temperature histories of adsorption of CO_2 in Mg-MOF-74 at point 03 for varying bed porosity (ε_b)

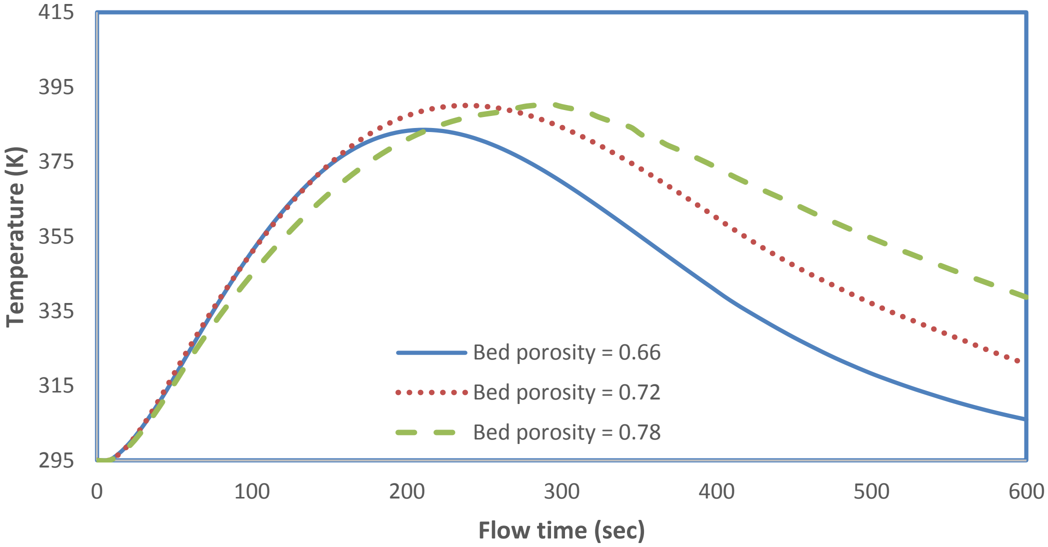

Figure 60: Temperature histories of adsorption of CO_2 in Mg-MOF-74 at point 04 for varying bed porosity (ε_b)

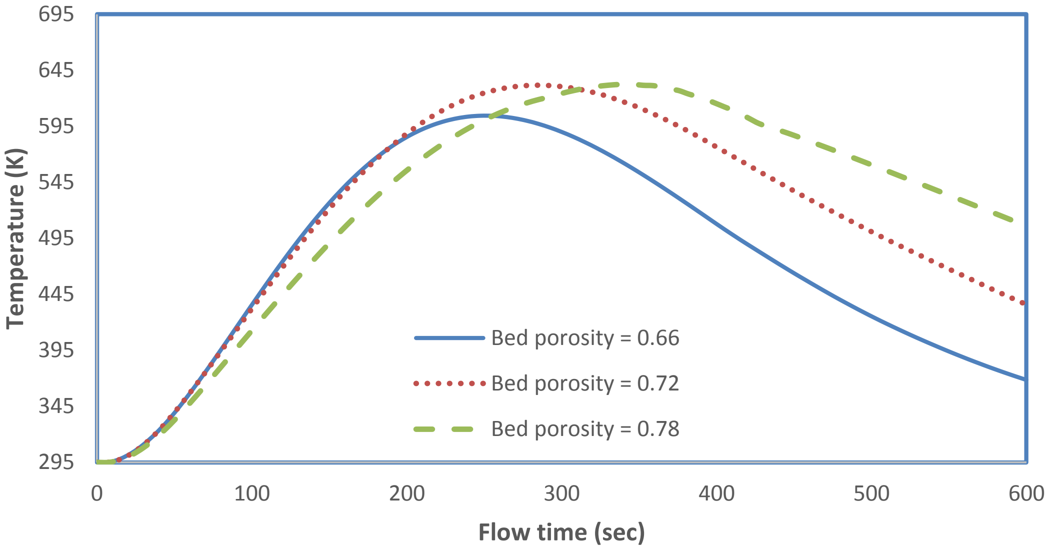

Figure 61: Temperature histories of adsorption of CO_2 in Mg-MOF-74 at point 05 for varying bed porosity (ε_b)

4.5.2 Effect of bed porosity on adsorption of CO_2 in Zeolite

Figures 62 – 64 provide temperature histories of adsorption of CO_2 in Zeolite at point 03, 04 and 05 respectively with varying bed porosity. Figure 62 shows temperature histories of adsorption of CO_2 in Zeolite at point 03 with varying bed porosity. For case 1 the peak value of temperature is 473 K and occurs at 215 seconds, 476.2 K and occurs at 265 seconds for case 2 and 481.4 K occurring at 300 seconds for case 3. After 600 seconds temperature of point 03 falls down to 319.75 K for case 1, 354 K for case 2 and 387 K for case 3. Figure 63 shows temperature histories of adsorption of CO_2 in Zeolite at point 04 with varying bed porosity. Peak values of temperature for case 1 is 338.7 K found at 170 seconds, 339.3 K found at 200 seconds for case 2 and 339.9 K found at 230 seconds for case 3. At the end of 600 seconds the temperature at point 04 is 296 K, 302 K and 307.5 K for case 1, 2 and 3 respectively. Figure 64 shows temperature histories of adsorption of CO_2 in Zeolite at point 05 with varying bed porosity. Peak value of temperature is 433 K found at 202 seconds for case 1, 435 K found at 240 seconds for case 2 and 438.5 K found at 277 seconds for case 3. At the end of 600 seconds the temperature at point 05 is 311 K, 335 K and 359 K for case 1, 2 and 3 respectively. Possible reason behind this rise in temperature and delay in peak values of temperature with increase in bed porosity is effective thermal conductivity of the bed. With increase in bed porosity the effective thermal conductivity of the bed is reduced which inhibits the transfer of energy resulting in large variation of temperature.

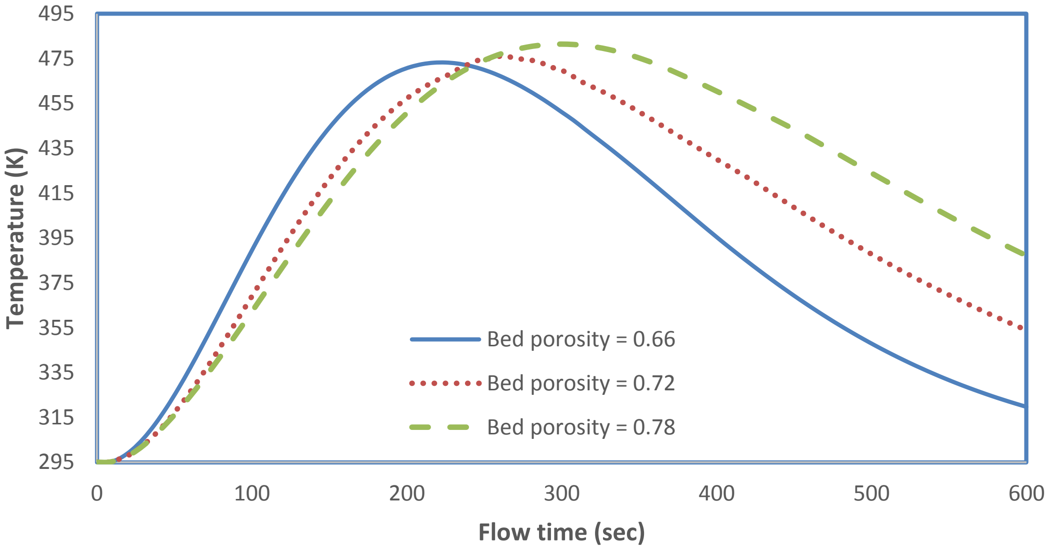

Figure 62: Temperature histories of adsorption of CO_2 in Zeolite at point 03 for varying bed porosity (ε_b)

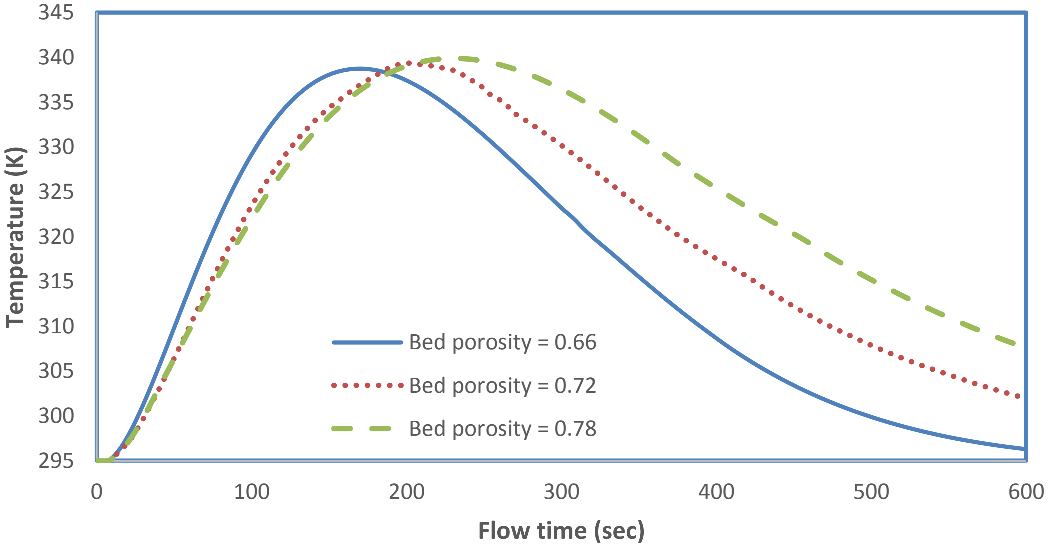

Figure 63: Temperature histories of adsorption of CO_2 in Zeolite at point 04 for varying bed porosity (ε_b)

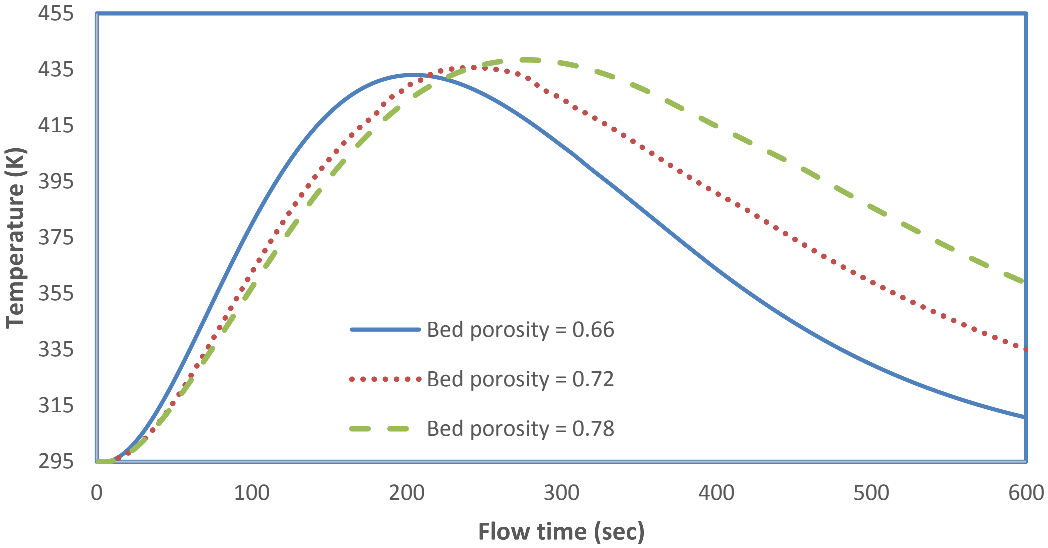

Figure 64: Temperature histories of adsorption of CO_2 in Zeolite at point 05 for varying bed porosity (ε_b)

4.5.3 Effect of bed porosity on adsorption of CO_2 in Activated carbon

Figures 65 – 67 provide temperature histories of adsorption of CO_2 in Activated carbon at point 03, 04 and 05 respectively with varying bed porosity. Figure 65 shows temperature histories at point 03 with varying bed porosity. For case 1 the peak value of temperature is 416 K and occurs at 270 seconds, for case 2 peak value of temperature is 420 K and occurs at 325 seconds and 428 K occurring at 385 seconds for case 3. After 600 seconds temperature at point 03 is 330.7 K for case 1, 367 K for case 2 and 403 K for case 3. Figure 66 shows temperature histories of adsorption of CO_2 in activated carbon at point 04 with varying bed porosity. Peak values of temperature for case 1 is 322 K found at 220 seconds, 322.25 K found at 270 seconds for case 2 and 323.5 K found at 325 seconds for case 3. At the end of 600 seconds the temperature at point 04 is 300 K, 307 K and 314 K for case 1, 2 and 3 respectively. Figure 67 shows temperature histories of adsorption of CO_2 in activated carbon at point 05 with varying bed porosity. Peak value of temperature is 386 K found at 260 seconds for case 1, 389.3 K found at 310 seconds for case 2 and 395 K found at 375 seconds for case 3. At the end of 600 seconds the temperature at point 05 is 319.8 K, 347.2 K and 374.3 K for case 1, 2 and 3 respectively. Possible reason behind this rise in temperature and delay in peak values of temperature with increase in bed porosity might be the same as explained earlier i.e. effective thermal conductivity of the bed. With increase in bed porosity the effective thermal conductivity of the bed is reduced which inhibits the transfer of energy resulting in large variation of temperature.

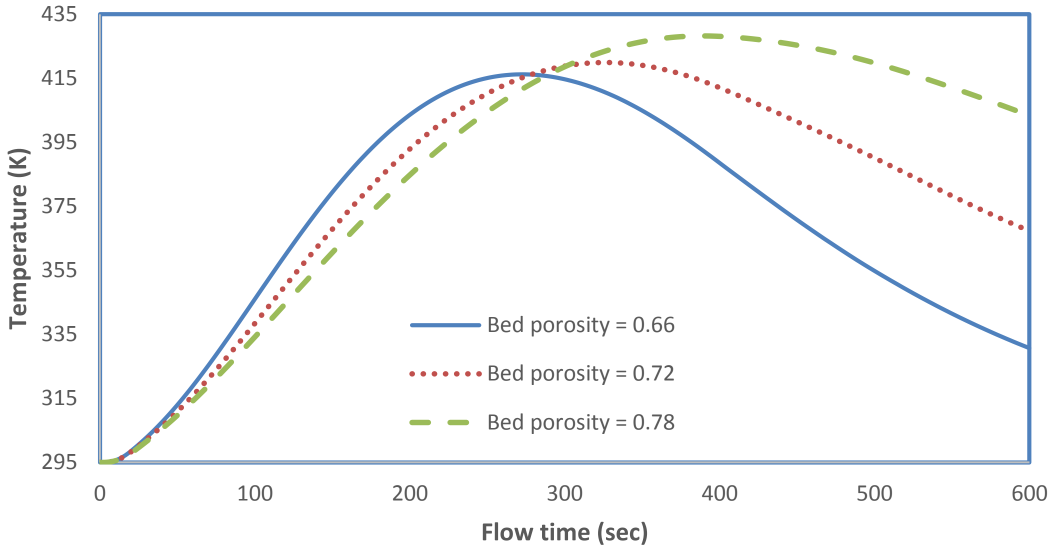

Figure 65: Temperature histories of adsorption of CO_2 in Activated carbon at point 03 for varying bed porosity (ε_b)

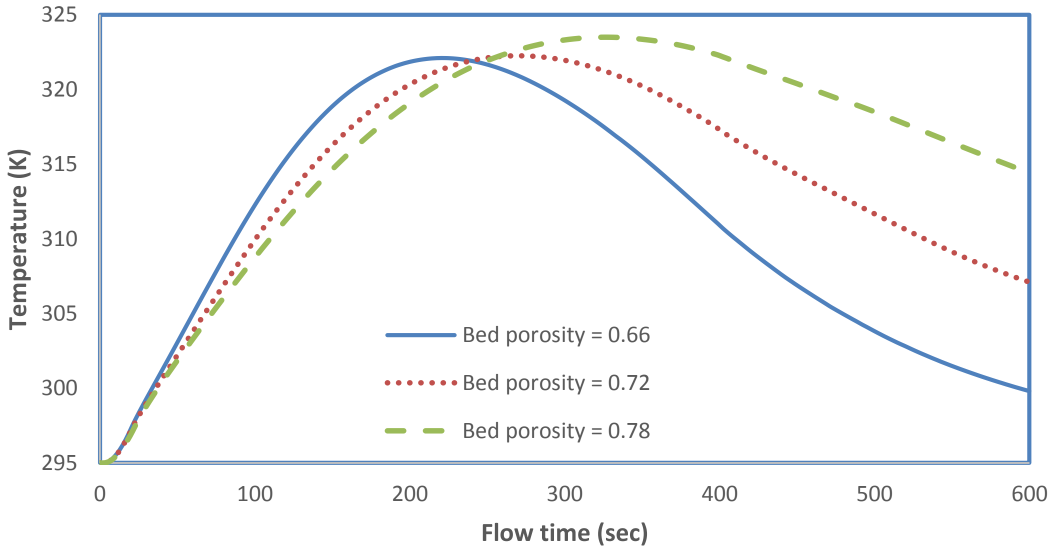

Figure 66: Temperature histories of adsorption of CO_2 in Activated carbon at point 04 for varying bed porosity (ε_b)

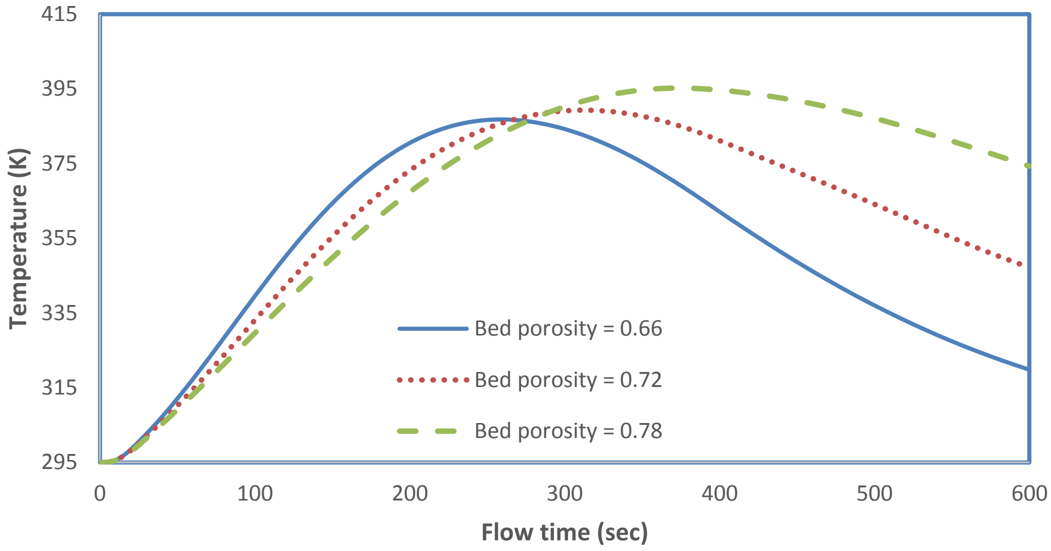

Figure 67: Temperature histories of adsorption of CO_2 in Activated carbon at point 05 for varying bed porosity (ε_b)

4.5.4 Effect of variation of bed porosity on adsorption

Figure 68 shows variation of volumetric average absolute adsorption of CO_2 for Mg-MOF-74, Zeolite and Activated carbon with bed porosity ranging from 0.66 to 0.78. It can be observed that bed porosity does not affect the absolute adsorption significantly. Because bed porosity represents the macropore porosity "ε_{ma}"of the adsorbent and provides the flow channel to the gas flowing through adsorption bed only. Therefore absolute adsorption of CO_2 for each adsorbent remains the same.

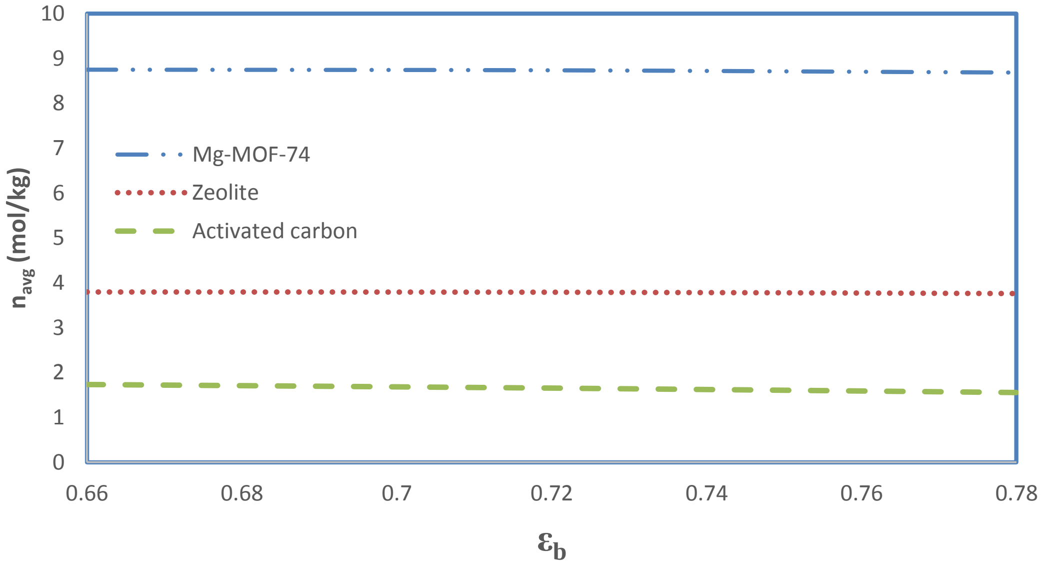

Figure 68: Bed porosity (ε_b) variation of volumetric average value of absolute adsorption of CO_2, n_{avg} in Mg-MOF-74, Zeolite and Activated carbon

CHAPTER 5

CONCLUSIONS AND RECOMMENDATIONS

The conclusion is divided into two sections. In the first section the numerical results are summarized and in the second section, proposed directions have been made for future research.

5.1. Conclusions

The study results indicate that;

a) For all adsorbents, temperature is maximum and adsorption is minimum at the central region of the adsorption bed.

b) The amount of absolute adsorption has been increased while increasing storage pressure.

c) Mg-MOF-74 adsorbent material showed high adsorption capacity as compared to zeolite and activate carbon.

d) Increase in bed porosity has no significant effect on the adsorption of CO2 however peak value of temperatures at different locations within the adsorption bed are delayed for each adsorbent.

5.2. Recommendations

As an extension for the present study, the following can be considered:

a) Dubinin-Astakov (D-A) adsorption model can be used to investigate the adsorption capacity of different MOFs material for CO_2 storage.

b) Simulation of breakthrough experiments can be performed with the help of this CFD model.

c) This model can be used for the separation of CO_2 from the mixture of gases like N_2, O_2 etc.

NOMENCLATURE

$\overset{=}{\tau}$	Stress tensor, Pa
ε_b	Bed porosity
ε_{mi}	Micropore porosity
ρ_g	Gas density, kg m^{-3}
$\vec{v}$	Superficial velocity vector, m s^{-1}
S_m	Mass source term, kg m^{3} s^{-1}
ρ_p	Particle density of adsorbent, kg m^{-3}
M_g	Molecular mass of gas, kg mol^{-1}
k_{eff}	Effective thermal conductivity of the medium, W m^{-1} k^{-1}
h_i	Species enthalpy along *i* direction, J kg^{-1}
ΔH	Isosteric heat of adsorption, J mol^{-1}
k_s	Thermal conductivity of the solid phase, W m^{-1} k^{-1}
$n_{\max}$	Limiting adsorption, mol kg^{-1}
E	Characteristic free energy of adsorption
R	Universal gas constant, J mol^{-1} K^{-1}
n_a	Absolute adsorption of gas in moles per unit mass of the adsorbent, mol kg^{-1}
α	Enthalpic factor, J mol^{-1}
$\vec{S}$	Momentum source term, N m^{-3}
ε_{ma}	Macropore porosity
μ	Dynamic viscosity of gas, Pa s
C_1	Permeability, m^{2}
C_2	Inertial resistance coefficient, m^{-1}
E_g	Total gas energy, J kg^{-1}
E_s	Energy of solid phase, J kg^{-1}
S_h	Energy source term
$\vec{J}_i$	Diffusion flux of species along *i* direction, kg m^{-2} s^{-1}
k_g	Thermal conductivity of the gas, W m^{-1} k^{-1}
θ	Degree of filling of volume of micropores
β	Entropic factor, J mol^{-1} K^{-1}
P_o	Limiting pressure, Pa
n_{avg}	Volumetric average absolute adsorption, mol kg^{-1}
A	Differential molar work of adsorption or adsorption potential, J mol^{-1}

REFERENCES

[1] F. Lecomte, P. Broutin, and E. Lebas, *CO_2 Capture Technologies to reduce greenhouse gas emissions*. IFP Publications, 2010, pp. 1–10.

[2] IFP-BRGM-ADEME, *CO_2 capture and storage in the subsurface*. 2007.

[3] IPCC, “Climate change, Synthesis Report,” 2007.

[4] K. Jordal, M. Anheden, J. Yan, and Lars Stromberg, “Oxyfuel Combustion for Coal-Fired Power Generation with CO_2 Capture – Opportunities and Challenges,” 2004.

[5] G. Hermosillalara, G. Momen, P. Marty, B. Leneindre, and K. Hassouni, “Hydrogen storage by adsorption on activated carbon: Investigation of the thermal effects during the charging process,” *Int. J. Hydrogen Energy*, vol. 32, no. 10–11, pp. 1542–1553, Jul. 2007.

[6] “World CO_2 emissions.” [Online]. Available: http://commons.wikimedia.org/wiki/File:World-co2-emissions-by-fuel-1990---2035-USDOE-IEA-2011.png.

[7] I. International energy agency, “Key World Statistics.,” France, 2007.

[8] C. Kunze and H. Spliethoff, “Assessment of oxy-fuel, pre- and post-combustion-based carbon capture for future IGCC plants,” *Appl. Energy*, vol. 94, pp. 109–116, Jun. 2012.

[9] B. J. P. Buhre, L. K. Elliott, C. D. Sheng, R. P. Gupta, and T. F. Wall, “Oxy-fuel combustion technology for coal-fired power generation,” *Prog. Energy Combust. Sci.*, vol. 31, no. 4, pp. 283–307, Jan. 2005.

[10] C. K. Law, D. L. Zhu, and G. Yu, “Propagation and extinction of stretched premixed flames,” in *Twenty-first Symposium (International) on Combustion/The Combustion Institute*, 1986, vol. i, pp. 1419–1426.

[11] K. Andersson and F. Johnsson, “Flame and radiation characteristics of gas-fired O_2/CO_2 combustion,” *Fuel*, vol. 86, no. 5–6, pp. 656–668, Mar. 2007.

[12] I. Pfaff and A. Kather, “Comparative thermodynamic analysis and integration issues of CCS steam power plants based on oxy-combustion with cryogenic or membrane based air separation,” *Energy Procedia*, vol. 1, no. 1, pp. 495–502, Feb. 2009.

[13] A. P. Simpson and a. J. Simon, “Second law comparison of oxy-fuel combustion and post-combustion carbon dioxide separation,” *Energy Convers. Manag.*, vol. 48, no. 11, pp. 3034–3045, Nov. 2007.

[14] E. Kakaras, A. Koumanakos, A. Doukelis, D. Giannakopoulos, and I. Vorrias, “Oxyfuel boiler design in a lignite-fired power plant,” *Fuel*, vol. 86. pp. 2144–2150, 2007.

[15] L. Eide and D. Bailey, “Pre-combustion decarbonisation process,” *Oil gas Sci. Technol.*, vol. 60, no. 3, pp. 475–484, 2004.

[16] D. Singh, E. Croiset, P. . Douglas, and M. . Douglas, “Techno-economic study of CO_2 capture from an existing coal-fired power plant: MEA scrubbing vs. O_2/CO_2 recycle combustion,” *Energy Convers. Manag.*, vol. 44, no. 19, pp. 3073–3091, Nov. 2003.

[17] P. Folger, “Carbon Capture : A Technology Assessment,” 2013.

[18] P. Folger, “Carbon Capture and Sequestration : Research , Development , and Demonstration at the U . S . Department of Energy,” 2014.

[19] M. A. Habib, H. M. Badr, S. F. Ahmed, K. Mezghani, and S. Imashuku, “A review of recent developments in carbon capture utilizing oxy-fuel combustion in conventional and ion transport membrane systems,” no. December 2010, pp. 741–764, 2011.

[20] Z. R. Herm, “MOFiosos,” 2012. [Online]. Available: http://berkeleysciencereview.com/article/mofiosos/.

[21] A. R. Millward and O. M. Yaghi, “Metal-organic frameworks with exceptionally high capacity for storage of carbon dioxide at room temperature.,” *J. Am. Chem. Soc.*, vol. 127, no. 51, pp. 17998–9, Dec. 2005.

[22] K. S. Walton, A. R. Millward, D. Dubbeldam, H. Frost, J. J. Low, O. M. Yaghi, and R. Q. Snurr, “Understanding inflections and steps in carbon dioxide adsorption isotherms in metal-organic frameworks.,” *J. Am. Chem. Soc.*, vol. 130, no. 2, pp. 406–7, Jan. 2008.

[23] D. Britt, H. Furukawa, B. Wang, T. G. Glover, and O. M. Yaghi, "Highly efficient separation of carbon dioxide by a metal-organic framework replete with open metal sites.," *Proc. Natl. Acad. Sci. U. S. A.*, vol. 106, no. 49, pp. 20637–40, Dec. 2009.

[24] Y. S. Bae, O. K. Farha, J. T. Hupp, and R. Q. Snurr, "Enhancement of CO_2/N_2 selectivity in a metal-organic framework by cavity modification," *J. Mater. Chem.*, vol. 19, no. 15, p. 2131, 2009.

[25] A. O. Yazaydin, R. Q. Snurr, T.-H. Park, K. Koh, J. Liu, M. D. Levan, A. I. Benin, P. Jakubczak, M. Lanuza, D. B. Galloway, J. J. Low, and R. R. Willis, "Screening of metal-organic frameworks for carbon dioxide capture from flue gas using a combined experimental and modeling approach.," *J. Am. Chem. Soc.*, vol. 131, no. 51, pp. 18198–9, Dec. 2009.

[26] J. A. Mason, K. Sumida, Z. R. Herm, R. Krishna, and J. R. Long, "Evaluating metal–organic frameworks for post-combustion carbon dioxide capture via temperature swing adsorption," *Energy Environ. Sci.*, vol. 4, no. 8, p. 3030, 2011.

[27] J. Yu and P. B. Balbuena, "Water Effects on Postcombustion CO_2 Capture in Mg-MOF-74," *J. Phys. Chem. C*, vol. 117, no. 7, pp. 3383–3388, Feb. 2013.

[28] Q. Wang, J. Luo, Z. Zhong, and A. Borgna, "CO_2 capture by solid adsorbents and their applications: current status and new trends," *Energy Environ. Sci.*, vol. 4, no. 1, p. 42, 2011.

[29] S. B. Choi, H. Furukawa, H. J. Nam, D.-Y. Jung, Y. H. Jhon, A. Walton, D. Book, M. O'Keeffe, O. M. Yaghi, and J. Kim, "Reversible interpenetration in a metal-organic framework triggered by ligand removal and addition.," *Angew. Chem. Int. Ed. Engl.*, vol. 51, no. 35, pp. 8791–5, Aug. 2012.

[30] Z. Zhao, Z. Li, and Y. S. Lin, "Adsorption and Diffusion of Carbon Dioxide on Metal - Organic Framework (MOF-5)," pp. 10015–10020, 2009.

[31] M. A. Richard, P. Bénard, and R. Chahine, "Gas adsorption process in activated carbon over a wide temperature range above the critical point. Part 1: modified Dubinin-Astakhov model," *Adsorption*, vol. 15, no. 1, pp. 43–51, Feb. 2009.

[32] J. Xiao, L. Tong, C. Deng, P. Bénard, and R. Chahine, "Simulation of heat and mass transfer in activated carbon tank for hydrogen storage," *Int. J. Hydrogen Energy*, vol. 35, no. 15, pp. 8106–8116, Aug. 2010.

[33] F. Ye, J. Xiao, B. Hu, P. Benard, and R. Chahine, "Implementation for Model of Adsoptive Hydrogen Storage Using UDF in Fluent," *Phys. Procedia*, vol. 24, pp. 793–800, Jan. 2012.

[34] J. Xiao, M. Hu, P. Bénard, and R. Chahine, "Simulation of hydrogen storage tank packed with metal-organic framework," *Int. J. Hydrogen Energy*, vol. 38, no. 29, pp. 13000–13010, Sep. 2013.

[35] J. Xiao, M. Hu, D. Cossement, P. Bénard, and R. Chahine, “Finite element simulation for charge–discharge cycle of cryo-adsorptive hydrogen storage on activated carbon,” *Int. J. Hydrogen Energy*, vol. 37, no. 17, pp. 12947–12959, Sep. 2012.

[36] J. Xiao, R. Peng, D. Cossement, P. Bénard, and R. Chahine, “CFD model for charge and discharge cycle of adsorptive hydrogen storage on activated carbon,” *Int. J. Hydrogen Energy*, vol. 38, no. 3, pp. 1450–1459, Feb. 2013.

[37] X. Bai, “Multi-dimensional CFD simulation of adsorption/desorption processes in carbon canister,” University o f Missouri-Rolla, 2004.

[38] X. Bai, K. M. Isaac, D. Klein, R. Banerjee, J. Edson, W. Breig, and L. Oliver, “Multidimensional, Time-Accurate CFD Simulation of Adsorption/Desorption in a Carbon Canister,” Mar. 2003.

[39] S. Sircar and R. Kumar, “Adiabatic adsorption of bulk binary gas mixtures. Analysis by constant pattern model,” *Ind. Eng. Chem. Process Des. Dev.*, vol. 22, no. 2, pp. 271–280, Apr. 1983.

[40] H. Yoshida and D. M. Ruthven, “Dynamic behaviour of an adiabatic adsorption column—I Analytic solution for irreversible adsorption,” *Chem. Eng. Sci.*, vol. 38, no. 6, pp. 877–884, Jan. 1983.

[41] J. M. Schork and J. R. Fair, “Parametric analysis of thermal regeneration of adsorption beds,” *Ind. Eng. Chem. Res.*, vol. 27, no. 3, pp. 457–469, Mar. 1988.

[42] G. A. Lavoie, P. J. Johnson, and J. F. Hood, “Carbon Canister Modeling for Evaporative Emissions: Adsorption and Thermal Effects,” May 1996.

[43] Y. Liu, C. E. Holland, and J. A. Ritter, “Solvent Vapor Recovery by Pressure Swing Adsorption. I. Experimental Transient and Periodic Dynamics of the Butane-Activated Carbon System,” *Sep. Sci. Technol.*, vol. 33, no. 15, pp. 2311–2334, Jan. 1998.

[44] Y. Liu, C. E. Holland, and J. A. Ritter, “Solvent Vapor Recovery by Pressure Swing Adsorption. II. Experimental Periodic Performance of the Butane-Activated Carbon System,” *Sep. Sci. Technol.*, vol. 33, no. 16, pp. 2431–2463, Jan. 1998.

[45] Y. Liu, C. E. Holland, and J. A. Ritter, “Solvent Vapor Recovery by Pressure Swing Adsorption. III. Comparison of Simulation with Experiment for the Butane—Activated Carbon System,” *Sep. Sci. Technol.*, vol. 34, no. 8, pp. 1545–1576, Jan. 1999.

[46] D. O. Cooney, “Numerical Investigation of Adiabatic Fixed-Bed Adsorption,” *Ind. Eng. Chem. Process Des. Dev.*, vol. 13, no. 4, pp. 368–373, Oct. 1974.

[47] M. Botzung, S. Chaudourne, O. Gillia, C. Perret, M. Latroche, A. Percheronguegan, and P. Marty, “Simulation and experimental validation of a hydrogen storage tank with metal hydrides,” *Int. J. Hydrogen Energy*, vol. 33, no. 1, pp. 98–104, Jan. 2008.

[48] H. K. Versteeg and W. Malalasekera, *An Introduction to Computational Fluid Dynamics The Finite Volume Method*, Second. 2007, pp. 179–211.

[49] Douglas C. Montgomery, *Design and Analysis of Experiments*, 5th ed. Wiley, 2004, p. 112.

[50] M. Sen, Ashish, Srivastava, *Regression Analysis: Theory, Methods, and Applications*. 1990, p. 5.

[51] N. Ravishankar and D. K. Dey, *A First Course in Linear Model Theory*. Chapman and Hall/CRC, Boca Raton, 2002, p. 101.

[52] M. H. Kutner, C. J. Nachtsheim, and J. Neter, *Applied Linear Regression Models*, 4th ed. McGraw-Hill/Irwin, Bosto, 2004, p. 25.

[53] J. A. Delgado, V. I. Águeda, M. A. Uguina, J. L. Sotelo, P. Brea, and C. A. Grande, "Adsorption and Diffusion of H_2 , CO, CH_4 , and CO_2 in BPL Activated Carbon and 13X Zeolite: Evaluation of Performance in Pressure Swing Adsorption Hydrogen Purification by Simulation," *Ind. Eng. Chem. Res.*, vol. 53, no. 40, pp. 15414–15426, Oct. 2014.

[54] Z. Bao, L. Yu, Q. Ren, X. Lu, and S. Deng, "Adsorption of CO2 and CH4 on a magnesium-based metal organic framework.," *J. Colloid Interface Sci.*, vol. 353, no. 2, pp. 549–56, Jan. 2011.

VITAE

Name : Yasir Jamil

Nationality : Pakistani

Date of Birth : 23-Mar-1985

Email : nettpanic@gmail.com
g201203740@kfupm.edu.sa

Address : House No. 539/H, Ward No. 09, Bukhari
Colony, Multan, Pakistan.

Academic background : Master of Science (M.S.) Dec, 2014
Mechanical Engineering Department
King Fahd University of Petroleum & Minerals,
Dhahran, Saudi Arabia.
Bachelors of Engineering (B.E.) Sep, 2007
Mechanical Engineering Department,
University of Engineering & Technology,
Lahore, Pakistan.

Research paper : CFD analysis of a CO_2 adsorption system using
different adsorbents including
activated carbon, zeolite and Mg-MOF-74.
Submitted – Separation & Purification Technology.